



# **Understanding high redshift Active Galactic Nuclei activity through infrared variability**

**Karel A. Green**

**REDACTED**

Thesis submitted to the University of Nottingham  
for the degree of Doctor of Philosophy

September 2024

*“I am, somehow, less interested in the weight and convolutions of Einstein’s brain than in the near certainty that people of equal talent have lived and died in cotton fields and sweatshops”*

– Stephen Jay Gould, *"The Panda's Thumb"*

Supervisors: Prof. Omar Almaini  
Prof. Michael Merrifield

Examiners: Prof. Andrew Lawrence (University of Edinburgh)  
Prof. Alfonso Aragón-Salamanca (University of Nottingham)

Submitted: 30 September 2024  
Examined: TBD  
Final version: ????

# Contents

<b>Abstract</b>	<b>vi</b>
<b>Acknowledgements</b>	<b>vii</b>
<b>Equality Diversity and Inclusion</b>	<b>ix</b>
<b>Published work</b>	<b>x</b>
<b>1 Introduction</b>	<b>1</b>
1.1 Extragalactic Astronomy . . . . .	2
1.2 Galaxies . . . . .	3
1.2.1 Black Holes . . . . .	4
1.3 Active Galaxies . . . . .	6
1.3.1 Discovery of Active Galactic Nuclei . . . . .	6
1.3.2 AGN and the evolution of the Universe . . . . .	7
1.3.3 AGN structure . . . . .	8
1.3.4 AGN detection methods . . . . .	12
1.4 Variability . . . . .	12

1.4.1	X-ray . . . . .	14
1.4.2	UV and Optical . . . . .	14
1.4.3	Infrared . . . . .	14
1.4.4	Gamma and Radio . . . . .	14
1.5	The host galaxies of active galactic nuclei . . . . .	14
1.6	Thesis Structure . . . . .	14
<b>2</b>	<b>Data</b>	<b>16</b>
2.1	UDS . . . . .	16
2.1.1	Redshifts . . . . .	17
2.1.2	Stellar Masses . . . . .	18
2.2	X-UDS . . . . .	19
2.3	CANDELS . . . . .	19
<b>3</b>	<b>Quantifying AGN variability</b>	<b>20</b>
3.1	Selecting AGN based on their IR variability . . . . .	21
3.2	Galaxies on the edge of the science image . . . . .	23
3.3	Measuring real variability: maximum likelihood . . . . .	23
3.4	Variability detection limit . . . . .	24
3.5	Modified monthly variability amplitude . . . . .	28
<b>4</b>	<b>Long-term near-infrared variability</b>	<b>30</b>
4.1	Introduction . . . . .	31

4.2	X-ray faint active galaxy populations . . . . .	32
4.3	Active Galaxy Properties . . . . .	33
4.3.1	Stellar mass distributions and quasar contamination . . . . .	33
4.3.2	Stellar mass functions . . . . .	39
4.3.3	Luminosity functions . . . . .	42
4.4	Conclusions . . . . .	43
<b>5</b>	<b>Investigating the origin of infrared variability in AGN</b>	<b>45</b>
5.1	Introduction . . . . .	46
5.2	Variability dependence on wavelength . . . . .	48
5.2.1	Infrared variability spectrum . . . . .	51
5.3	Origin of Variability in AGN . . . . .	51
5.4	Spectral energy distribution analysis . . . . .	55
5.4.1	Mass Matching . . . . .	55
5.4.2	Calculating spectral energy distributions . . . . .	55
5.4.3	SED comparison . . . . .	57
5.5	Stellar Populations . . . . .	58
5.6	Variability timescale . . . . .	59
5.7	Conclusions . . . . .	63
<b>6</b>	<b>Science Chapter 3</b>	<b>66</b>
6.1	Introduction . . . . .	66
6.2	Data and sample selection . . . . .	66

6.2.1	Ground based UDS field . . . . .	67
6.2.2	Space based CANDELS field . . . . .	67
6.3	Determining host galaxy parameters . . . . .	68
6.4	Calculating environmental density . . . . .	70
6.5	Results . . . . .	70
6.5.1	Environment . . . . .	70
6.5.2	Infrared and optical colour comparisons . . . . .	71
6.5.3	Host galaxy comparison . . . . .	78
<b>7</b>	<b>Conclusions and Future Work</b>	<b>81</b>
7.1	Conclusions . . . . .	81
7.2	Future work . . . . .	81
<b>Bibliography</b>		<b>81</b>

## **Abstract**

Abstract

## Acknowledgements

My first thanks go to my supervisors Omar and Mike, who – in the most literal way – I could not have done this PhD without. I’m so sorry about all the stupid questions, but thank you for answering them anyway.

Next, I’d like to thank the people who were also my supervisors in every way except formally: Dave and Lizzie. Doing a PhD is no easy task, and helping someone else with one is all the more difficult. It cannot be stressed enough that few people would be able to obtain a PhD without the effort of postdocs and more senior PhD students, with myself being the primary example of this. I am sorry about all the stupid questions though, but thank you for answering them anyway.

Thank you to the actual backbones of the astronomy department: Phil, Margaret and Ella. All three of you are literal angels.

Thank you to my fellow 2019 starters Clár-Bríd, Tomáš and Stephane. It was the worst of times for us I’m afraid, but misery loves company and we all made it through in the end.

I cannot thank my wider gals community enough: CB, Lizzie (Lizzie T.), Kellie, Sophie, Molly, Rowann, Charutha, Stephane, Jen, Isabel, Kira, Paris (and a honorary James). Gaining confidence through kindness is a rare blessing. I thank you all for giving it to me.

To the DA: Mick, Baresca and Roan, you were certainly people I met during my PhD (thank you). To Sukhi and Simon, I owe you both a lot, but neither of you mentioned me in your thesis acknowledgements, so you’ve made an enemy of me. Know that I will never forgive you for that (thank you).

Thank you to other PhD friends both old and new, Lizzie (Lizzie E.), Amy, Julian, Jimi, Swagat, Shaun, Tom, Leo, Dan, Matt, Brad, Mikey and many more. I couldn’t have picked a better group to go insane with.

Thank you to my undergrad OG’s Pruthvi, Rachel and Abbie, for sticking with me for 10+ years. The 100’s of hours of voice messages we’ve sent each other were the only things keeping me going at times. I can only hope for 10 more.

Finally, thank you to my family - Mum, Dad, Shawna (+ Nico + Tibby) - for always

ensuring I was doing something but never caring what it was. Your gentle encouragement lead me beyond the stars.

## **Equality Diversity and Inclusion**

## Published works

Material presented in this thesis has already been published in — or is in preparation for submission to — a journal as the following works:

- I **Green K.**, Elmer, E., Maltby, D., Almaini, O., Merrifield, Hartley W. G., 2024, MNRAS, 531, 2: ‘*Increasing AGN sample completeness using long-term near-infrared variability*’.
- II **Green K.**, Elmer, E., Maltby, D., Almaini, O., Merrifield, Hartley W. G., 2024, MNRAS, in preparation: ‘*Investigating the origin of infrared variability in AGN*’.

The vast majority of work presented here was carried out by the author, with advice from the paper authors above. Where the work contains the product of larger collaborations, this is mentioned in the relevant chapter.

# **Chapter 1**

## **Introduction**

## 1.1 Extragalactic Astronomy

The general goal of astrophysical research is to understand how the Universe evolved into what we see today. Though it is now well understood that the Milky Way is just one of many galaxies in the Universe, the fact that other galaxies exist was a major scientific breakthrough in of itself. One of the earliest recorded observations of galaxies beyond the Milky Way can be seen in the '*Book of fixed stars*' by Iranian Astronomer Abū al-Ḥusain al-Ṣūfī in 964AD. Here the Andromeda galaxy was identified, and it was noted that it had a smeared appearance, which was unlike other celestial bodies in the sky (Hafez, 2010). These bodies largely remained a mystery until the philosopher Immanuel Kant presented the idea of “island universes”, meaning other galaxies, as an explanation for the observed “nebulae of unknown nature”. This theory of other galaxies was a major argument in the ‘*Great Debate*’ (Curtis, 1988) and was finally confirmed by the early 20<sup>th</sup> century, when Hubble measured the distance to one such spiral nebulae and proved it was truly extragalactic in nature (Hubble, 1925). This confirmation that objects exist beyond the edge of the Milky Way opened up the extragalactic research field, as the nature of these objects would need to be understood before new models of the Universe could be suggested.

As the number of galactic surveys increased, it was quickly found that galaxies have a range of properties. Edwin Hubble classify these galaxies based on their visual morphology in increasing complexity, and this resulted in the first iteration of the Hubble sequence (Hubble, 1926). This sequence was then completed by Allan Sandage after Hubble’s death (Sandage, 1961), which built the Hubble Tuning Fork classification scheme that is popular today (Figure 1.1). Beyond morphology, measurements of extragalactic spectra found that spectral lines were shifted compared to galaxies are not static, but have a velocity relative to the Milky Way. The radial velocity was of Andromeda was first measured by Slipher 1913, who used the blueshift of the galaxy’s spectrum to calculate the speed of approach. This idea was then extended in Hubble 1929 where it was noticed that the more distant a galaxy, the faster its speed of recession. This marked the development of Hubble’s law as well as providing empirical evidence for the expanding Universe theory.

Amongst these discoveries, it is important to note that a class of galaxies with peculiar visual and spectral features were observed. These galaxies are now known as ‘active

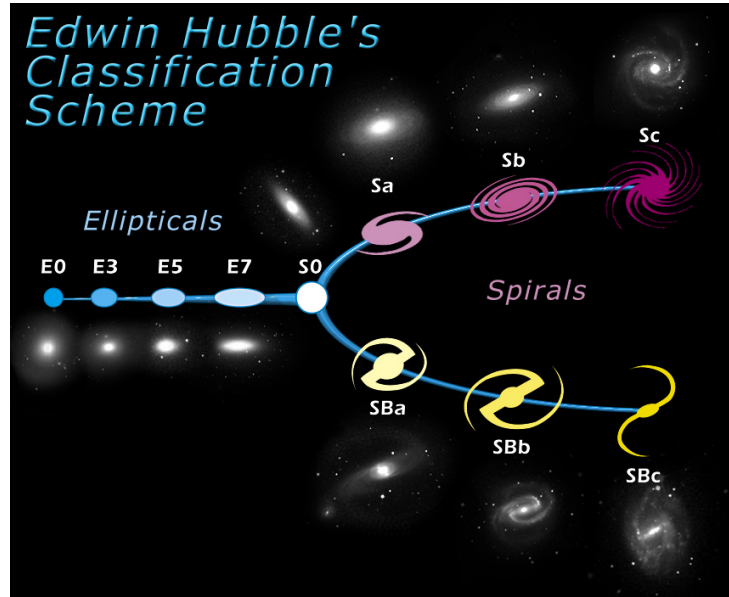


Figure 1.1: The Hubble sequence as devised by [Hubble 1926](#) and updated by [Sandage 1961](#). Image taken from [information@eso.org](mailto:information@eso.org) (1999). Galaxies are ordered according to their visual complexity, progressing from elliptically (left) to lenticulars in the centre. Spiral galaxies form the right of the diagram, with barred-spirals on the bottom and non-barred, "normal", spirals at the top.

galaxies' and it is this galaxy group we explore in the following section.

## 1.2 Galaxies

In order to understand the active galaxies, we must first explore the general features of galaxies. In modern astrophysics, galaxies are generally recognised to be structures where a collection of matter is bound in orbit to a supermassive black hole (SMBH). As discussed in Section 1.1, there galaxies can have a range of properties, however it is believed that most, if not all galaxies contain a supermassive black hole (SMBH) in the centre. Many relations have been reported between black holes and the properties of the host galaxy that implies the formation and evolution of the two are heavily linked, and active galaxies are no exception to this. The accretion of matter onto a black hole is the current leading theory for the emission observed from active galaxies and as such understanding black holes is required to understand active galaxies in general.

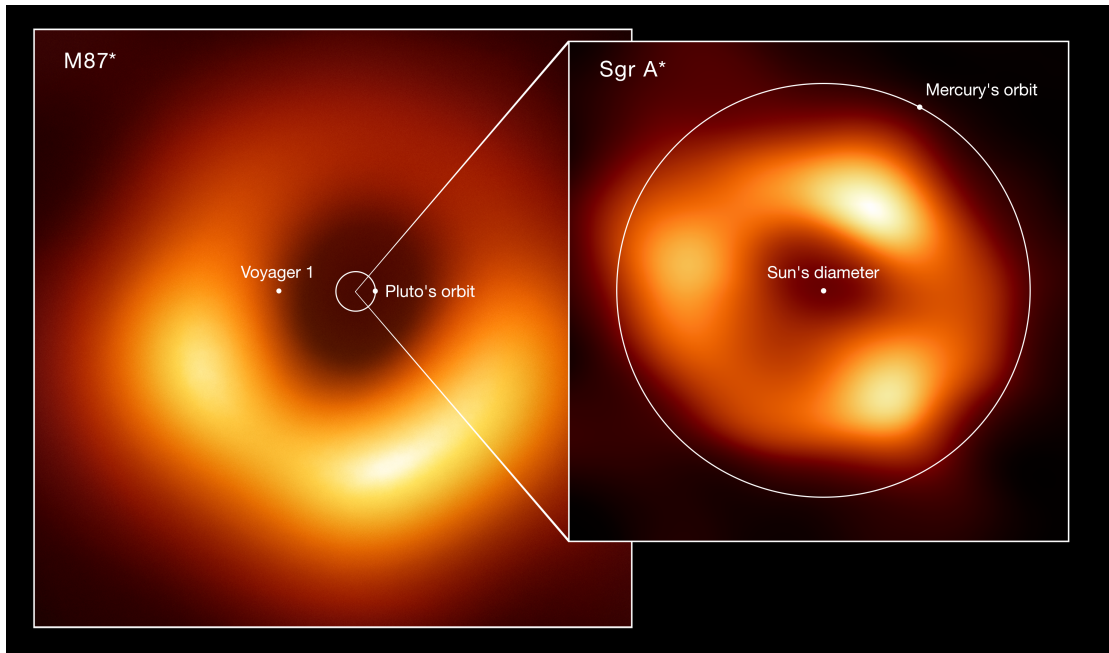


Figure 1.2: Image of the event horizon about the black hole in the galaxy Messier 87 (left) as well as the event horizon of Sagittarius A\* (right). Various properties of Solar System objects are shown on the images to illustrate the relative scales of the black holes (Collaboration et al. 2019; Collaboration et al. 2022).

### 1.2.1 Black Holes

Black holes are defined as regions of spacetime so dense that nothing, not even light, can escape. A simplistic model places a singularity - a point of infinite density and zero volume - at the centre of the black hole, and the Schwarzschild radius defines the region around it where information cannot escape. The idea of black holes can be seen as early as [Michell 1784](#), who used Newtonian physics to show that, if a star was dense enough, its escape velocity would be greater than the speed of light. Though the idea of massive, invisible stars is an exciting theory, the interest in this did not last, as the wave-like properties of light were discovered and its assumed-zero mass lead scientists to believe it would be largely unaffected by gravity.

The concept of black holes became relevant again in the early 20<sup>th</sup> century when Einstein developed his theory of general relativity (GR; [Einstein 1916](#), eng. translation: [Einstein et al. 1920](#)). His field equations described gravity as a bending of space-time which could therefore impact light, and Schwarzschild quickly discovered a solution to these equations defining the a region from a singularity where light could not escape

(Schwarzschild 1916, eng. translation: Schwarzschild 1999). The exact nature of the resulting surface formed by the Schwarzschild radius remained a mystery until 1958, where physicist David Finkelstein described it as ‘a perfect unidirectional membrane’ where influences could only pass beyond the surface in one direction, indicating that particles could not escape it (Finkelstein, 1958). The edge of space, just beyond the Schwarzschild radius, is now known as the black hole event horizon (Rindler, 1956) and this is the closest one can get to observing a black hole directly. As such, it is the interaction of gravitationally bound matter as well as the bending of light that allows for the study of black holes.

Outside of theory predictions, there is a wealth of evidence for the existence for black holes including:

1. The X-ray binary system Cygnus X-1 is one of the brightest and well studied X-ray sources in the night sky (Webster & Murdin, 1972). Here, the mass of the non-stellar source has been estimated to be on the order of  $10M_{\odot}$ , well above the upper limit for a neutron star. From this it is widely believed that the binary pair is comprised of a black hole and a star (Herrero et al., 1995).
2. Measurements of the proper motion of stars about the galactic centre of the Milky Way was used to estimate the mass of Sagittarius A\* in Ghez et al. 1998 and Genzel et al. 2010. Based on mass and radius estimates, the authors concluded that Sagittarius A\* is a black hole.
3. In September 2015, gravitational waves were detected at the Laser Interferometer Gravitational-wave Observatory (LIGO). It was concluded that the waves originated from a merger of a pair of black holes, as the measured shape matched the GR prediction for such an event (LIGO Scientific Collaboration and Virgo Collaboration et al., 2016).
4. One of the most recent and compelling arguments for the existence of black holes comes from the images of multiple black hole event horizons. The first image released was of the event horizon for the black hole in active galaxy Messier 87 (M87). The second ever image of an event horizon was taken of Sagittarius A\*, the black hole in the centre of the Milky Way. These are pictured in Figure 1.2 (Collaboration et al. 2019, Collaboration et al. 2022).

5. Finally, in the following sections we detail the discovery and structure of active galaxies. Active galaxies are distinguished from inactive or "regular" galaxies by the presence of an active galactic nuclei (AGN). AGN are thought to be powered by black hole accretion which results in the observed coherent changes in flux across the electromagnetic spectrum. The existence of AGN, and more specifically the observed variability in their emission, is arguably the most convincing evidence for the existence of black holes as outside of black hole accretion, it is difficult to reproduce this observed feature (Rees 1984; Green et al. 1993).

Having explored black holes as a key feature of galaxies, we now return to the specifics of active galaxies.

## 1.3 Active Galaxies

### 1.3.1 Discovery of Active Galactic Nuclei

Active galaxies are galaxies that host an active galactic nucleus (AGN). Active galaxies are extremely powerful systems, being one of the few objects to emit across the entire electromagnetic spectrum (e.g., Edelson & Malkan 1987; Collier & Peterson 2001; Cackett et al. 2021), and the central AGN engine is believed to be powered by accretion onto a super massive black hole (Salpeter 1964; Kormendy & Richstone 1995).

As previously stated, AGN emission causes active galaxies have different visual and spectral features compared to an inactive galaxy. For this reason, though it was not known, AGN emission has been observed as early as the beginning of the 20<sup>th</sup> century. In Fath 1909, 'spiral nebulae' were being observed to determine if their spectra was truly continuous, as commonly claimed at the time. Amongst the objects studied, NGC 1068 stood out, as it showed both absorption and emission lines compared to other objects which had little to no emission lines in their spectra. Similarly, in measuring the spectrum of NGC 1275, Humason 1932 noted that the nuclear component of the galaxy appeared near-stellar compared to other objects that did not show excess light in the centre. Finally, Seyfert produced his now seminal paper, Seyfert 1943, where he measured the properties of a unique class of objects that would eventually be known as "Seyfert galaxies". He noted that, in agreement with Humason 1932, the nucleus of

these galaxies appear bright and point-like, but also showed unique spectral properties, having broad emission lines with the width of seemingly correlating with the luminosity of the nucleus as well as the nuclear-to-host light ratio. These studies formed the early history of AGN discovery and proved that active galaxies formed a different group of galaxy compared to inactive galaxies in the Universe.

Completing the history of the AGN observational timeline, it was only with the discovery of high energy, radio-loud quasars that the historical measurements of active galaxies were popularised and AGN physics became a real area of interest. In [Baade & Minkowski 1954](#), discussion of discrete radio sources found that the spectrum of Cygnus A, a radio-loud galaxy, to be similar to the spectrum of NGC 1275, one of the six original Seyfert galaxies. Following this, [Schmidt 1963](#) identified the radio-loud active galaxy 3C 273. The authors state that 3C 273 is extragalactic in nature, and appears as a star-like nucleus with a radio jet outflow and as more of these extra-galactic ‘quasi-stellar’ radio sources were identified, they were given the name ‘quasars’ in the literature. Over time, it was realised that quasars and Seyfert galaxies are likely the same type of object emitting at different energy ranges, and in generalising these objects the active galaxy theory was formed, with Seyferts and quasars forming specific sub-classes of active galaxies.

### 1.3.2 AGN and the evolution of the Universe

Beyond understanding how they work, active galactic nuclei activity has been used as a key component in describing the evolution of the Universe.

In the early universe it is believed that AGN activity drove helium reionisation. The epoch of reionisation begins when the first stars (population III stars) produce photons that are energetic enough to ionise neutral hydrogen in the Universe ([Dayal et al., 2020](#)). Though population III stars are largely thought to drive the earliest emission in the Universe, active galactic nuclei activity is credited as being the main driver of the subsequent ionisation of Helium ([Volonteri & Gnedin 2009; Eide et al. 2020](#)).

The effects of AGN emissions can also be seen in large scale structure within the Universe. In galaxy clusters, the brightest cluster galaxy is more likely to be a radio loud AGN than an inactive galaxy at the same stellar mass. This forms an important observation as the feedback from the radio jets from such galaxies is the current most accepted solution

to the cooling flow problem observed in galaxy clusters (Best et al., 2007).

Outside of the solutions AGN emission poses to structures within the Universe, there have been many observations between the properties of black holes the properties of the galaxies they exist in, implying the evolution of the two are linked despite the different physical scales they exist on.

The first is the known Mbh-Mbulge - observations

AGN accretion - SFR history - observations

Mph-sigmabulge - observations

### 1.3.3 AGN structure

Having described the historical observations of AGN, we now address modern views of the underlying structure and emission from active galaxies.

In the contemporary view, an AGN consist of a black hole that is actively accreting material from its surroundings (Alloin et al., 2006). From the central black hole outwards, the accreting material takes the form of an accretion disk and surrounding both the disk and black hole is an electron plasma moving at relativistic speeds. Beyond this electron corona are clouds of gas bound to the system, which produce broad and narrow emission lines depending on their proximity to the black hole, and at the edges of the system there is a surrounding dusty, torus-like object that feeds into the accretion disk. The final component is a pair of relativistic jets, anti-parallel to each other, however these are only observed in  $\sim 10\%$  of AGN. A diagram of an AGN system can be seen in Figure 1.3.

In addition to the physical structure of the system, one of the defining observational features of AGN is their broad-band radiation. The flux from inactive galaxies is dominated by stellar emission, and as such the spectra of these galaxies typically consists of a superposition of blackbody spectra, over a relatively narrow wavelength range. AGN, on the other hand, have a range of distinct observational features (Dermer & Giebels 2016; Padovani et al. 2017) and are one of the few known objects to have been observed in every waveband in the electromagnetic spectrum (See Figure 1.4). Though

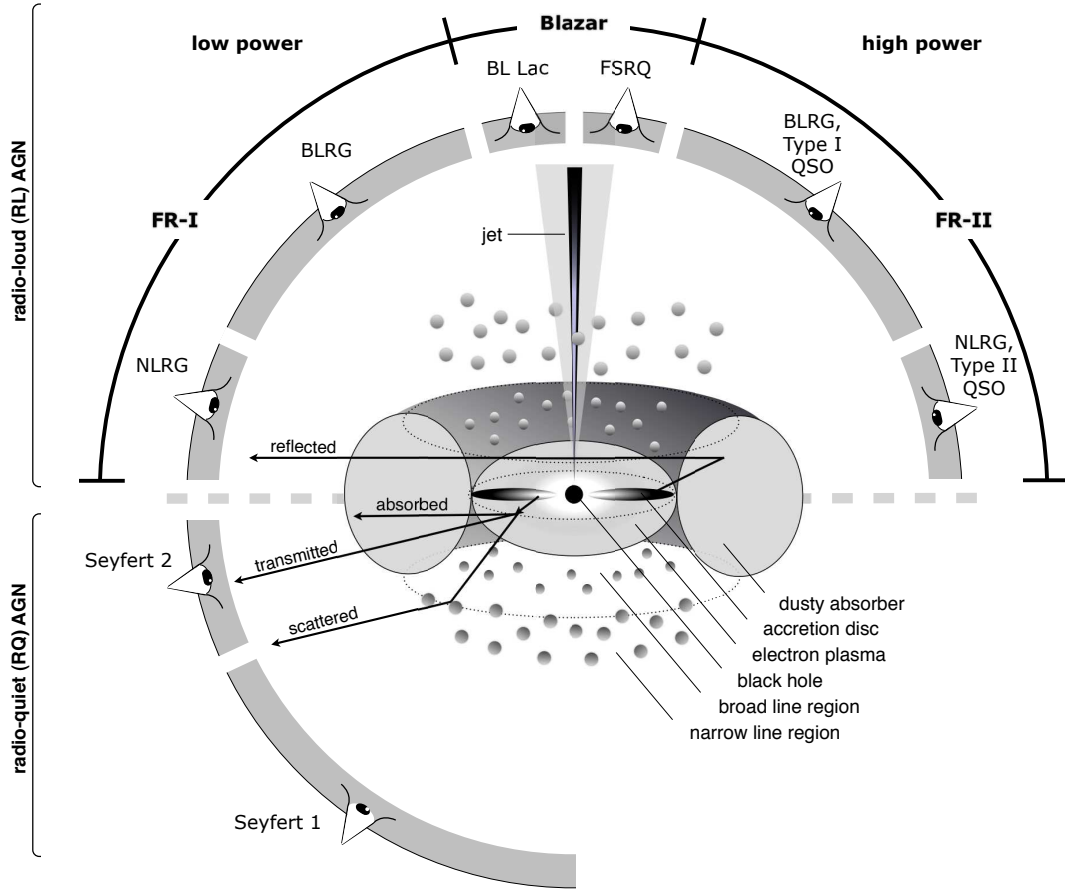


Figure 1.3: Diagram of the main components of an AGN, taken from Beckmann & Shrader (2013). Note that jets in radio-loud AGN are thought to be symmetric and the true shape of the dusty absorber is not confirmed to be a perfect torus.

the processes that drive multi-wavelength AGN emission is still not fully understood, Antonucci 1993 provided the current leading model for AGN structure and emission. This unified model states that all AGN are driven by the same black hole accretion process, however the observed differences in AGN types is due to different viewing angles between a given active galaxy and the observer. This theory suggests plausible structures for the nuclear regions of an active galaxy as well as reproduces broadband AGN emission.

Connecting components of an AGN to the radiation produced, the bulk of AGN emission is attributed to the accretion disk (Salpeter, 1964). Here, surrounding matter falls towards the central supermassive black hole and this matter takes the form of an optically thick

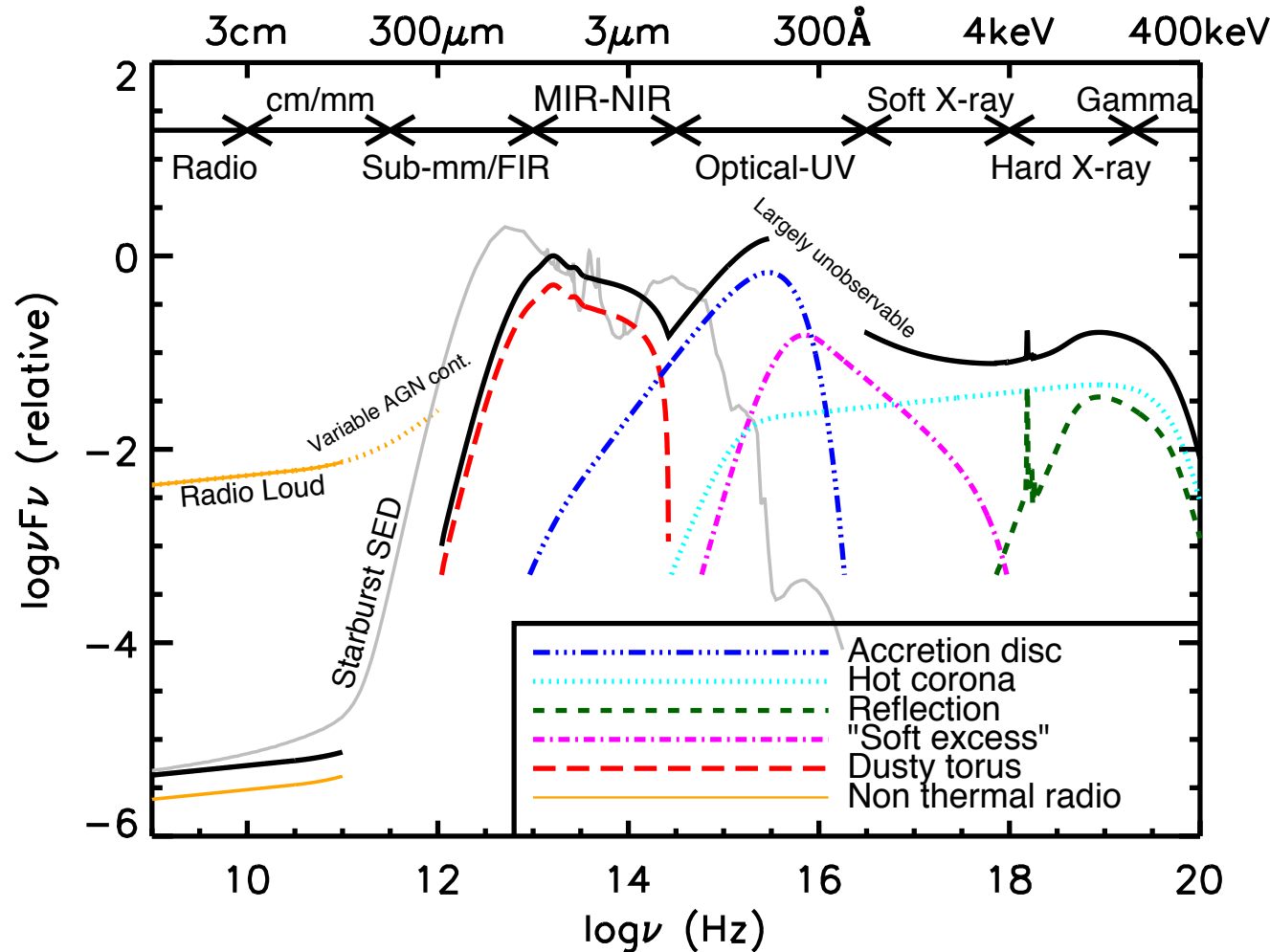


Figure 1.4: An AGN spectral energy distribution (SED), taken from [Harrison 2014](#) and [Hickox & Alexander 2018](#). Here the black solid line shows the overall emission and the coloured curves show individual components. The coloured curves have been offset from the total-emission curve for clarity.

(light is readily absorbed) but geometrically thin (small width or thin in the vertical direction) disk. The accretion disk is viscous enough that the differential rotation of the material induces shearing at adjacent radii. Angular momentum and gravitational energy is converted into electromagnetic (EM) radiation as well as kinetic energy, and the heated matter is blown out as accretion disk as "winds". The EM radiation of disk is typically in the optical/UV frequency range, and this forms the "big blue bump" of the AGN SED (Netzer 2013; Panagiotou et al. 2022).

Following from the accretion disk, optical and UV photons travel to the electron plasma, and are inverse Compton scattered to X-ray wavelengths. This interaction produces X-ray radiation and forms the X-ray corona of the AGN. Moving further out the system, the broad line region (BLR) is reached. Here clouds of gas are bound to the black hole and orbit at extremely high speeds. As such, any emission lines from this region is widened due to Doppler broadening, and the production of these broad-emission-lines gives the region its name. Further out from the BLR is the narrow line region (NLR). Also comprised of clouds of gas, these clouds exist at a lower density and orbit at a higher radius from the black hole. Their lower orbital speed leads to little or no broadening of the emitted radiation from these clouds, resulting in standard emission lines at specific wavelengths.

The edges of the AGN system is formed by a surrounding dusty obscurer/absorber. The specific shape of this object is still up for debate, as it is unlikely to be a perfectly smooth and rounded torus, however it is likely to exist in a ring around the accretion disk. This dusty object, referred to from now as the dusty torus, is comprised of dust that is heated by the nuclear-produced photons of the accretion disk, which is then absorbed and reprocessed into the infrared (IR).

About 10% of AGN are observed to be radio-loud, and in these cases the AGN are thought to have a pair of anti-parallel, relativistic jets that also serve as an explanation for gamma-ray emission in the galaxy. Radio emission originates from the synchrotron process within the jets, where relativistic electrons radiate EM radiation in the form of radio waves as they accelerate through a magnetic field. Jet activity also gives rise to gamma ray production in AGN, as "seed" photons from the accretion disk, dusty torus, BLR and NLR clouds or the synchrotron emission in the jet itself is inverse Compton scattered to gamma ray wavelengths by the jet-bound electrons (Madejski & Sikora, 2016).

Finally, to conclude this section we revisit the AGN unification theory (Antonucci, 1993), where it is stated that all types of AGN have effectively the same structure, but the viewing angle, presence of jets, as well as the power of the AGN itself determines the type of active galaxy that is ultimately observed. In type I active galaxies, the AGN is viewed from the "top-down" such that the dusty torus does not intervene between the observer and all AGN emission is unobscured. In contrast to this, type II active galaxies are viewed "through" the dusty torus, and as such areas closer to the core such as the broad line region are not observable, leading to only the narrow lines of these objects to be measurable.

The multiple processes within the unified theory of AGN emission interconnect to reproduce the wide range of wavelengths observed from the objects, but in addition to this the mechanisms are flexible enough to allow for variability in the radiation. Irregularity in flux is a quality that is intrinsic to AGN emission and it is this characteristic that is described in Section 1.4.

### 1.3.4 AGN detection methods

## 1.4 Variability

A key feature of the broad-band emission from AGN is that it is not static, but varies in flux in every wavelength in which it has been observed (e.g., Fitch et al. 1967; Sánchez et al. 2017). This variability has been studied in detail since their discovery (e.g., Smith & Hoffleit 1963), and has been found to be aperiodic in nature. Hypotheses into the origin of variability point to stochastic processes within the AGN itself, with UV and optical variability originating from instabilities in the accretion disk, which has a knock on effect causing irregularities in the X-ray output of the corona as well as IR emission in the dusty torus. Variability in radio and gamma-rays however, likely arise from jet-related processes as well as uneven seed photons production from the accretion disk (Netzer 2013; Bianchi et al. 2022).

Despite the high power output and range of emission wavelengths AGN produce, the small physical size of an active galaxy's central engine means that accretion and emission occurs on scales many orders of magnitude smaller than that of the host galaxy.

Consequently, resolving the central nucleus is simply not feasible for galaxies outside our local neighbourhood (e.g., Padovani et al. 2017) making AGN difficult to study. The difficulty in unpicking AGN emission from that of its host galaxy also poses a significant barrier in understanding the structures present within an AGN, and the impacts of the accretion process on the surrounding region (Grogan et al. 2005; Gabor et al. 2009; Pierce et al. 2010; Fan et al. 2014). As such, AGN variability is an important tool in the study of active galaxies, as variability observations are limited by light-travel times, allowing for small scales to be indirectly probed.

Since the speed of light in a vacuum is a known physical quantity, the timescale that AGN variability takes place on can be used to characterise the emitting region of the system. Such variability studies have produced key pieces of evidence for AGN emission theories, such as mass and radius estimates favouring black holes over other objects as the nuclear body in the emission process (Green et al., 1993). Variability timescales have also been found to increase with wavelength, for example, emission at higher frequencies, such as X-rays, vary within hours, while UV and optical variations take days to weeks. The longer wavelengths, such as infrared (IR), typically vary on timescales of months or years (e.g., Berk et al. 2004). Since this variability is coupled to structures within the AGN itself, it allows for the study of AGN on the relatively tiny scales they span compared to the size of a galaxy.

Infrared variability is uniquely useful in the study of AGN, as IR measurements probe the dusty torus-like structure on the edges of the AGN system as material from it feeds the accretion disk as well as being able to probe dusty galaxies and rest-frame optical emission for galaxies at higher redshift. Unfortunately, the timescale of variability in the IR is several months to years, and this time cost has limited the research in this regime compared to variability in higher frequency wavebands. The Ultra Deep Survey (UDS, Chapter 2), however, provides a solution to the obstacles preventing IR variability studies, as it has 8 years of deep, near-IR imaging. The  $\sim 1\text{deg}^2$  imaging has collected the time-intensive data required for significant IR variability to be observed and these deep observations provide the perfect dataset for the study of infrared variability in active galaxies.

AGN emission is invoked across many aspects of galaxy evolution to help explain observed phenomena, but this activity, and the underlying mechanisms that drive it, is still not fully understood. As a result, despite many theories within the literature,

there is no firm consensus on the potential trigger (or triggers) that activates an AGN. Furthermore, we are currently unable to observe any given galaxy and know with certainty how and why it is, has been, or will become, active in its lifetime. In order to determine robust answers for these questions, a complete census of active galaxies in the Universe is necessary to allow for the study of the cosmic evolution of AGN and a complete understanding of the active galaxy system in of itself must be known.

### **1.4.1 X-ray**

### **1.4.2 UV and Optical**

### **1.4.3 Infrared**

### **1.4.4 Gamma and Radio**

## **1.5 The host galaxies of active galactic nuclei**

## **1.6 Thesis Structure**

The research presented in this thesis selects a sample of active galaxies based purely on their near-infrared variability. It then compares the properties of this sample to active galaxies selected through X-ray emission, which is a technique more commonly used in scientific research. The variability detected active galaxies are then further grouped, based on the IR waveband of detection, and the properties of these are investigated to deduce possible structures in active galaxies as a whole.

In Chapter 2, we describe the data used in this research. We make use of the UKIDSS UDS, which was taken on The UKIRT Wide Field Camera (WFCAM). We detail the multi-wavelength catalogues of the field as well as how redshifts and stellar masses were calculated. We also describe the X-ray imaging of the UDS field and its comparative coverage.

In Chapter 3 we explain the method used to select AGN based on their NIR variability in the  $J$  and  $K$ -bands. We describe the cleaning of the dataset after selection, as well as how variability amplitudes are measured and how detection limits of the survey are calculated.

Chapter 4 consists of a comparison between the properties of active galaxies selected through NIR variability, and active galaxies selected by X-ray emission.

In Chapter 5 we split the NIR variable active galaxies based on their variability in the  $J$  and  $K$ -bands. We then investigate if the properties of the galaxies are different depending on the band they are variable in.

Chapter 6 - AGN variability + host galaxy properties

Finally, in Chapter 7, we summaries the results and present the overall conclusions of the work.

Much of the method described in Chapter 3 and the research shown in Chapter 5 is published in Paper I. The work presented in Chapter 5 and the accompanying method described in Section 3.5 is in preparation to be submitted in Paper II. All magnitudes stated are AB magnitudes. We use a  $\Lambda$  cold dark matter ( $\Lambda$ CDM) cosmology, with  $H_0 = 70 \text{ kms}^{-1}\text{Mpc}^{-1}$ ,  $\Omega_\Lambda = 0.7$  and  $\Omega_m = 0.3$ .

# Chapter 2

## Data

In this work, we make use of data from multiple deep surveys: the UKIDSS Ultra Deep Survey (UDS; Almaini et al., in prep); combined with the *Chandra* Legacy Survey of the UDS field (X-UDS; [Kocevski et al. 2018](#)). A plot of the extent of the fields is shown in Figure 2.1.

### 2.1 UDS

The UDS is the deepest of the UKIDSS surveys ([Lawrence et al., 2007](#)) and the deepest NIR survey over  $\sim 1 \text{ deg}^2$ . Its *JHK* band imaging was taken over an 8 year period from 2005–2013 using the WFCAM instrument at UKIRT ([Casali et al., 2007](#)). Although not primarily designed to study variability, the collection of the data spread over eight years offers a powerful resource for long-term infrared variability studies. In addition to this, the field is well studied and as such has additional imaging in many other wavebands including:

- $u'$ -band imaging from the Canada–France–Hawaii Telescope (CFHT) MegaCam.
- $B$ ,  $V$ ,  $R$ ,  $i'$  and  $z'$ -band optical imaging from the Subaru *XMM-Newton* Deep Survey (SXDS; [Furusawa et al., 2008](#)).
- $Y$ -band imaging from the VISTA VIDEO survey ([Jarvis et al., 2013](#)).

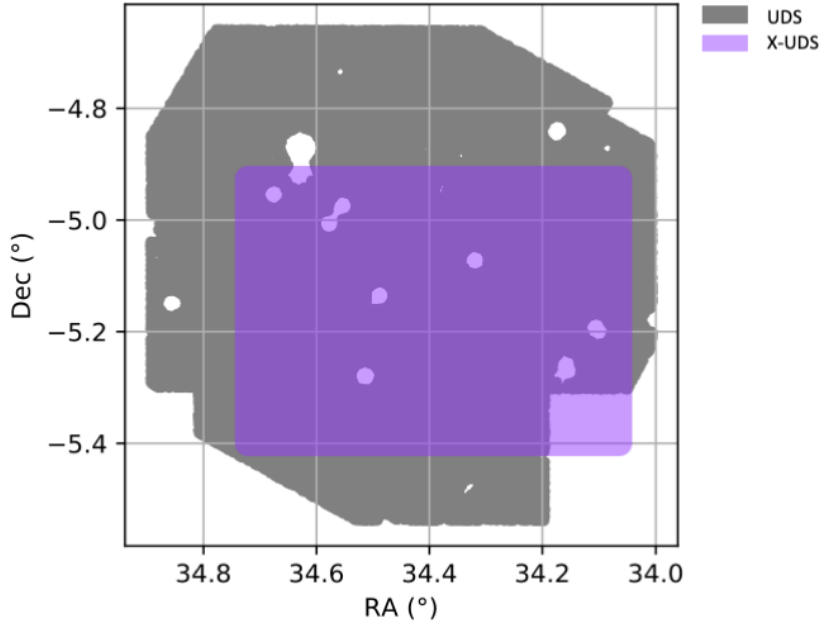


Figure 2.1: The survey region of the Ultra Deep Survey (UDS) and the *Chandra* Legacy Survey of the UDS field (X-UDS). The grey shaded area shows the subset of the ground-based UDS field where there is reliable photometry in all 12 photometric bands, and the purple shaded area shows the coverage from the *Chandra* X-UDS imaging.

- $3.6\mu\text{m}$  and  $4.4\mu\text{m}$  mid-infrared (MIR) IRAC imaging from the *Spitzer* UDS Legacy Programme (PI: Dunlop).

The DR11 is the latest data release from the Ultra Deep Survey (UDS). This data release has 296,007  $K$ -band detected sources and  $5\sigma$  limiting depths of  $J = 25.6$ ,  $H = 24.8$  and  $K = 25.3$  (AB in 2-arcsec diameter apertures; Almaini et al. 2017; Almaini et al., in prep.). From this data release we make use of the ‘*best galaxies*’ subset which covers  $0.62\text{ deg}^2$ , and comprises objects identified in unmasked regions of the field with reliable photometry in all 12 bands, the deepest IRAC imaging, and with galactic stars removed. Masked regions correspond to boundaries of the science image, artefacts, bright stars and detector cross-talk. The *best galaxies* subset contains 202,282  $K$ -band detections.

### 2.1.1 Redshifts

Of the 202,282 galaxies, 6558 have secure spectroscopic redshifts provided by complementary spectroscopic surveys (e.g., UDSz, VANDELS; Bradshaw et al., 2013; McLure

et al., 2013; Maltby et al., 2016; McLure et al., 2018; Pentericci et al., 2018). For non-variable objects, spectroscopic redshifts are used (where available); otherwise, photometric redshifts are adopted.

Photometric redshifts for non-variable objects were calculated according to the methodology described in Simpson et al. (2013). For this, the 12-band photometry was fit using a grid of galaxy templates constructed from the stellar population synthesis models of Bruzual & Charlot (2003), and used the publicly available code `EAZY` (Brammer et al., 2008). These photometric redshifts have a typical accuracy of  $\frac{\Delta z}{(1+z)} \approx 0.018$ . Additional properties used in this work (e.g. stellar mass and luminosity; Almaini et al., in prep), are based on these redshifts and are entirely adequate for our purposes.

In this paper, we identify IR-variable objects (see Section 3.1). For these objects, spectroscopic redshifts were used (where possible) over photometric determinations. For the variability detected sources for which spectroscopic redshifts were not available, inaccuracies in the photometric redshifts are a potential concern due to the AGN emission not being accounted for. To address this, we have recalculated the photometric redshifts for these objects via the `EAZY` redshift fitting code. Here additional reddened and unreddened AGN templates were included in the fitting. Comparing the median absolute deviation of  $\frac{\Delta z}{(1+z)}$  before and after including the recalculated photometric redshifts, indicates the redshifts improve only marginally from  $\sigma_{\text{MAD}} = 0.10$  to  $\sigma_{\text{MAD}} = 0.098$ . This demonstrates the initial photometric redshift values to be largely robust. Regardless, the recalculated redshifts for the IR-variable active galaxies are used throughout this work, though we note that using the original photometric redshifts made no significant difference to our analysis or conclusions.

### 2.1.2 Stellar Masses

Stellar masses (Almaini et al., in prep), were calculated using the method described in Simpson et al. (2013). Here, the 12-band photometry was fit to a grid of synthetic SEDs from the stellar population models of Bruzual & Charlot (2003) with a Chabrier (2003) initial mass function. Typical uncertainties in these stellar masses are of the order  $\pm 0.1$  dex. The redshift-dependent, 90 per cent stellar mass completeness limits were calculated using the method described in Pozzetti et al. (2010). A second order polynomial was fit to the resulting completeness limits across a wide redshift range to

give a 90 per cent mass completeness curve of the form  $\log_{10}(M_*/\text{M}_\odot) = -0.04z^2 + 0.67z + 8.13$ .

## 2.2 X-UDS

The X-UDS survey is a deep X-ray survey of a sub-region of the UDS field carried out by the *Chandra* X-ray Observatory's Advanced CCD Imaging Spectrometer (ACIS). It comprises a mosaic of 25 observations of 50 ks exposure, totalling 1.25 Ms of imaging. It covers  $0.33 \text{ deg}^2$  in total (Kocevski et al., 2018) and has a flux limit of  $4.4 \times 10^{-16} \text{ erg s}^{-1} \text{ cm}^{-2}$  in the full band (0.5–10 keV). In total, 868 point sources were identified.

This data set was matched to the UDS DR11 *K*-band catalogue using the methodology described in Civano et al. (2012), which adopted the maximum likelihood method described in Sutherland & Saunders (1992). Through this analysis, we find that 710 of these point sources are associated with *K*-band-selected galaxies in the UDS DR11.

## 2.3 CANDELS

[GalfitM data needs to go here]

# **Chapter 3**

## **Quantifying AGN variability**

### 3.1 Selecting AGN based on their IR variability

IR-variable AGN are selected from the UDS DR11 using the technique first developed and used in [Elmer et al. \(2020\)](#). Here, the authors were able to construct NIR light curves from multiple flux measurements that spanned 7 semesters in the  $K$ -band. Errors on the flux measurements were self-calibrated, based on the population variance in flux of the non-variable objects, as this provided a better fit to the data than the errors generated by SExtractor (see Figure 3. in [Elmer et al. 2020](#)). To do this, the authors began by convolving each semester stack of images with a Gaussian kernel to match the stack with the poorest quality PSF. This ensured that the differences in flux measurements were due to intrinsic AGN variability and not changes in the point spread function from semester to semester. A preliminary  $\chi^2$  analysis was then performed to remove the most variable sources and the remaining light curves were normalised and split into bins based on flux, epoch and quadrant. From this the standard deviation of the binned flux values provided the photometric error on the measurements for the objects in that bin.

After the publication of [Elmer et al. 2020](#), additional  $J$ -band imaging was incorporated into the dataset. First an updated catalogue of galactic stars was developed for the UDS DR11 release, none of which were included in the initial  $K$ -band sample selection. These stars were used to improve the PSF images prior to convolving the data to match the semester with the poorest PSF (see Section 2.2 of [Elmer et al. 2020](#)), allowing for an improved sample selection in the  $K$ -band. Furthermore, the 2006B semester in the  $J$ -band had sufficient observations to allow it to be included in the light curves. This gives the  $J$ -band a total of 8 epochs for study.

We further select only objects with reliable (unmasked) photometry in all 12 bands, to ensure the most reliable photometric redshifts. Objects identified as galactic stars were excluded, as were any galaxies close to cross-talk detector artefacts. We also exclude any objects with formally negative flux values in any individual semester, as described in [Elmer et al. \(2020\)](#). This final step largely excluded very faint galaxies at  $K > 25$ , close to or beyond the formal detection limit of the survey. Inspecting this faint subgroup reveals that all would be excluded by the eventual  $J$ -band magnitude cut described in Section 3.4, so have no impact on our analysis. Overall, these rejection criteria yield a final sample of 114,243 light curves for this study.

Errors on the flux measurements were self-calibrated, based on the population variance

in flux of the non-variable objects at the same apparent magnitude, as this provided a better fit to the data than the errors generated by SExtractor (see Figure 3 in Elmer et al. 2020). A full description of this process can be found in Section 2.2 of Elmer et al. (2020).

IR-variable AGN were selected using a  $\chi^2$  analysis applied to the IR light curves based on the null hypothesis that flux measured from the object is constant with time. Thus we calculate

$$\chi^2 = \sum_i \frac{(F_i - \bar{F})^2}{\sigma_i^2}, \quad (3.1)$$

where for each semester  $i$ ,  $F_i$  is the flux of an object,  $\sigma_i$  is the corresponding uncertainty and  $\bar{F}$  is the mean flux of that object across all imaging epochs. A threshold of  $\chi^2 > 30$  was used for the  $K$ -band and we use  $\chi^2 > 32.08$  for the  $J$ -band. The differing  $\chi^2$  limits give the same p-value for both  $\chi^2$  distributions based on the  $J$  and  $K$ -band light curves, accounting for the different number of imaging epochs and therefore differing degrees of freedom. If a galaxy satisfies either or both conditions, it is classed as hosting a variable AGN.

Utilising this method to select significantly variable objects via the  $\chi^2$  analysis, we are able to identify a sample of 705 candidate active galaxies for study (430 from  $K$ -band variability, 471 from  $J$ -band variability, with 196 detected by both). We recover all of the 393  $K$ -band selected AGN found in Elmer et al. 2020, with a modest increase due to the improvements in the data analysis since the publication of that work. From the initial data set of 114,243 galaxies with IR light curves, we would expect a total of 4 false positives based on a  $\chi^2$  distribution with this number of degrees of freedom.

To search for potential supernovae in the sample, tests were carried out according to Section 5 of Elmer et al. 2020. We identified 36 of the 471  $J$ -band variables (7.6 per cent) for which the variability is largely driven by one epoch. Inspection of both the  $J$  and  $K$ -band imaging and comparing epochs revealed no obvious signs of supernovae (e.g., off-nuclear sources). No additional supernova candidates were identified among the new  $K$ -band variables not analysed by Elmer et al. 2020. Removing this small number of galaxies had no influence on any of the key conclusions presented in this work.

## 3.2 Galaxies on the edge of the science image

Visual inspection revealed a suspicious sample of 104 variable objects located very close to the detector edges. These objects were inspected individually within each epoch, and approximately  $\sim 33$  per cent were identified as potentially fake variables. All objects were found to be real galaxies, but in many cases false variability could be attributed to problems with background subtraction at the detector edges. As such, we re-ran all analysis both with and without this sub-sample of galaxies, and found no significant change in the overall reported trends. Therefore, we removed these edge objects entirely from the analysis to ensure robust results. The remaining sample consists of 601 galaxies.

We note that the pattern of false variables occurred only at the outer edges of the UDS imaging. There was no evidence for false positives close to the internal WFCAM chip boundaries in the UDS mosaic.

## 3.3 Measuring real variability: maximum likelihood

For any measurement of an active galaxy light curve, we know that the observed dispersion in flux ( $\sigma_{\text{obs}}$ ) is due to a combination of the intrinsic magnitude variations due to the active galactic nucleus ( $\sigma_Q$ ) and the measurement noise ( $\sigma_{\text{noise}}$ ) such that

$$\sigma_{\text{obs}}^2 = \sigma_Q^2 + \sigma_{\text{noise}}^2. \quad (3.2)$$

Consequently, if we are to measure the properties of the AGN, we have to be able to separate out these two effects.

As such, to calculate the fractional variability amplitude due to AGN emission ( $\sigma_Q$ ), we make use of a maximum likelihood technique. This method, developed in Almaini et al. (2000), allows for an estimate of the noise-subtracted intrinsic fractional variance ( $\sigma_Q$ ) of the AGN, within the observed variability ( $\sigma_{\text{obs}}$ ). We first take any given AGN light curve and generate a likelihood function

$$L(\sigma_Q | x_i, \sigma_i) = \prod_{i=1}^N \frac{\exp[-(x_i - \bar{x})^2 / 2(\sigma_i^2 + \sigma_Q^2)]}{(2\pi)^{1/2}(\sigma_i^2 + \sigma_Q^2)^{1/2}}. \quad (3.3)$$

To generate each point in the likelihood curve, we normalise each galaxy light curve such that the average flux ( $\bar{x}$ ) is unity. We then step through possible values of fractional AGN variability ( $\sigma_Q$ ) using the measurement of the flux in each semester ( $x_i$ ) and its corresponding measurement error ( $\sigma_i$ ). To get the final likelihood measurement, we take the product of the N values that have been calculated where N is the number of flux measurements in a given light curve.

In order to determine the most likely value of  $\sigma_Q$  for each active galaxy, we simply select the value of  $\sigma_Q$  that maximises the likelihood function, as seen in Figure 3.1. Here the  $1\sigma$  errors are calculated by assuming the likelihood curve has a Gaussian shape.

## 3.4 Variability detection limit

The  $\chi^2$  detection method is inevitably sensitive to photometric errors, and thus in fainter galaxies we can only expect to detect variability at higher fractional amplitude. We can attempt to quantify this effect, to estimate our completeness in identifying variable AGN with a range of intrinsic variability amplitudes ( $\sigma_Q$ ), and over a range of apparent magnitudes. To begin, we remove any active galaxies via their IR variability or X-ray emission from the initial sample of 114,243 galaxies and then split the remaining inactive galaxies into bins based on apparent magnitude. Then, to simulate variability in the inactive galaxies, we artificially introduce variability to their light curves assuming a Gaussian distribution of variations. We require this (variable) component to have a mean of zero and a standard deviation equal to the degree of variability we are simulating, and add this distribution to the normalised inactive galaxies light curves. We then re-run the  $\chi^2$  and maximum likelihood analysis on the ‘new’ light curve for each galaxy, which now contains simulated variability. This allows us to determine if it is now classed as hosting a significantly variable object by the  $\chi^2$  analysis and to ascertain the most likely amplitude of simulated variability using the maximum likelihood technique. This procedure is repeated for a range of variability amplitudes and for each apparent magnitude bin. The results are then used to determine, for a given apparent magnitude, the minimum fractional variability amplitude required for an AGN to be consistently detectable. This also allows us to compare the known simulated variability amplitude

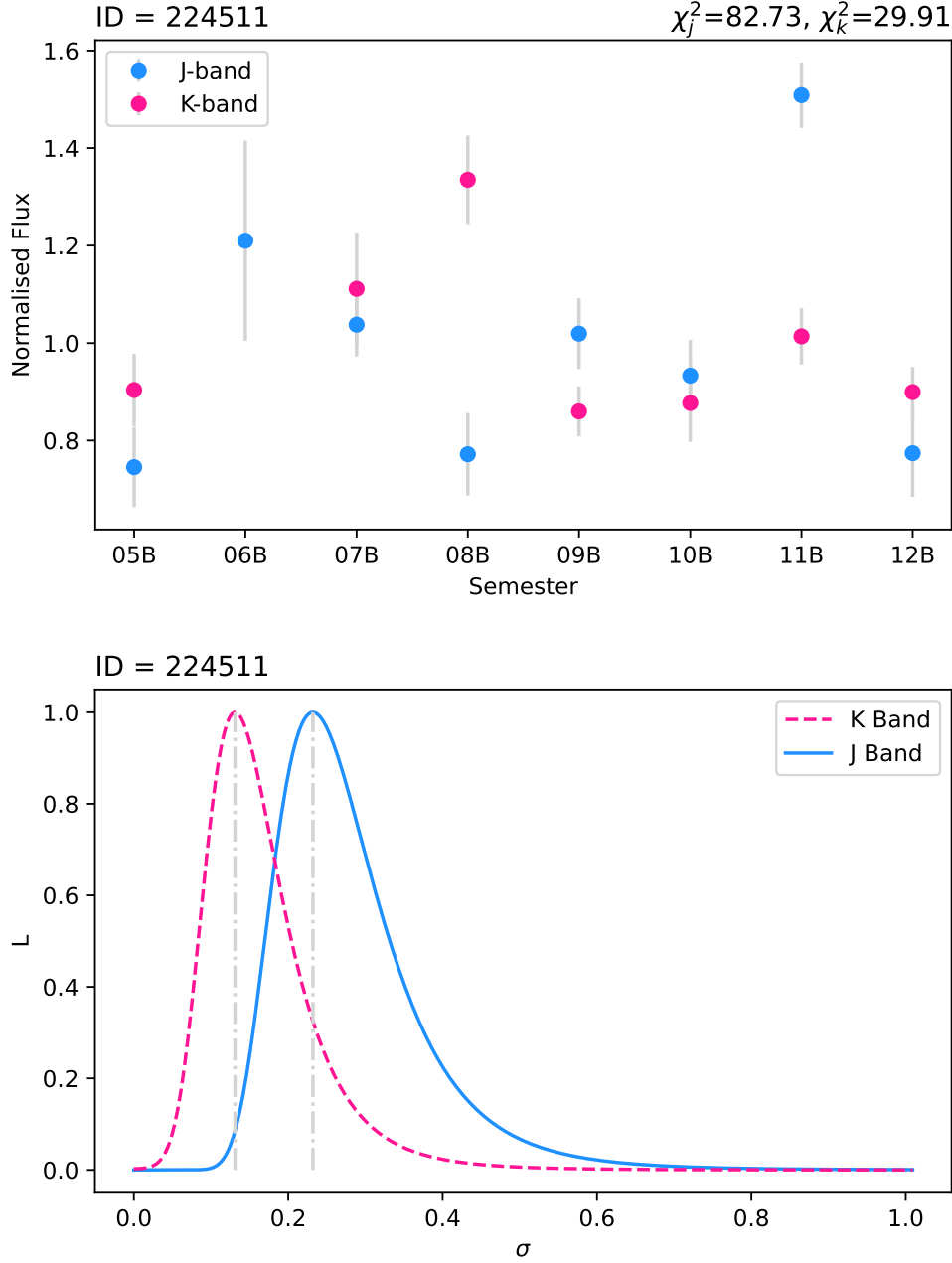


Figure 3.1: Example light curves for a variable galaxy candidate in both the  $J$  and  $K$ -band (top panel) and the corresponding normalised likelihood curves (bottom panel). The threshold for recovery of AGN variability from a given light curve is  $\chi_K^2 > 30$  and  $\chi_J^2 > 32.08$ . As shown by the grey lines in the bottom panel, the variability amplitude is determined by selecting the corresponding value for  $\sigma_Q$  that maximises the likelihood function. This galaxy is only classified as formally variable in the  $J$ -band (blue), as shown by the value of the  $\chi^2$ .

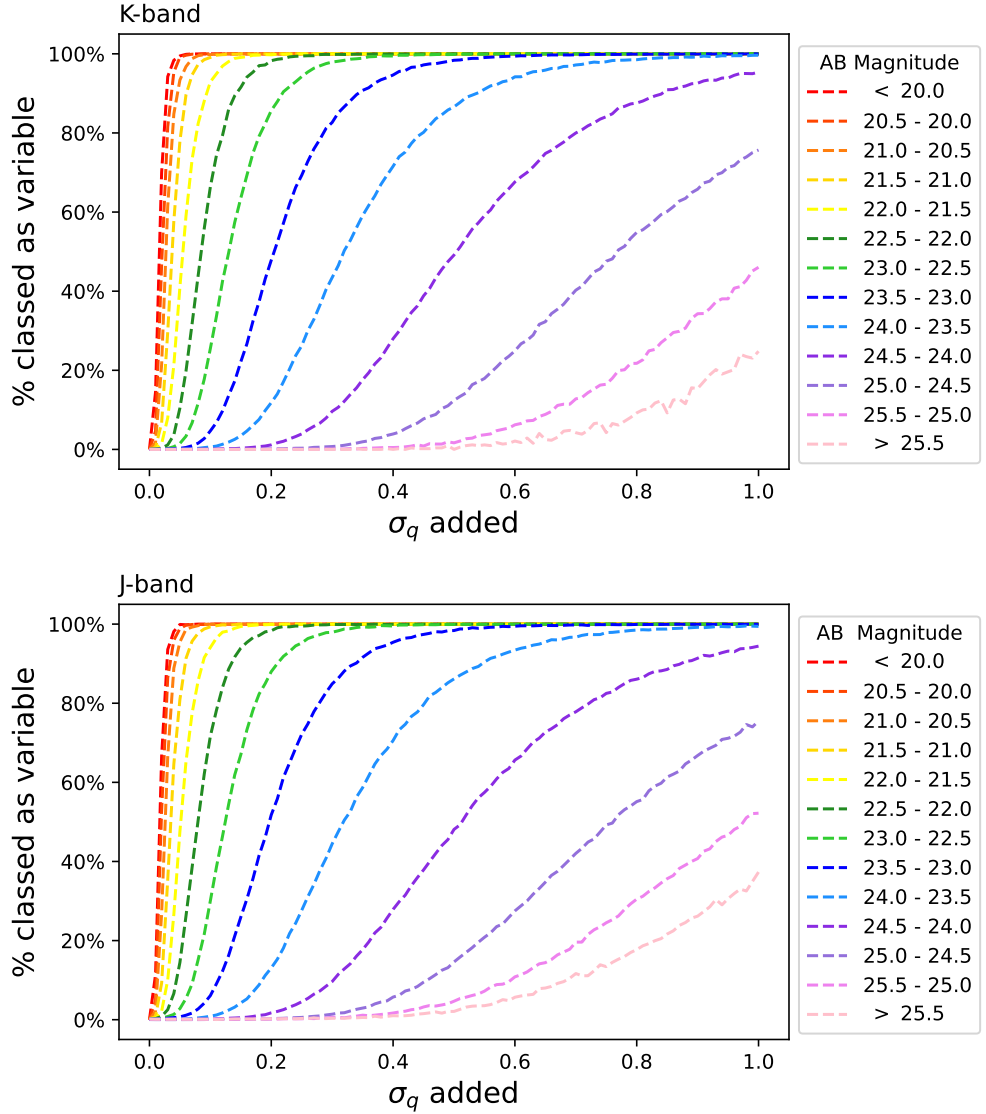


Figure 3.2: The fraction of galaxies classed as hosting variable AGN compared to the level of artificial variability added to the inactive galaxy light curves. Results are shown for the *K*-band (top panel) and *J*-band (bottom panel). Each dashed line represents a different apparent magnitude bin. In the brightest bins, lower uncertainties on measurements allow for low amplitudes of variability to be recovered. However, larger variability amplitudes are required for AGN to be detected in the faintest galaxies.

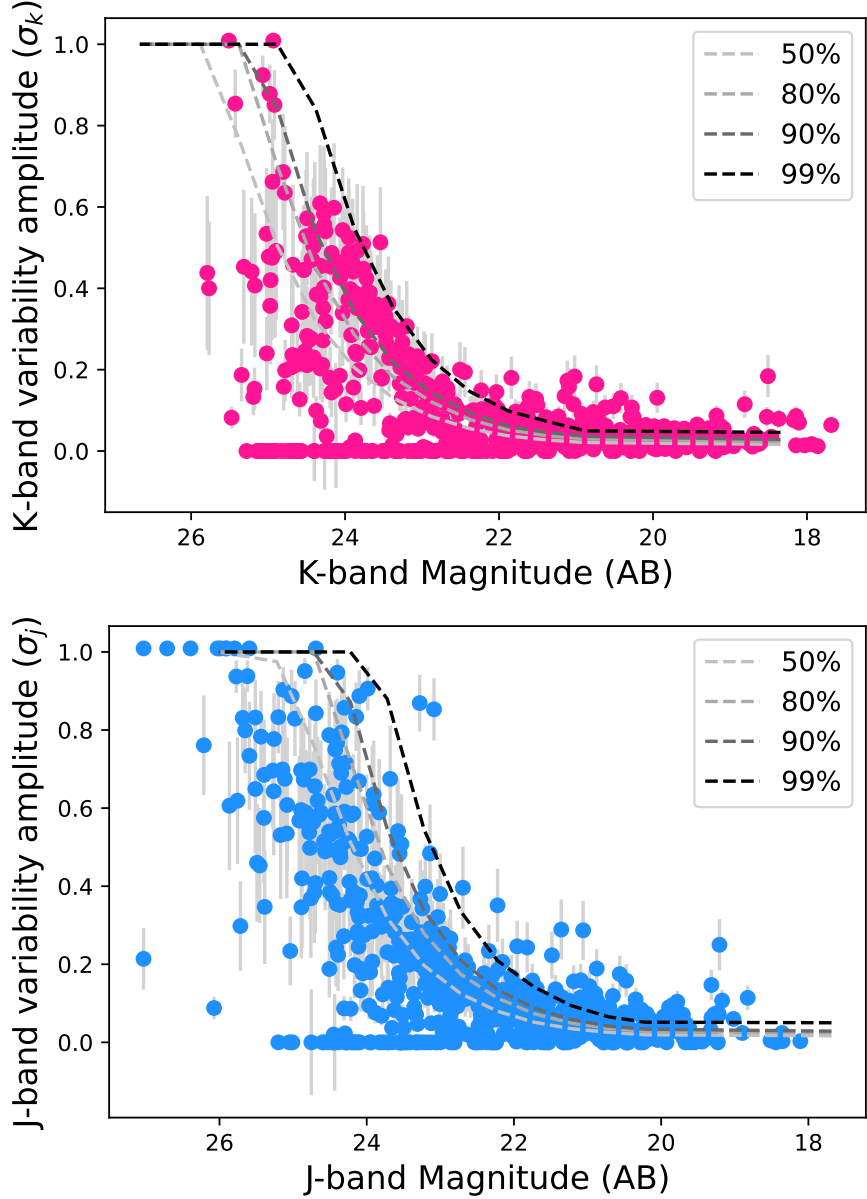


Figure 3.3: AB magnitude vs. variability amplitude for the *real* variable active galaxies. Pink points indicate galaxies selected as hosting variable AGN in the  $K$ -band (top panel), while blue points show the same data but for the  $J$ -band (bottom panel). Grey  $1\sigma$  errors are based on assuming a Gaussian fit to the likelihood curves. Overlaid are detection limit curves for different levels of completeness. We use the 90 per cent curve as this threshold provides a high level of completeness without over-reducing the sample size.

to the amplitude recovered via the maximum likelihood method.

We find that the maximum likelihood technique accurately recovers the amplitude of input AGN variability. Sampling galaxies from each magnitude bin, the average difference in variability amplitude is consistently of the order of 1 per cent. Using these simulations, we are also able to calculate the fraction of galaxies classed as hosting an AGN for every value of simulated  $\sigma_Q$  in each magnitude bin (see Figure 3.2). This provides a suitable estimate for the completeness of our NIR variables, as a function of both apparent magnitude and variability amplitude.

As seen in Figure 3.3, for a given value of an AGN’s fractional variability amplitude and a selected completeness level, we can determine the apparent magnitude required for that selected variability amplitude to be consistently detected to the desired completeness. Throughout this work, we adopt the 90 per cent completeness threshold for a variability amplitude of 20 per cent or higher. From the  $J$ -band curve in Figure 3.3, we find this requires our galaxies to have apparent magnitudes of  $m_J \leq 22.66$ . In the  $K$ -band, the same limit requires an apparent magnitude of  $m_K \leq 23.25$ . We use the  $J$ -band limit in this work as it is stricter, and removes all galaxies excluded by the  $K$ -band limit.

## 3.5 Modified monthly variability amplitude

We can also probe variability on different timescales, and this allows us to determine possible NIR emission mechanisms as well as gain insight into the NIR power spectrum of the variability in the active galaxies. To do this, we calculate a modified monthly variability amplitude measurement in addition to the semester timescale measurements of fractional variability amplitude.

To begin, we use the infrared light-curves built in [Elmer et al. 2021](#), where flux measurements were taken between September 2005 and November 2012 on month timescales. We remove light curves with negative values from the sample and then group the flux measurements based on the date they were taken, with flux measurements being required to be within 120 days of each other to be grouped together. Each group is then normalised such that the average flux is unity. Finally, the maximum likelihood measurement as described in Section 3.3 is applied to the modified light curve to calculate what we refer to as the modified fractional variability amplitude on month timescales.

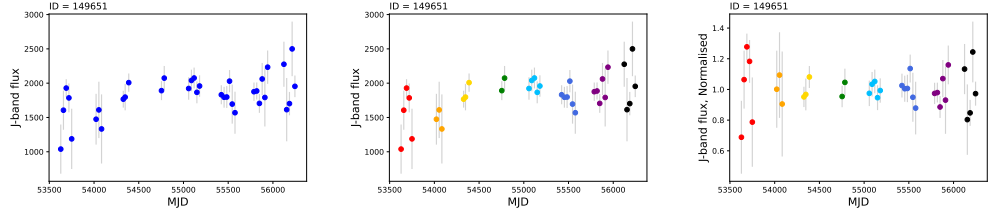


Figure 3.4: Example of the month light curve modification process in the  $J$ -band. In all plots, circular points denote flux measurements and grey lines are errorbars. Left is the measured light curve comprised of flux measurements on month timescales, centre is the group selection, where measurements within 120 day of each other are grouped together and right is the final modified light curve, where each group is normalised such that the mean is unity. The process for  $K$ -band modification is identical, with  $K$ -band data being used in place of  $J$ -band measurements.

An example of this process can be seen in Figure 3.4 and shows how the overall trends on year timescales are removed whilst preserving any month-scale variability that may occur within an AGN system. We also note that whilst we refer to the value measured in this process as a modified month-scale variability amplitude, it is only the month-scale light curves used that are changed, with the procedure by which the variability is measured (i.e. the maximum likelihood technique) remaining unaltered.

# **Chapter 4**

## **Long-term near-infrared variability**

In this work we compare the properties of the 601 NIR variability selected active galaxies in Chapter 3 to a sample of 710 X-ray detected active galaxies from the X-UDS (Chapter 2). We then investigate if and how the properties of active galaxies differ depending on the detection method. This work was published in Paper I.

## 4.1 Introduction

Variability has been shown to be a useful tool in selecting AGN, being able to complement other selection methods by succeeding where they fail. X-ray emission, for example, is commonly thought to have a high probability of selecting the most complete sample of active galaxies (e.g., [Suh et al. 2019](#), [Pouliasis et al. 2019](#)), but this method is intrinsically biased against X-ray-faint objects. In [Trevese et al. \(2008\)](#), a study of low-luminosity AGN found that only 44 per cent of their optical-variability-selected active galaxies have associated X-ray emission. [Pouliasis et al. \(2019\)](#) also selected AGN via optical variability and X-ray emission, but additionally employed the use of IR colour selection. They find that 23 per cent of their variable sample have associated X-ray emission, and only 12 per cent of their variable sample satisfies the IR colour selection criteria for the presence of an AGN. More recently, [Lyu et al. \(2022\)](#) used a wide combination of selection techniques, including radio emission, X-ray detection, variability, UV–IR SED analysis, optical spectroscopy, and IR colour selection in an attempt to find a complete sample of active galaxies in the GOODS-S field. They concluded that no single method was able to select a complete sample of galaxies, and the overlap in the AGN found by different techniques was small.

AGN variability is a relatively unexplored property at infrared wavelengths due to the time required to observe it, but one which is believed to provide significant insight into the nature of the outer edges of the AGN system. In principle, this technique may also provide an advantage in identifying heavily-obsured and/or high-redshift AGN, which may be missed by optical/UV selection techniques. Furthermore, deep wide-field imaging can allow us to study thousands of galaxies simultaneously.

Until recently, studies of IR variability either focused on a handful of individual objects ([Cutri et al. 1985](#), [Lira et al. 2011](#), [Lira et al. 2015](#)), observed AGN selected by other means ([Kouzuma & Yamaoka 2012](#), [Sánchez et al. 2017](#), [Son et al. 2022](#)), or studied

light curves that are not well sampled (Edelson & Malkan, 1987) or constructed from observations from multiple different surveys (Neugebauer et al., 1989). However, Elmer et al. (2020) were the first to select AGN in large numbers based purely on their NIR variability using a single deep data set, and it is this sample we build upon in this work.

In this paper, we investigate the properties of active galaxies selected using NIR variability. We use  $J$ -band light curves to select significantly variable AGN in addition to the  $K$ -band light curves and method described in Elmer et al. 2020. We then compare the properties of these galaxies to a sample of AGN selected via X-ray selection, to determine if and how the properties of active galaxies differ depending on the detection method. We make use of nearly a decade of IR observations provided by the Ultra Deep Survey (UDS; Almaini et al., in prep); the deepest component of the UKIRT (United Kingdom Infra-red Telescope) Infrared Deep Sky Survey (UKIDSS; Lawrence et al., 2007). We use this data to select 601 active galaxies between  $0 < z \leq 5$  based purely on their IR variability using the technique developed, as well as the data constructed, in Elmer et al. (2020). We then compare the properties of these active galaxies to those found using X-ray emission from the X-UDS survey (Kocevski et al., 2018), as well as a control sample of inactive galaxies.

## 4.2 X-ray faint active galaxy populations

We applied the AGN variability detection method described in Section 3 to the UDS DR11, and compared the results to the full-band (0.5–10 keV) *Chandra* X-UDS catalogue described in Section 2.2. If we limit the UDS and the X-UDS to the same survey area (see Figure 2.1, for reference), the samples are largely separate. Of the 601 variability detected active galaxies, 292 lie within the *Chandra* imaging region. The percentage of these that are dual-detected AGN (i.e. X-ray detected and variable in the NIR) is only  $\sim$ 37 per cent (107 / 292). This represents  $\sim$ 15 per cent of the X-ray detected sample (107 / 710).

One possible explanation for this result is that NIR-variable AGN have X-ray emission that is too faint to be detected at the depth of the X-UDS survey. X-ray emission from AGN has long been known to correlate with optical/UV emission (e.g., Tananbaum et al. 1979, Avni & Tananbaum 1986). Therefore, to address this issue, we compare

the observed X-ray-to-optical luminosity ratios to determine if the variability-detected AGN are unusually X-ray quiet (for galaxies that reside within the X-UDS survey region). In Figure 4.1, we compare the monochromatic luminosities at 2 keV and 2500 Å, compared with the expected ratios assuming point-to-point spectral slopes with  $\alpha_{ox} = 1$  and  $\alpha_{ox} = 2$ , corresponding to the typical range observed for quasars (e.g., Steffen et al. 2006).

We note, however, that in our work we make no corrections for host galaxy contributions, dust reddening, or X-ray absorption. We are comparing the observed X-ray to optical ratios, to determine if the objects selected by variability show similar ratios to those selected with deep Chandra observations.

Here, monochromatic luminosities at 2500 Å are derived from the observed optical/UV SEDs, given the source redshift, interpolating the flux between the nearest observed wavebands. The monochromatic X-ray luminosities are determined from the 0.5-10 keV X-ray flux, assuming an X-ray photon index  $\Gamma = 1.9$  for all sources, as used in Elmer et al. (2020). X-ray upper limits from Kocevski et al. (2018) are used for X-ray non-detections. Overall we find that many variable active galaxies have similar optical luminosities to X-ray bright active galaxies, but the majority have only upper limits in our X-ray imaging. Based on the data available to us, the variable AGN appear systematically fainter in the X-rays.

One possible explanation is that the variable AGN are more obscured in the X-ray waveband, but deeper X-ray data will be needed to test that hypothesis. Overall, the implication is that near-infrared variability appears to detect a set of active galaxies that are largely missed by X-ray surveys at these depths.

## 4.3 Active Galaxy Properties

### 4.3.1 Stellar mass distributions and quasar contamination

In addition to there being limited overlap in AGN selected using NIR variability and X-ray detection, we find a difference in the stellar mass ranges of active galaxies selected via X-ray detection and NIR variability. Examining the mass distribution with redshift

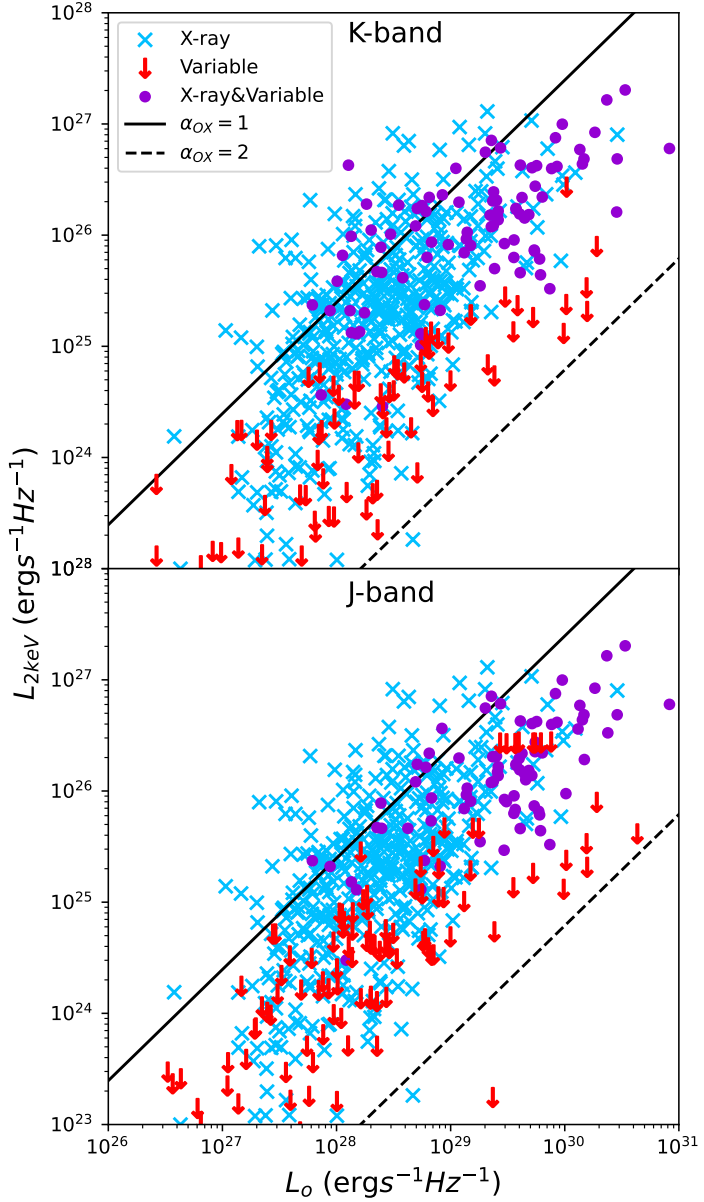


Figure 4.1: Monochromatic 2 keV X-ray luminosity vs. rest-frame optical luminosity at 2500 Å for objects imaged within the *Chandra* region of the UDS field. X-ray bright active galaxies are denoted by blue crosses and AGN detected by both NIR variability and X-ray emission are highlighted as purple dots. Upper limits are used for variability-detected active galaxies without X-ray detections, and are shown by red arrows. The top plot shows *K*-band detected active galaxies and the bottom plot shows *J*-band detected active galaxies. Black lines indicate the slopes corresponding to a spectral index ( $\alpha_{\text{ox}}$ ) of  $\alpha_{\text{ox}}=1$  (solid) and  $\alpha_{\text{ox}}=2$  (dashed), where  $\alpha_{\text{ox}}$  is the spectral index between the optical and the X-ray.

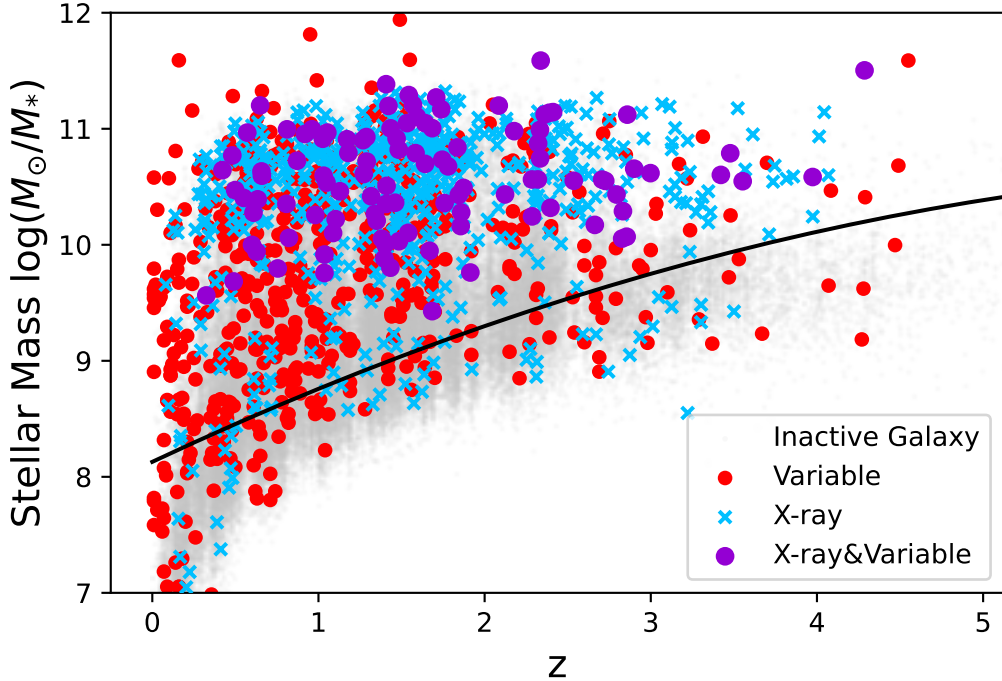


Figure 4.2: Stellar mass vs. redshift distribution for the galaxies in this study. X-ray bright active galaxies are shown as blue crosses, red circles denote variability-detected active galaxies, and purple circles show dual-detected active galaxies. Grey points are inactive galaxies, and the black curve shows the 90 per cent stellar mass completeness limit as a function of redshift.

in Figure 4.2, X-ray emission probes AGN in high-mass galaxies across all redshifts considered, with a majority of X-ray selected active galaxies having stellar masses  $\geq 10^{10} M_{\odot}$ . This is in contrast to the active galaxies selected through variability, which show no obvious bias towards high-mass galaxies.

To illustrate these differences, in Figure 4.3 we plot the distribution of the stellar mass of the active galaxies, separated by detection method.

We find a clear distinction between any X-ray detected AGN, which are much more likely to exist in high-mass galaxies, and NIR variability detected AGN, which show a much more extended mass distribution.

One caveat to these results, however, is the potential for the contamination by non-stellar light, which may bias the stellar masses for the brightest AGN. To investigate this issue, we plot the measured stellar mass against the  $J$ -band absolute magnitude for all galaxies

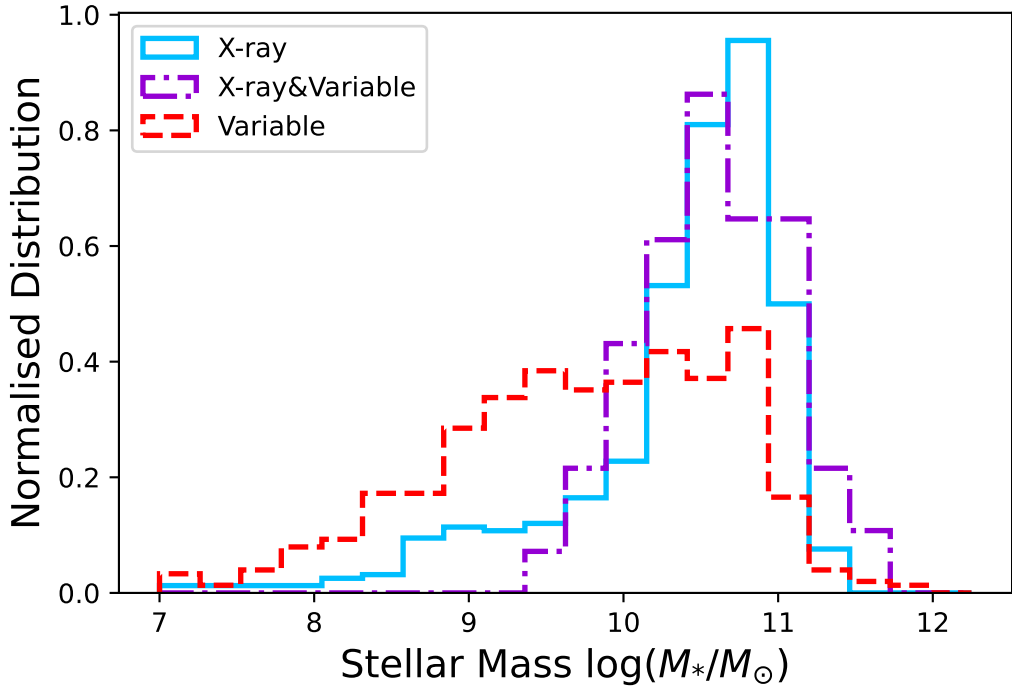


Figure 4.3: Normalised histograms showing the distribution in stellar mass of active galaxies in the sample. Galaxies are separated according to detection method, where the blue solid-lined histogram represents X-ray selected active galaxies, the red-dashed histogram shows objects classified as hosting variable AGN only, and the purple-dotted histogram shows objects that were detected using both methods. A Kolmogorov-Smirnov test confirms that the variability detected sample has a significantly different distribution in stellar masses compared to the X-ray population, rejecting the null hypothesis that they are drawn from the same underlying mass distribution with a significance of > 99.99 per cent.

in the field in Figure 4.4.

Here we find the active galaxies to broadly exist in two regimes: one where the measured magnitude of the galaxy is much brighter than inactive galaxies of a similar mass, and one where the measured magnitude of the galaxy is similar to inactive galaxies of a similar mass. From this bimodality, we can assume that the observed light from the active galaxies that lie within the locus formed by the inactive galaxies are dominated by the hosts' stellar light, and as such the measured host galaxy parameters are minimally impacted by the presence of an AGN. On the other hand, active galaxies that are much brighter than their inactive counterparts of similar mass likely have emission that is dominated by the AGN, suggesting the presence of a quasar.

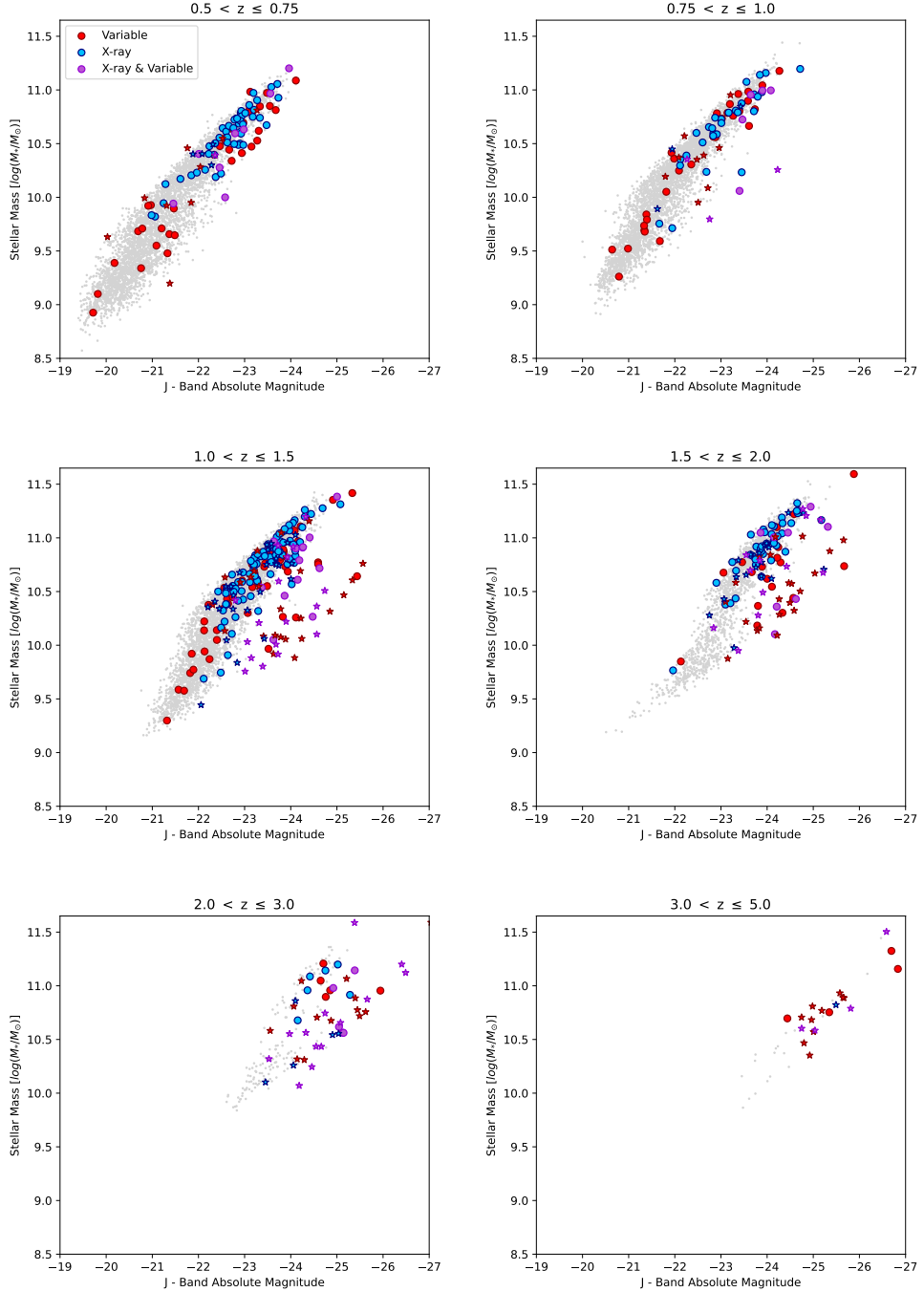


Figure 4.4: Stellar mass vs.  $J$ -band absolute magnitude for X-ray detected active galaxies (blue points), variability-detected active galaxies (red points) and dual-detected active galaxies (purple points) as a function of redshift. Inactive galaxies are plotted as grey points and all galaxies lie above the 90 per cent mass completeness limit. Corresponding coloured stars indicate an active galaxy that has a stellarity index of  $\geq 90\%$  according to the CLASS STAR parameter from SExtractor.

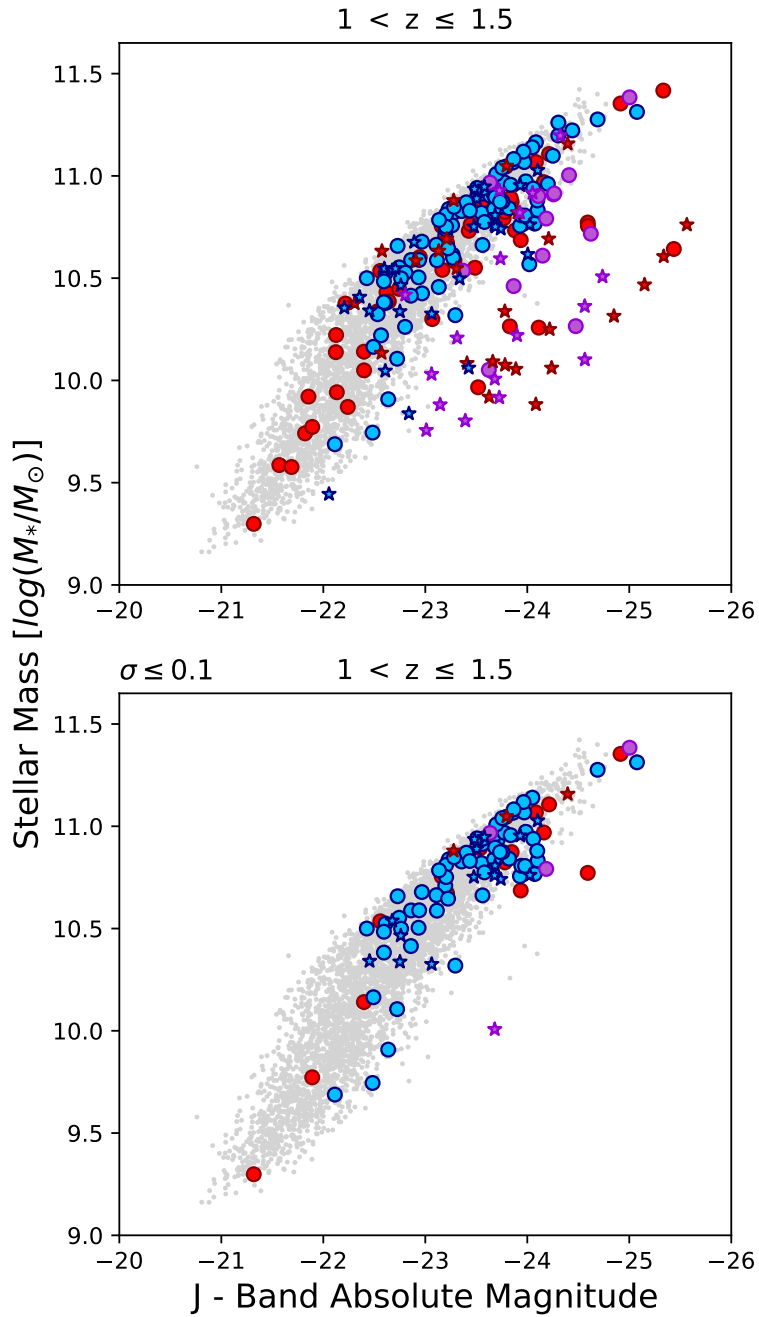


Figure 4.5: Stellar mass vs.  $J$ -band absolute magnitude for galaxies between  $1 < z \leq 1.5$ . Plotted are active galaxies (AGN) that are either X-ray-detected (blue points), variability-detected (red points), or dual-detected (purple points), as well as a comparison sample of inactive galaxies (grey points). Correspondingly-coloured stars indicate an active galaxy that has a stellarity index of  $\geq 90\%$  according to the CLASS STAR parameter from SExtractor. The bottom plot is as the top, but only shows active galaxies with (intrinsic) variability amplitudes of  $\sigma_J \leq 0.1$ . All galaxies plotted lie above the 90% mass completeness limit.

To test if these abnormally bright sources are quasars, we investigate their morphology using the  $K$ -band stellarity index from SExtractor, which (after removing galactic stars) provides a good indication that an AGN is dominating the emission from a source. From this we find that a majority of the bright sources appear point-like, which suggests the AGN emission is outshining that of the host galaxy.

These empirical trends are likely to be caused by a combination of factors. In particular, the stellar masses are obtained by fitting stellar population models, without an AGN component. If a Type-1 quasar dominates the SED, the best fit is likely to be an extremely young stellar population, yielding a very low mass-to-light ratio. As a secondary issue, the variable AGN were identified in the observed  $J$  and  $K$  bands, while observations at longer and shorter wavelengths were taken at different epochs. Therefore, as a selection effect, we might expect AGN to be brighter than average in the  $J$  and  $K$  bands, which would enhance their near-infrared luminosity relative to the stellar mass determined from the 12-band SED.

Furthermore, to investigate if a quasar is present within the identified bright, point-like sources, in Figure 4.5 we remove the objects with the largest variability amplitudes, on the assumption that the NIR light in such objects must be dominated by the AGN. Figure 4.5 shows the stellar mass vs. magnitude for galaxies with redshift  $1 < z \leq 1.5$  both before and after requiring galaxies to have an intrinsic variability amplitude of  $\sigma_Q \leq 0.1$ . Here we find that applying this limit primarily removes the point-like sources that are much brighter than inactive galaxies of a similar mass. In the case of objects detected via their X-ray emission, imposing this limit does not have a significant effect on the active galaxies that lie within the locus formed by inactive galaxies, but largely removes the bright, point like sources. It is therefore likely that the bright point-like active galaxies are indeed quasars, where the powerful AGN is driving significant variability and dominating the NIR light.

### 4.3.2 Stellar mass functions

To fairly compare the host properties of the active galaxies, we remove the quasars from the distributions to avoid significant amounts of non-stellar light impacting measurements. To do this we generate a contour that encompasses 95% of the inactive galaxies in each bin seen in Figure 4.4, and we require the active galaxies in corresponding bins

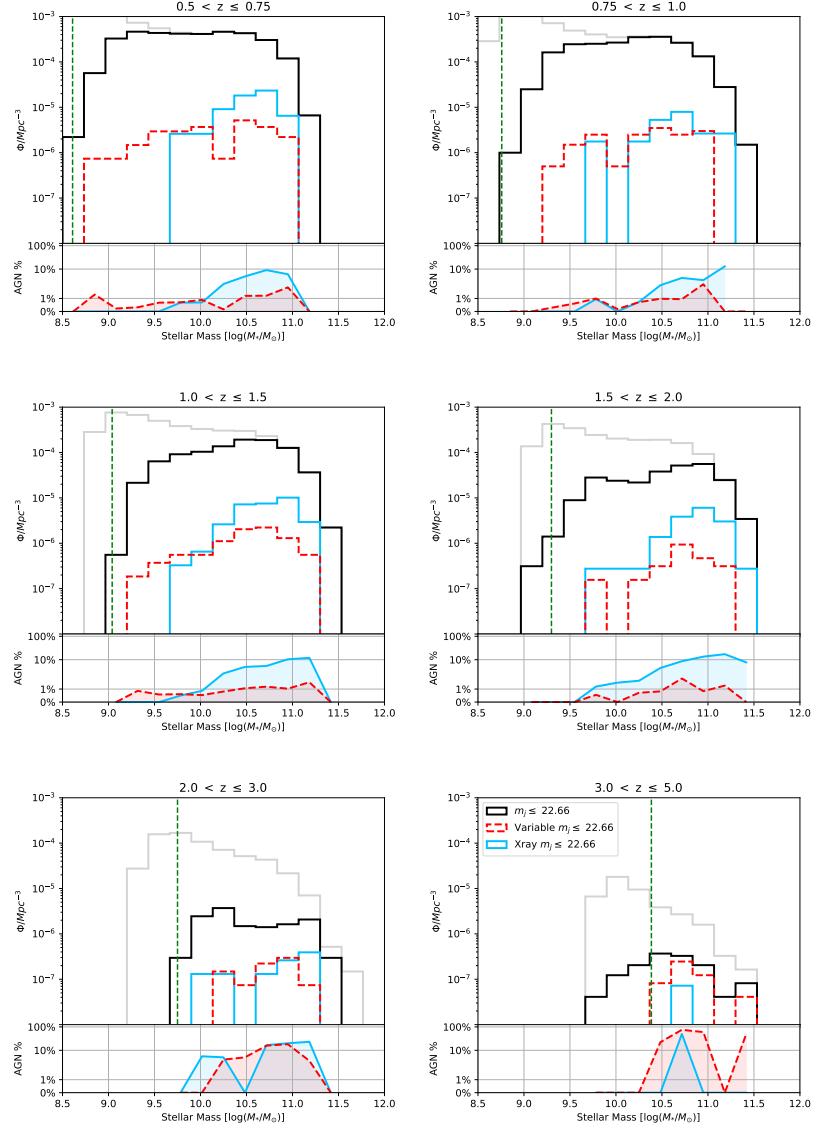


Figure 4.6: Stellar mass functions as a function of redshift. The grey histogram represents the mass distribution for all galaxies within the field except for quasar-like AGN, which have been removed. The black histogram shows the same but for galaxies with  $J$ -band apparent magnitudes  $m_J \leq 22.66$  which ensures that a variability of 20% or higher will be consistently detectable. The dashed red histogram is as the black but shows only variability detected active galaxies. The solid blue histogram shows X-ray detected active galaxies, again with candidate quasars removed. X-ray detections were calculated using galaxies from the X-UDS imaging region and scaled to match the variability detected galaxies. The corresponding coloured distributions below each stellar mass function shows the percentage of AGN for that redshift bin as a function of stellar mass. The 90% mass completeness limit is denoted by the vertical dashed green line.

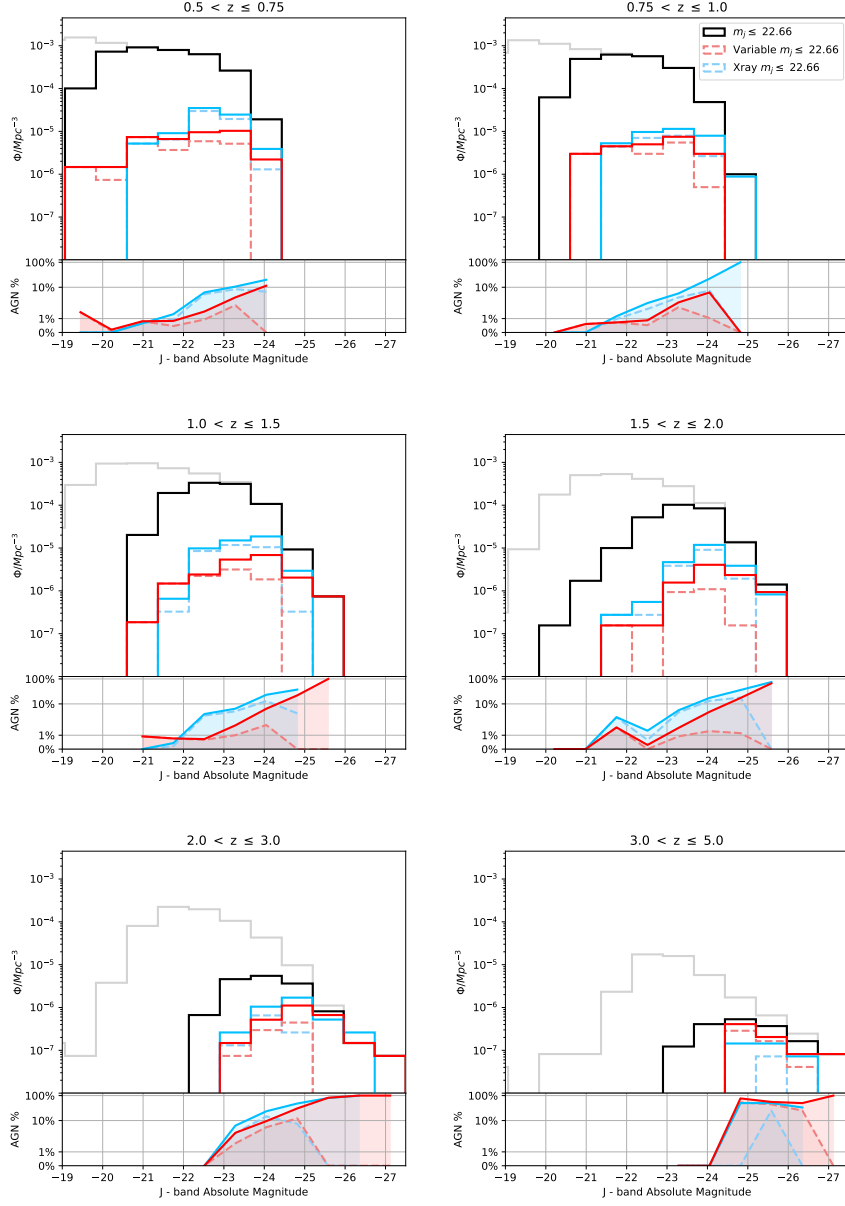


Figure 4.7: Luminosity functions as a function of redshift. The grey histogram represents the luminosity distribution for all galaxies within the field, while the black histogram shows the same but for galaxies with  $J$ -band apparent magnitudes  $m_J \leq 22.66$ . The solid red and blue histograms are as the black but only shows variability and X-ray detected active galaxies, respectively. Lighter coloured, dashed histograms show the active galaxy luminosity functions with quasars removed. X-ray detections were calculated using galaxies from the X-UDS imaging region and scaled to match the variability detected galaxies. The corresponding coloured distributions below each luminosity function shows the percentage of AGN for that redshift bin as a function of decreasing  $J$ -band absolute magnitude.

to lie within the contour formed by the inactive galaxies. Applying this cut to the data removes 75 (12%) of the variable AGN from the sample, 35 (5%) of the X-ray AGN and 55 (51%) of the dual-detected AGN. Using the remaining galaxies, we generate the stellar mass functions shown in Figure 4.6. Here the grey line shows the mass function for all galaxies in the data and the solid black line shows the population of galaxies with  $m_J \leq 22.66$ . As discussed in Section 3.4, this magnitude limit ensures that a variability of 20% or higher will be consistently detectable for all galaxies.

With the quasars removed, we find that the fraction of galaxies with X-ray detected AGN increases with increasing stellar mass of the host galaxy, whereas the detection rate of NIR variable AGN is largely flat, remaining on the order of  $\sim 1\%$  of galaxies regardless of the stellar mass of the host. This difference is consistent up to  $z \approx 2$ , where enough galaxies above the mass completeness limit are present to draw reasonable conclusions. We conclude that, across a broad redshift range, NIR variability allows for the identification of AGN in much lower mass host galaxies compared to X-ray selection.

### 4.3.3 Luminosity functions

In this section we investigate the luminosity functions of objects derived from the two methods of AGN detection, without applying any quasar filtering. This will provide a check on the influence of AGN light on the derived properties of these objects, which will be particularly significant in future situations where we may lack the range of spectral data and spatial resolution required to filter out quasars. In Figure 4.7, we plot the  $J$ -band absolute magnitude as a function of redshift for the detected active galaxies.

Here, we find that both methods detect much more similar distributions of objects, with the fraction of AGN increasing with luminosity whichever technique is used. This increase reflects the fact that the luminosity functions are strongly influenced by the contribution of AGN light, with brighter AGN more likely to be detected by either method. Without the auxiliary information we have employed in this work, it is not possible to reliably disentangle host galaxy and AGN properties from such data.

## 4.4 Conclusions

In this study, we use the long-term near-infrared variability of objects seen in the UKIDSS Ultra Deep Survey as an alternative approach to finding active galactic nuclei. We then compare the sample of AGN revealed in this way to those found using a more conventional X-ray-based method in the same field.

We find that the variability approach detects a distinct population of AGN, with an overlap of only 37 per cent between the two samples. An analysis of the X-ray-to-optical luminosity ratio finds the IR-variable AGN appear relatively X-ray quiet. Whether these AGN are intrinsically X-ray faint or heavily obscured is unclear, and will be the subject of future study.

After excluding quasar-like objects, whose AGN brightness means that we cannot reliably measure properties of the underlying host galaxy, we find that IR variability systematically detects AGN in galaxies with lower stellar masses than X-ray-detected objects. Comparing their mass functions, we find that IR-variable AGN are hosted in  $\sim 1\%$  of galaxies of any mass, whereas the percentage of X-ray AGN detected strongly increases with increasing stellar mass of the host galaxy. This distinction seems to be independent of redshift out to the  $z \sim 2$  probed by these data. One plausible explanation for the difference would be related to extinction: if low-mass hosts tend to systematically contain more heavily obscured nuclei, that might explain why AGN in such galaxies are more readily detected by their infrared variability than by their extincted X-ray emission. In future work we will explore the dependence of variability on redshift and hence on rest-frame waveband, to explore the implications for the origin of the AGN emission.

In seeking such physical explanations, we need to be able to reliably separate AGN and host properties. The significance of the contribution of AGN light to distorting our understanding of their host galaxies is underlined by the rather different results we obtain by simply studying their luminosity functions, in which a higher fraction of AGN is found in more luminous objects, whichever method is used to identify them. This distinction arises from the fact that the luminosity function, particularly when including quasar-like objects, reflects the properties of the AGN as well as their hosts. Clearly, some care is needed in interpreting such composite data, and additional spectral and spatial information is vital.

These results indicate that multiple approaches to AGN detection are required to obtain a complete census of such objects. With upcoming deep, wide-field surveys such as EUCLID and LSST, which will be obtained over extended periods, long-term variability offers an important approach to identifying AGN missed by other methods, which is key to a more detailed understanding of the prevalence of these objects and their role in galaxy evolution.

# **Chapter 5**

## **Investigating the origin of infrared variability in AGN**

## 5.1 Introduction

Infrared (IR) emission has been observed in active galaxies since the late 60's ([Pacholczyk & Wisniewski 1967](#); [Low & Kleinmann 1968](#)), and these detections sparked interest into the how the radiation is generated in this regime. As discussed in Section 1.4, there is a paucity of research into the IR variability properties of active galaxies compared to shorter wavelengths, and this is most likely due to the time required for IR variability occur, however observations in these wavelengths has the potential to reveal much information about the system. Before conclusions can be drawn from IR variability studies however, one must ascertain how IR emission is produced, as the production method implies different underlying physical structures within the AGN system.

The two main contenders for generating infrared radiation are thermal and non-thermal emission processes. Thermal radiation arises when the emitting particles do so because of the energy they have gained through their temperature, whereas the energy produced in non-thermal emission has no dependence on the temperature of the particles. Since non-thermal emission does not require the heating of a body, in theory a singular production mechanism could generate the broadband radiation seen in active galaxies, leading to a simpler view of the AGN structure.

Given that infrared emission has been detected in active galaxies, research has found evidence that it is produced non-thermally. [Elvis et al. 1986](#), for example, was able to fit a single power law to the X-ray to infrared spectral energy distribution (SED) of the quasars studied in their sample. From this, they argued that an AGN is comprised of a single, nuclear, non-thermal production component for X-rays to IR radiation as it is unlikely that multiple interacting emission mechanisms would fit the same overall power law. Similarly, [Cleary et al. 2007](#) ruled in favour of non-thermal emission processes when fitting both dust (thermal) and synchrotron (non-thermal) models to observed data from radio-loud quasars. They found their fits to be dominated by the non-thermal components and concluded that mid-infrared to radio emission was produced in the jets and lobes of active galaxies. Whilst both of these pieces of research favour non-thermal emission, the AGN structure models they suggest are very different from each other, illustrating the range of possible structures that AGN could have.

In contrast to the non-thermal scenario, other studies have concluded IR radiation arises from thermal processes. One such example can be seen in [Rees et al. 1969](#), who was

able to recreate the observed  $2.2\mu\text{m}$  -  $22\mu\text{m}$  spectra of Seyfert galaxies via a dust-heating model. By simulating dust grains heated by a nuclear source, they found they were able to recreate the observed power-law spectrum as well as predict the variability timescale for the IR based on evaporation temperatures of the dust. [Barvainis 1987](#) completed similar work, developing a circumnuclear dust-heating model for IR AGN radiation. Again this thermal radiation scenario was able to reproduce observed IR spectra of active galaxies, but it was also able to predict the orbital radii for the material. A ring of dusty material is required in both pieces of research for thermal emission to be viable, however an absence of this structure does not impact the non-thermal models.

Outside of simulations, direct observations of the infrared continuum in AGN has also favoured a thermal emission scenario. One of the first reviews on the topic is presented in [Rieke 1978](#), where the IR measurements for 53 Seyfert galaxies is collated from various sources. This review concludes that the IR is made up of re-radiated light from dust in a disk about the central engine. Similarly, [Sanders et al. 1989](#) measured the  $0.3\text{nm}$  to  $6\text{cm}$  continuum of 109 quasars and found similar results, stating that the accretion disk and the broad line region contribute to heating dust and gas in the AGN, resulting in the observed IR radiation. Furthermore, in reporting on the infrared photometry of 20 radio-loud quasars [Shi et al. 2005](#) found a majority of the far-infrared radiation originated from dust heated by the AGN and star formation within the active galaxy, with the AGN being the dominant heating source. [Dicken et al. 2009](#) also studies the far-infrared spectrum of 46 active galaxies. They quote the heating of circumnuclear dust as being the primary emission mechanism for the infrared radiation in the systems, as well as rule out non-thermal synchrotron contamination as a potential source of infrared radiation in active galaxies.

Analysing the spectral data has provided mixed results in determining what drives infrared emission in both thermal and non-thermal scenarios, however other approaches have been used to characterise this radiation. If a single, non-thermal source produces the broadband emission observed in an AGN, then the NIR flux should vary on the same hour-timescale observed in the X-rays. To test this hypothesis,  $2.2\mu\text{m}$  variability was measured in [Hunt et al. 1994](#) for 9 Seyfert galaxies known to be highly variable in the X-rays. Through this research, no short timescale variations typical of non-thermal emission was observed in the IR measurements, resulting in the conclusion that the NIR emission is dominated by slowly varying reprocessed light.

Finally, [Rieke & Lebofsky 1981](#) examined the X-ray, UV, optical and infrared continuum of NGC 4151, one of the six original Seyfert galaxies ([Seyfert, 1943](#)), where they fit multiple components to the spectrum of the galaxy to derive a comprehensive view of the nucleus. The polarisation of the  $1\mu\text{m}$  -  $4\mu\text{m}$  radiation was found to be negligible in this galaxy, which argues strongly against non-thermal emission and they concluded that it was more likely that infrared emission arose from dust heated by a non-thermal source.

Though it is now accepted that AGN emission varies in flux in every band it has been observed in (Section 1.4), very few variability studies have been completed on the origin of infrared emission in active galaxies. Though [Hunt et al. 1994](#) rules in favour of the thermal scenario, the research is limited to a small galaxy sample with light curves that are not well sampled.

Infrared variability is also measured in [Clavel et al. 1989](#), where the far-UV, optical and infrared variability of the active galaxy Fairall 9 is studied. They found that the nature of the variability changed in different wavelengths, with the optical and *J*-band variability seeming to be to be diluted by starlight, but otherwise in phase with UV variability measurements. Variations at longer wavelengths, such as the *K* and *L*-bands however, were noticeably out of phase with measured fluctuations in the bluer bands and this identified a possible turnover in emission mechanisms between the rest-frame *J* and *K* bands in active galaxies.

In this chapter, we investigate the properties of 601 active galactic nuclei between  $0 < z \leq 5$ , selected through long-term near-infrared variability in the *J* and *K*-bands. We compare the rest-frame features of the galaxies to each other as well as to a sample of X-ray selected AGN split by hardness ratio as a proxy for obscuration. From this we determine if AGN that are significantly variable in the *K*-band show features consistent with emission from the thermal re-radiation of bluer light by dust, and we investigate if these same features are present in AGN selected in the *J*-band.

## 5.2 Variability dependence on wavelength

We begin by investigating how the variability amplitude of the active galaxies changes with wavelength. To do this, we plot the variability amplitude in the *J*-band ( $\sigma_J$ ) vs the

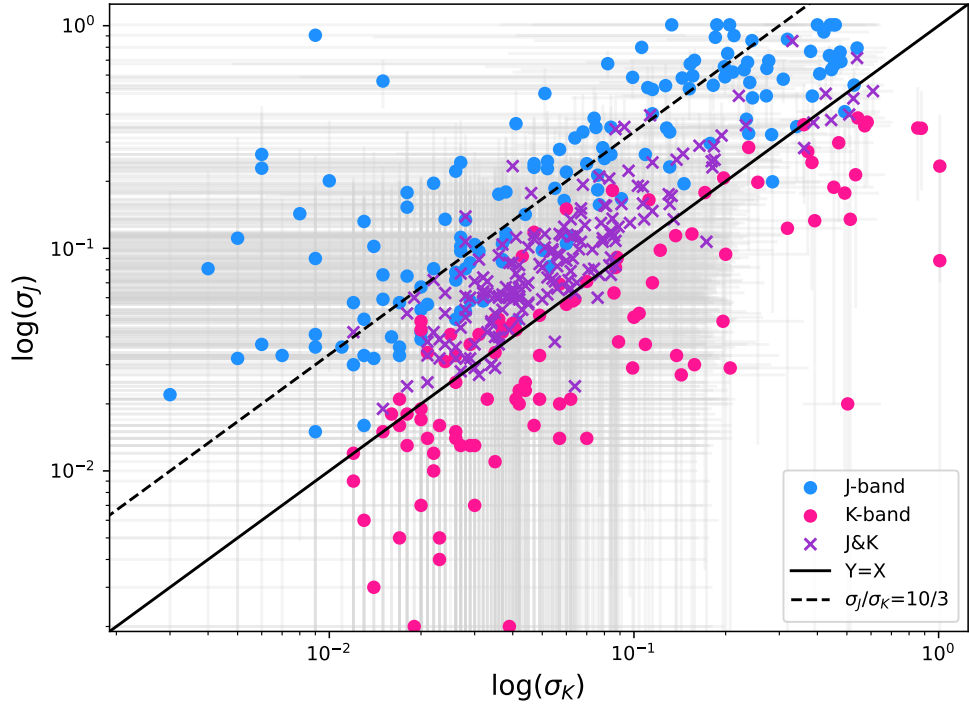


Figure 5.1:  $J$  vs  $K$ -band variability amplitude for variability detected AGN. AGN are split by detection band with blue dots showing AGN variable in the  $J$ -band only, pink dots showing  $K$ -band only variables and purple crosses denoting dual-band detected AGN. The solid black line shows unity and the black dashed line is the expect variability ratio of 10/3 based on the modeled IR variability spectrum in [Meusinger et al. 2011](#).

$K$ -band ( $\sigma_K$ ) in Figure 5.1. Here galaxies are split by the photometric band the AGN were selected as being significantly variable in.

We first find that all the galaxies show a positive correlation in  $\sigma_J$  and  $\sigma_K$ , regardless of the band the AGN was selected in, however clear differences in the chromatic nature of the AGN becomes apparent when splitting the measurements by the detection band. AGN selected in the  $J$ -band show enhanced variability in the bluer,  $J$ -band compared to the  $K$ -band. This anti-correlation of variability amplitude with wavelength is in agreement with previous work in the UV ([Paltani & Courvoisier, 1994](#)) and the optical ([Cid Fernandes et al. 1996](#), [Berk et al. 2004](#), [MacLeod et al. 2010](#), [Zuo et al. 2012](#)). Measurements for  $K$ -band selected AGN contrast this however, with larger fractional variability being measured in the redder  $K$ -band.

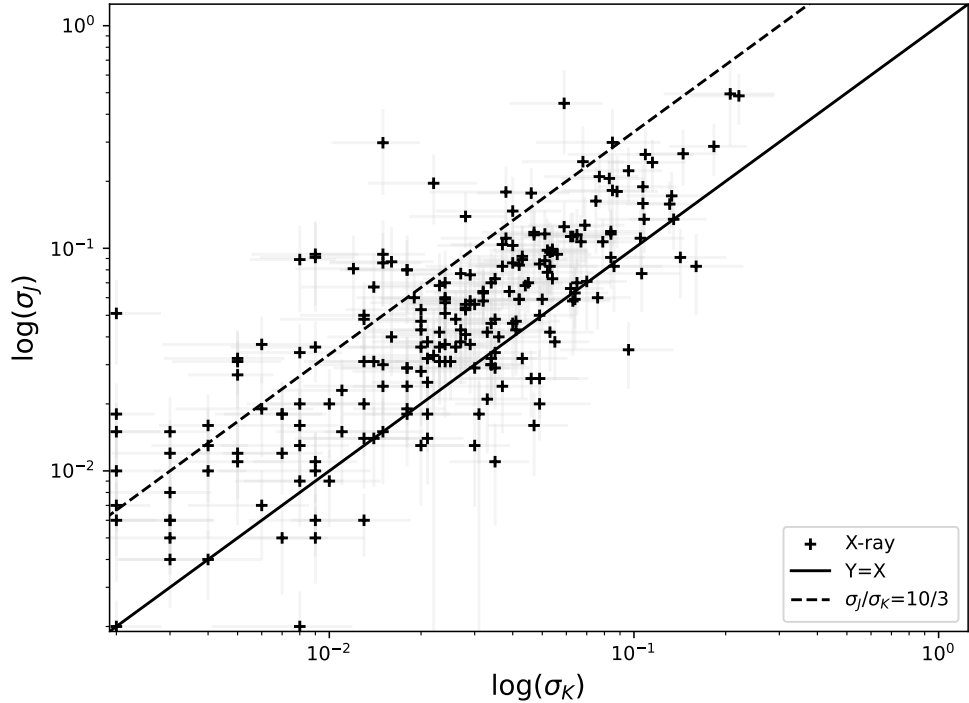


Figure 5.2:  $J$  vs  $K$ -band variability amplitude for all X-ray detected AGN in this sample. The solid black line shows unity and the black dashed line is the expect variability ratio of 10/3 based on the modeled IR variability spectrum in Meusinger et al. 2011.

The result that  $K$  and  $J$ -band selected active galaxies show opposite correlations with wavelength could be due to selection bias, as one would expect the variability amplitude to be larger in the detection band. To determine if this is the case, we inspect the behaviour of the dual-band detected active galaxies (AGN measured as being significantly variable in both the  $J$  and  $K$ -photometric bands), as if the detection band does bias the variability amplitude measurement, we expect the comparison of  $\sigma_J$  to  $\sigma_K$  to be unity in this sample. We also make the same comparison for the X-ray AGN. The detection of these AGN is not dependant on variability, and as such breaks the degeneracy of the amplitude measurement with detection band, allowing for an intrinsic study of the chromatic nature of the AGN variability. Inspecting these measurements in Figures 5.1 and 5.2 finds both of these samples to largely anti-correlate wavelength and variability amplitude, in agreement with the  $J$ -band variable AGN in this sample.

### 5.2.1 Infrared variability spectrum

In [Meusinger et al. 2011](#), the AGN variability spectrum is calculated to change as

$$\sigma_\lambda \propto \lambda^{-2}. \quad (5.1)$$

Here  $\lambda$  is the wavelength and  $\sigma$  is the variability amplitude measured at wavelength  $\lambda$ . Applying this relation, we find the expected  $J$  to  $K$  amplitude ratio to be  $\sigma_J/\sigma_K \approx 10/3$ . This value is plotted in Figures 5.1 and 5.2, and predicts that a given, unobscured AGN should be more variable in the  $J$ -band than the  $K$ -band.

Inspecting where the values measured in this study lie in comparison to the simulated value finds differences when splitting the variability detected AGN by detection band, with it appearing that the more significant the  $K$ -band variability is, the further the  $\sigma_J/\sigma_K$  ratio lies from the model expectation. The  $J$ -band detected AGN largely lies along the 10/3 line, whereas the AGN only variable in the  $K$ -band have a much lower ratio and dual-band detected AGN fall largely in the middle of these two groups. The X-ray AGN show a larger spread in their amplitude ratio measurements, however the bulk of the distribution follows the dual-band detected AGN, lying between the simulated values and unity.

These results show that AGN variable in the  $J$ -band only are clearly different from AGN variable in the  $K$ -band only. The properties of the X-ray and dual-band selected samples confirm that these differences cannot be explained by selection bias in the AGN and as such, it is more likely that the positive correlation of  $\sigma_K$  and wavelength for  $K$ -band detected AGN is due to some physical processes in the system.

## 5.3 Origin of Variability in AGN

After determining that splitting the variable AGN by detection band gives opposite correlations of wavelength and variability amplitude (Section 5.2), we next aim to determine if the underlying origin of the variability is different for a given detection band. To do this, we examine the rest-frame (RF) emission of the 601 variability detected active galaxies by plot the ratio of the measured  $K$  to  $J$ -band variability amplitude vs

redshift in Figure 5.3. Once again, samples are split by the photometric band they are variable in.

As found in Section 5.2, AGN that are variable in the  $J$ -band only best follow the simulated variability expected in AGN (Meusinger et al., 2011), showing little evolution with redshift and largely lying along the predicted ratio of  $\sigma_K/\sigma_J \sim 0.3$ . Additionally, dual band detected AGN have a similar flat distribution with redshift, but are consistently offset from the model value, with larger values of  $\sigma_K/\sigma_J$  for all epochs studied. In Figure 5.4 we reproduce Figure 5.3 and overlay the X-ray AGN. Inspecting this we find the bulk of the X-ray population to follow a similar distribution as the dual-band detected AGN, with values that are positively offset from the model, however we note they do show a spread in  $\sigma_K/\sigma_J$  overall, with both large and low values over cosmic time. The AGN variable in the  $K$ -band have the most unique behaviour of the active galaxies considered in this study. They show the highest  $\sigma_K/\sigma_J$  of any group as well as a clear decrease in the ratio with increasing redshift. In addition to this, most  $K$ -band only detections are found at RF-IR redshifts where  $J$  and dual-band detections show no obvious preference for the rest-frame of the emission.

To explain the differences observed, we suggest a mix of effects. We first see that  $K$ -band detected AGN have a lower value of  $\sigma_J$  than what may be expected, and this could be due to a larger host galaxy contribution to the measured light in the  $K$ -band detected active galaxies. As we measure fractional variability in this work, larger host galaxy emission relative to the AGN would lead to a lower value of  $\sigma_J$  for the same intrinsic AGN variability. This would also contribute to the decrease in the ratio over cosmic time, as AGN at higher redshifts are more luminous by definition, leading to higher AGN-to-host flux ratios and an overall increase in  $\sigma_J$  for the  $K$ -band selected AGN. Further to this, the presence of dust in the  $K$ -band AGN systems where there is less or none in the dual and  $J$ -band detected active galaxies is a plausible cause for the shape and location of the galaxies on the  $\sigma_K/\sigma_J - z$  plane, as well as the positive correlation of variability amplitude and wavelength, measured in the  $K$ -band detected sample. Variations in dust obscured AGN would first be reddened, and then redshifted to wavelengths beyond the  $K$ -band for all but local galaxies. Moreover, the few  $K$ -band detections at RF-optical redshifts having  $\sigma_K/\sigma_J$  ratios closer to the model value is evidence in favour of a dust-reprocessing scenario with host galaxy emission becoming more prominent at lower redshifts. These observations would be expected if such objects were truly unobscured compared to their RF infrared counterparts, with less or no dust being available for the

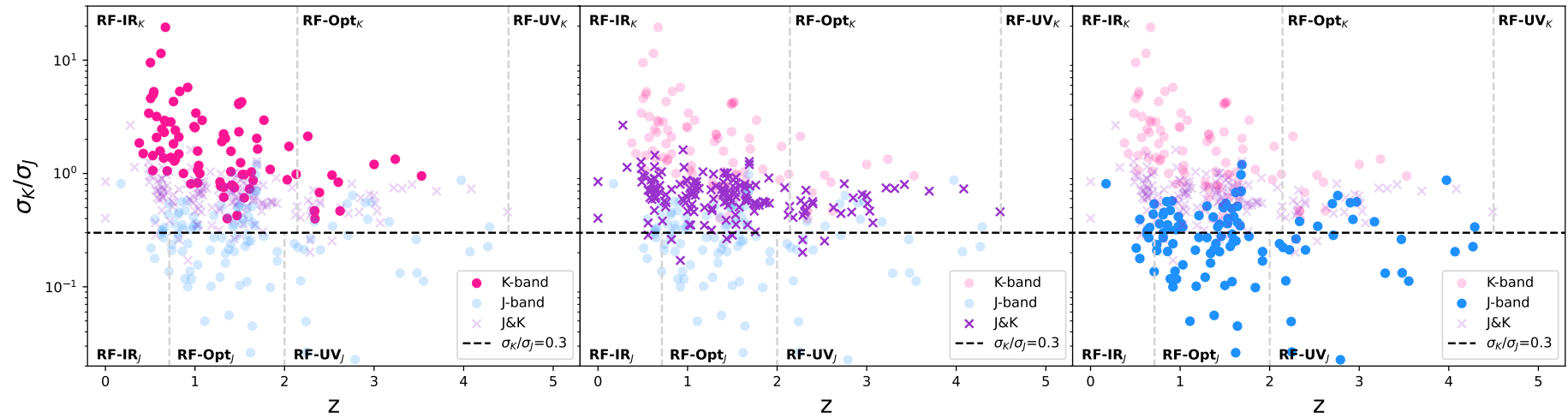


Figure 5.3: Ratio of  $K$  to  $J$ -band variability amplitude vs redshift for variability detected active galaxies. Pink dots show  $K$ -band only detect active galaxies, purple crosses show dual band detected active galaxies and blue dots show  $J$ -band only detected active galaxies. Horizontal dashed grey line shows the model variability ratio of 0.3 as calculated according to the variability spectrum in Meusinger et al. 2011. Vertical dashed light-grey lines denote the rest-frame emission ranges for the  $K$  and  $J$ -band above and below the  $Y=0.3$  line respectively.

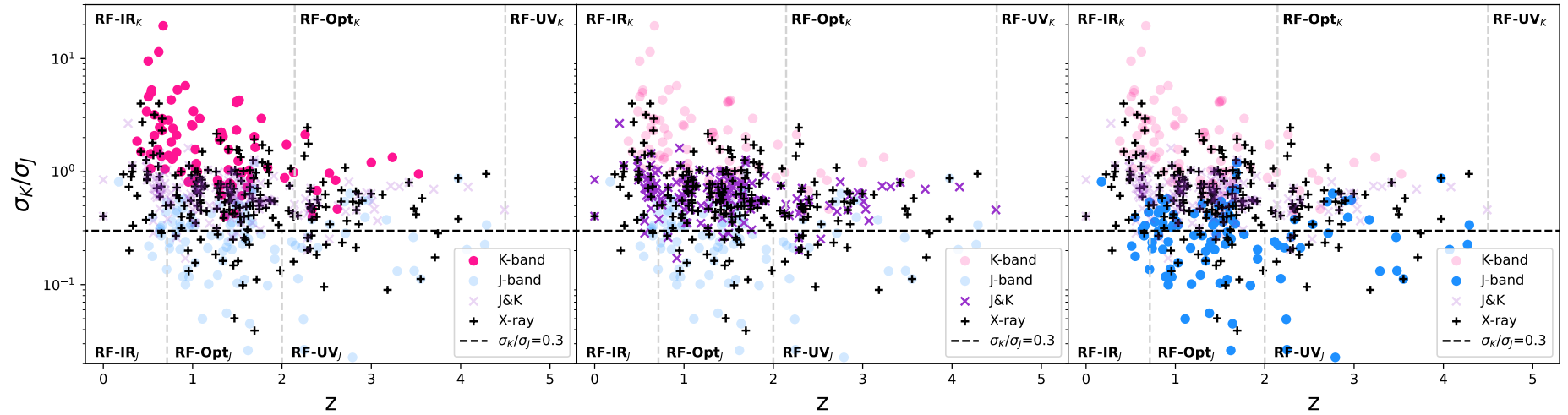


Figure 5.4: Ratio of  $K$  to  $J$ -band variability amplitude vs redshift for variability detected active galaxies. Pink dots show  $K$ -band only detect active galaxies, purple crosses show dual band detected active galaxies, blue dots show  $J$ -band only detected active galaxies and black crosses show X-ray AGN. Horizontal dashed grey line shows the model variability ratio of 0.3 as calculated according to the variability spectrum in [Meusinger et al. 2011](#). Vertical dashed light-grey lines denote the rest-frame emission ranges for the  $K$  and  $J$ -band above and below the  $Y=0.3$  line respectively.

generation of  $K$ -band variability. Likewise the RF-optical AGN are more luminous as seen in their higher redshift, and as such more likely outshine their host galaxy leading to a higher measurement of  $\sigma_J$ .

This explanation is in agreement with the study of Seyfert galaxy Fairall 9 by [Clavel et al. 1989](#). They found the  $K$ -band variability of the AGN to be out of phase with UV, optical and  $J$ -band variability measures. From this, they interpreted  $K$ -band emission to probe thermal re-radiation of UV and optical emission from dust in an active galaxy, whereas  $J$ -band emission originates from the accretion disk of the AGN.

## 5.4 Spectral energy distribution analysis

To investigate if variability in the  $K$ -band preferentially detects dust-reprocessed light from AGN, we investigate the spectral energy distributions (SEDs) of the galaxies. We also introduce a comparative sample of active galaxies selected through X-ray emission and split these galaxies based on their hardness ratio (HR), as a proxy for the obscuration. In this research we consider X-ray soft galaxies ( $HR < 0$ ) to be unobscured and X-ray hard galaxies ( $HR \geq 0$ ) to be obscured.

### 5.4.1 Mass Matching

For a fair comparison of the SEDs of the active galaxies to be made, we begin by mass matching the sub-samples of variability detected ( $K$  and  $J$  band detected) and X-ray selected (hard and soft) active galaxies. Galaxies are required to have stellar masses within 1% of each other (Fig 5.5), taking the samples from 180 to 74 detections in the  $K$ -band and 239 to 83  $J$ -band detections as well as 323 to 247 X-ray hard AGN and 387 to 262 X-ray soft AGN.

### 5.4.2 Calculating spectral energy distributions

To build spectral energy distributions for the galaxies (Figure 5.6), we take the 12 bands of photometry in the UDS (Chapter 2) and convert the measured AB magnitude values

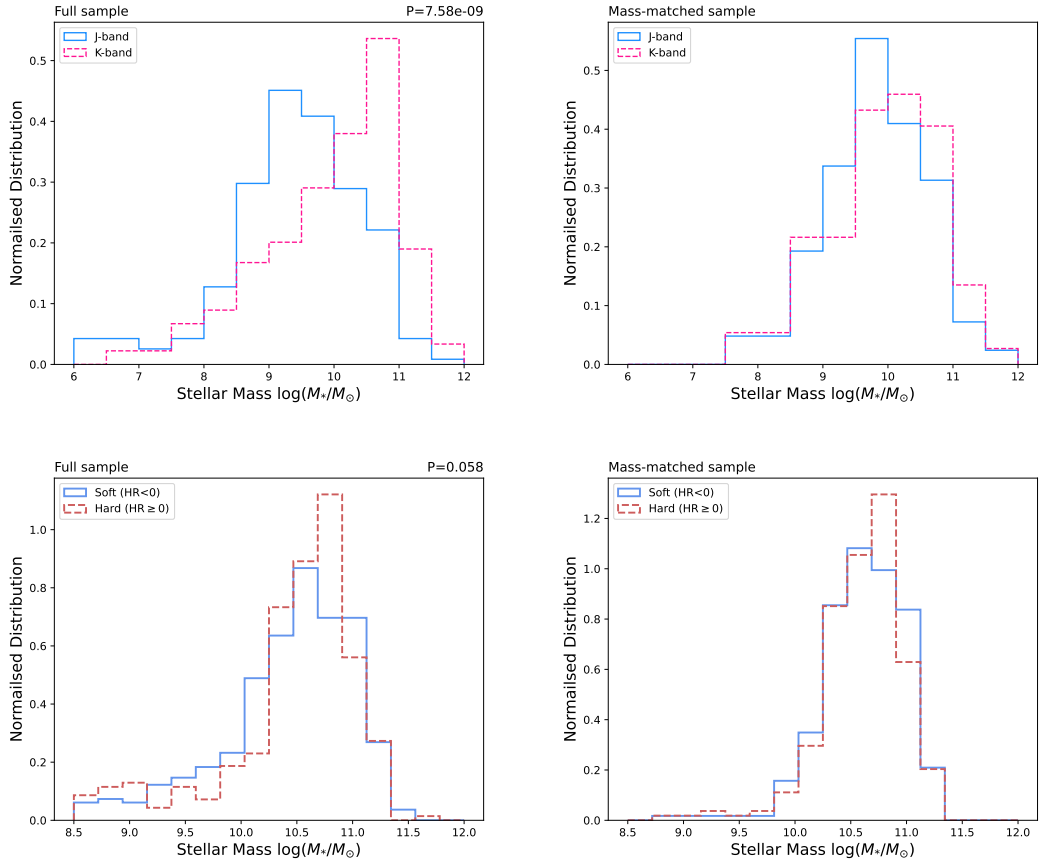


Figure 5.5: Stellar mass distributions of variability detected active galaxies split by detection band (top) and X-ray bright active galaxies split by hardness ratio (bottom). The left and right columns show the distribution prior to and after mass-matching respectively. Galaxy populations are mass matched within 1% of each other. In the top row, blue histogram shows the distribution for *J*-band detected active galaxies and the pink dashed histogram show the *K*-band detected active galaxies. In the bottom row the blue histogram shows X-ray soft active galaxies and the red dashed histogram shows the X-ray hard active galaxies.

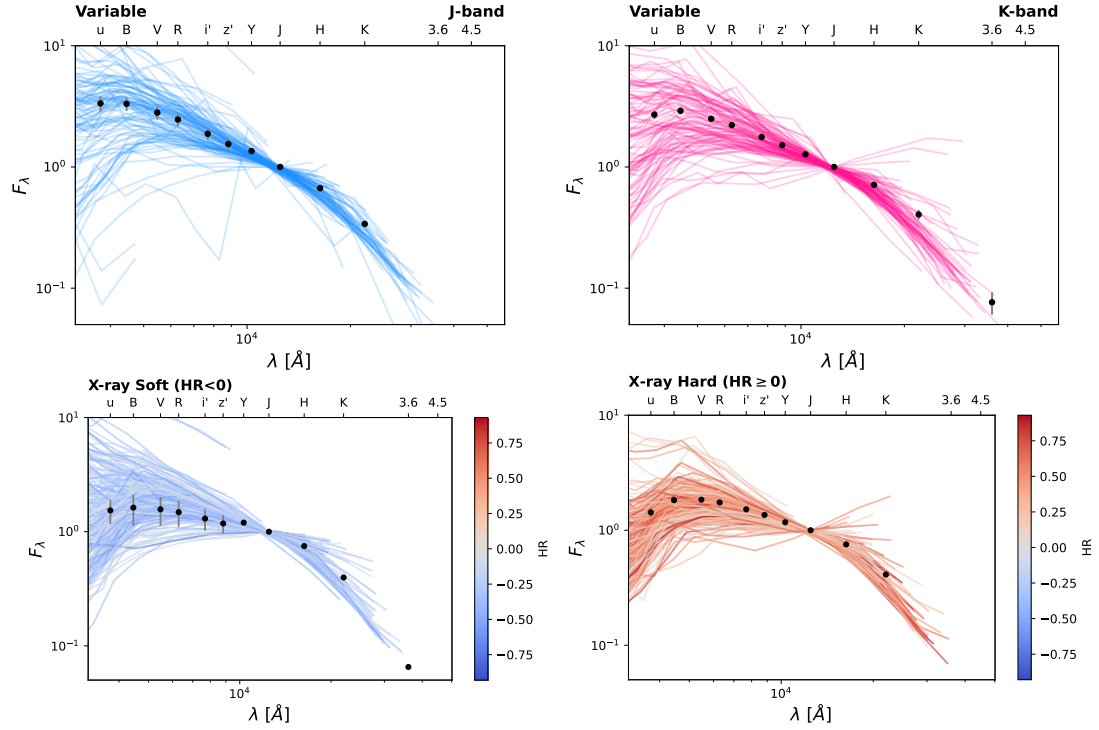


Figure 5.6: Rest-frame spectral energy distributions for the active galaxies studied in Section 5.4. In the top row, blue lines show active galaxies selected via  $J$ -band variability and pink lines show active galaxies selected in the  $K$ -band. The SEDs of X-ray detected active galaxies are split into X-ray soft ( $HR < 0$ ) and X-ray hard ( $HR \geq 0$ ) samples, and colour coded by hardness ratio on the same scale. All SEDs are normalised to unity in the  $J$ -band and have black points at each photometric band denoting the average flux density value at that wavelength, with the standard error on the mean being shown.

into flux densities ( $F_\lambda$ ). We then shift the flux density measurements into the rest-frame based on the galaxy's redshift. These rest-frame SEDs are then normalised to unity in the  $J$ -band, where normalised, rest-frame values of flux density are calculated by interpolation at each of the 12 wavebands of the UDS photometry. These final flux density values are converted back into AB magnitudes where appropriate.

### 5.4.3 SED comparison

Inspecting these SEDs, we find the largest differences in the ultraviolet,  $U$ -band. Visually, this is most apparent in the X-ray detected active galaxies, where X-ray soft galaxies show a range of  $U$ -band flux densities, but X-ray hard galaxies tend to be predominately faint in this filter. This difference can be seen by comparing the  $U-B$  colour of the

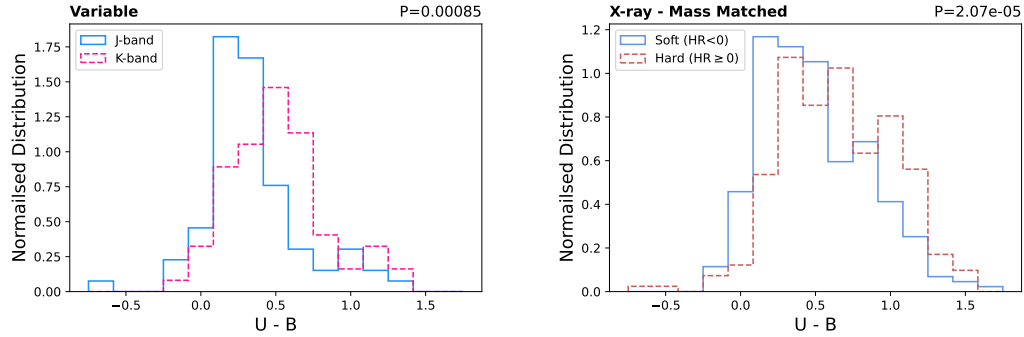


Figure 5.7: Rest frame  $U - B$  colour distribution for variability detected (left) and X-ray detected (right) active galaxies. For the variability detected sample, the blue histogram represents active galaxies selected as variable in the  $J$ -band only, and the pink dashed histogram shows galaxies selected as variable in the  $K$ -band. For the X-ray detected sample, galaxies are split based on their hardness ratio, with X-ray soft galaxies denoted by the blue histogram and X-ray hard galaxies shown as the red dashed histogram. Sub-samples in each plot are mass-matched within 1 per cent of each other. The P-values shown are from a Kolmogorov-Smirnov test between corresponding sub-samples, and confirms that the  $K$ -band selected and X-ray hard active galaxies have significantly different underlying distribution of  $U - B$  colour than the  $J$ -band selected and X-ray soft galaxies respectively.

galaxies, with Figure 5.7 showing this comparison. As seen visually in the overall shape of the SEDs, the distribution of the  $U - B$  colour in the X-ray hard active galaxies is redder compared to the X-ray soft active galaxies. Similar results are found for the  $J$  and  $K$ -band detected active galaxies, with the  $K$ -band detected sample having a redder  $U - B$  colour distribution compared to the  $J$ -band detected objects. For both comparisons a Kolmogorov–Smirnov (KS) test confirms that samples do not draw from the same underlying distribution and from this we conclude that variability in the infrared bands are able to provide information on the UV absorption of a galaxy.

## 5.5 Stellar Populations

In section 5.4 we find that the detection of band of the variable AGN is linked with the UV absorption of the active galaxy, however it is possible that differences in stellar populations drives the UV emission of the galaxies.

To investigate this, we plot the rest frame  $UVJ$  diagram of the galaxies in Figure

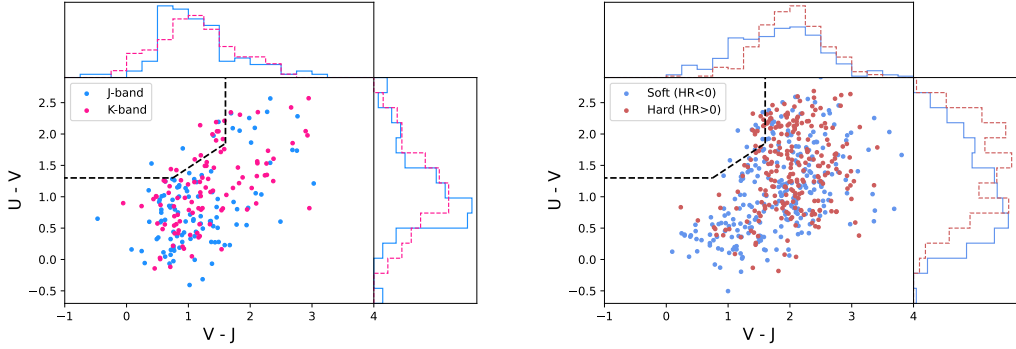


Figure 5.8: Rest-frame  $UVJ$  colour - colour diagram for mass-matched samples of variability detected (left) and X-ray detected (right) active galaxies. The black dashed line is as defined in Schreiber et al. 2015 and delineates quiescent galaxies from star-forming galaxies. Quiescent galaxies lie in the top left of the diagram. For the variability detected sample, blue points indicate  $J$ -band selected active galaxies and pink points show  $K$ -band selected active galaxies. In the X-ray detected sample, galaxies are split based on their hardness ratio, with X-ray soft galaxies shown as blue points and X-ray hard galaxies shown in red. In both plots, corresponding coloured histograms show the colour distribution.

5.8. A  $UVJ$  colour-colour diagram is commonly used to separate out star-forming and quiescent galaxies (Wuyts et al., 2007), and we use the standard selection box as outlined in Williams et al. 2009 and Schreiber et al. 2015 to accomplish this.

Inspecting this diagram, we find no evidence that the differences in UV emission in the active galaxies is due to the age of the stellar population. A vast majority of all mass-matched galaxies lie within the star-forming region of the diagram, with the distributions of the matched  $K$  and  $J$ -band detected galaxies being statistically similar according to a KS test and X-ray hard galaxies skewing red in both  $U - V$  and  $V - J$ , which is known to indicate dust emission over older stellar populations (Williams et al., 2009). From this we find that differences in stellar age does not pose a plausible explanation the relatively faint UV emission in  $K$ -band selected active galaxies.

## 5.6 Variability timescale

As reviewed in Section 5.1, more evidence has been found in favour of IR AGN spectra beyond  $\sim 2\mu\text{m}$  being generated via thermal re-radiation of optical and UV light by dust

over a non-thermal emission scenario. We find differences in the chromatic nature of AGN variability amplitudes when splitting the active galaxies by selection band in section 5.2, and model comparisons confirm that observed results cannot be explained by selection bias in the sample in Section 5.3. SED analysis reveals  $K$ -band variable AGN are systematically fainter in the UV compared to  $J$ -band variable AGN in Section 5.4 and a UVJ diagram confirms that the active galaxies have similar stellar populations regardless of detection method in Section 5.5. Combining these results, the properties of the  $K$ -band detected AGN favour a dust-driven, thermal emission model over a non-thermal emission model more consistent with the  $J$ -band detected sample.

To investigate the hypothesis that  $K$ -band variability does result from thermal emission processes, we examine the timescale of the measured variability in the active galaxies. In addition to providing clues to the origin of the variability, investigating the timescale variability takes place on effectively measures the AGN power spectrum. Generally, AGN variability has been found to be dominated by long term trends, and this is commonly known as a red-noise spectrum (e.g. [Lawrence et al. 1987](#); [Uttley et al. 2014](#)). Objects with blue-noise spectra behave in the opposite way, where variability on short timescales dominate the overall fluctuations seen in the object (e.g. a supernova event). As expressed in [Hunt et al. 1994](#), non-thermal, direct emission theory places no limit on the timescale of variability for a given wavelength. Thermal emission however, is dust-dependent and limited by the sublimation temperature and therefore orbital radius of the material, rendering variability on scales shorter than  $\sim 1$  year impossible. This means we would expect to see contributions from both short and long timescales to the overall observed variability in a non-thermal emission scenario, however thermal emission is restricted the longest timescales only, resulting in red-noise spectra only.

As detailed in [Almaini et al. 2000](#), the variability amplitude relates to the power spectrum as

$$\sigma^2 \propto f^{-\alpha}, \quad (5.2)$$

where  $\sigma$  is the AGN variability amplitude,  $f$  is the frequency in terms of variability timescale (*not* observed frequency of the light) and  $\alpha$  is the spectral index. Negative values of  $\alpha$  result in a red-noise spectrum, positive values lead to a blue noise spectrum and  $\alpha=0$  corresponds to white noise, where the variability in the object shows no dependence

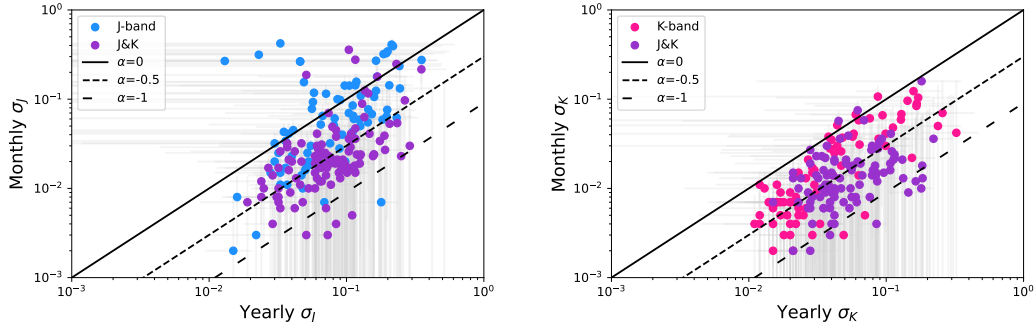


Figure 5.9: Modified, month-scale fractional variability amplitude vs year-scale variability amplitude for variability detected active galaxies. Measurements in the  $J$ -band are shown in the left plot and measurements in the  $K$ -band are shown on the right.  $J$ -band detected active galaxies are shown by blue points,  $K$ -band detected active galaxies are shown by pink points and active galaxies variable in both  $J$  and  $K$  photometric bands are shown as purple points, with light grey lines showing the errors on measurements. Several values for the spectral index,  $\alpha$ , are over-plotted as lines on the diagram.

on timescale. To study the variability timescale of the AGN in this sample, we compare the fractional variability amplitude measured on year timescales to a modified fractional variability amplitude measured on month timescales, where year-scale/semester effects have been removed (see Section 3.5).

Inspecting Figure 5.9, we find the timescale that variability occurs on is different for the  $J$ -band detected sample compared to the  $K$ -band detected sample. In the  $J$ -band, significant variability on month scales can be observed in the AGN with the highest variability amplitudes. Further to this, the contribution from month-timescales seems to correlate with the magnitude of the AGN fluctuations, as the lowest amplitudes are dominated by variations on year timescales. The  $K$ -band detected sample behaves differently however, with year-length variations clearly dominating the entire sample regardless of the magnitude of variations themselves. These same results remain true for corresponding measures of dual-band detected AGN, which are analysed in the same manner. For  $J$ -band fluctuations in these galaxies, we find fluctuations on short timescales significantly contribute to measured variability amplitude in the AGN with the highest levels of variation. The  $K$ -band measurements however remains consistent with the AGN variable only in the  $K$ -band, requiring several years of observations before variability can be observed.

We also find that these results link to observed properties in the active galaxies. Taking

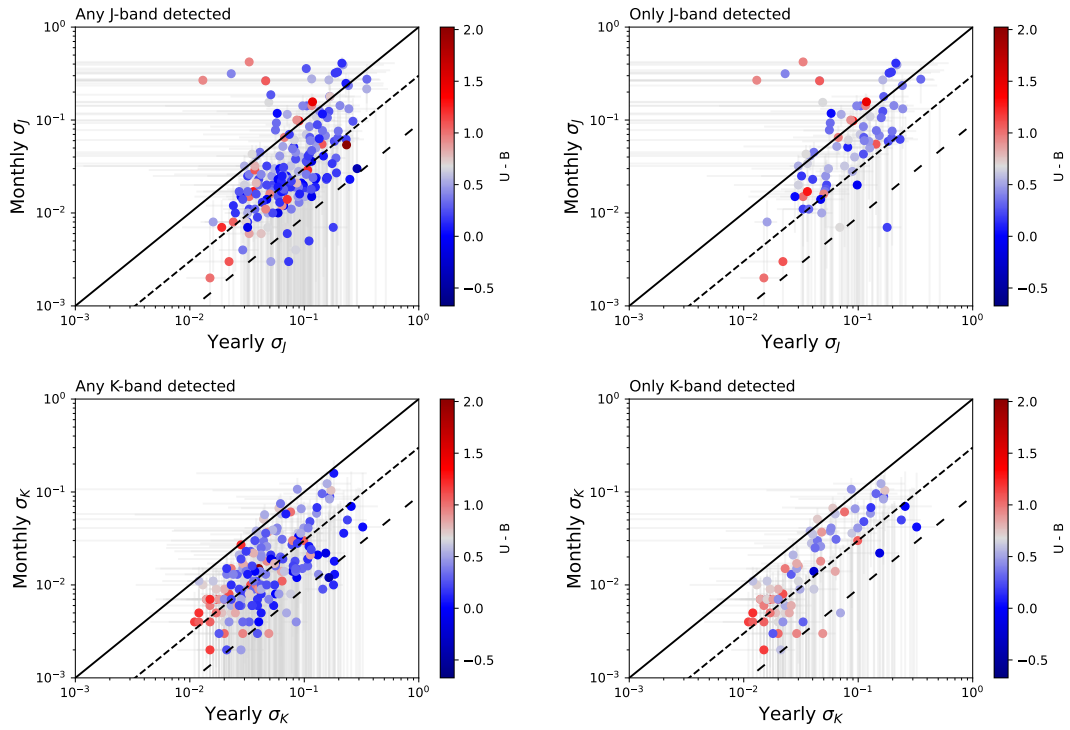


Figure 5.10: Modified, month-scale fractional variability amplitude vs semester variability amplitude for variability detected active galaxies. Measurements in the *J*-band are shown in the top row and measurements in the *K*-band are shown in the bottom row. The first column contains any galaxy detected as variable in the described photometric band and the second column shows galaxies only classed as variable in one band, with the AGN variable in both *J* and *K*-bands removed. Points are colour coded by the  $U - B$  colour and light grey lines show the errors on measurements. Black diagonal lines on the figure are the same as Figure 5.9, showing different values of the spectral index  $\alpha$ .

the comparison shown in Figure 5.9 and colour coding the points by the  $U - B$  colour seen in Figure 5.7 we produce Figure 5.10. Here we find variability amplitude measurements anti-correlation with  $U - B$  colour in the  $K$ -band selected variable AGN. No such relationship is observed in  $J$ -band detected objects and these results remain true when corresponding measurements from dual-band detected AGN are included. This provides more evidence in favour of a dust-reprocessing scenario in the  $K$ -band detected objects, as higher levels of obscuration would lead to the redder colours, dilution in variability amplitude and variability timescales limited to order years and longer, as observed.

## 5.7 Conclusions

In this research, we investigate the properties of AGN selected using long-term near-infrared variability in the  $J$  ( $1.2\mu\text{m}$ ) and  $K$  ( $2.2\mu\text{m}$ ) photometric bands. We compare these active galaxies to each other as well as to a set of X-ray AGN, split by hardness ratio as a proxy for dust obscuration in active galaxies.

We first study how the measured variability amplitude ( $\sigma_\lambda$ ) changes with wavelength. From this we find variability in  $J$ -band detected AGN anti-correlates with wavelength, in agreement with previous optical and UV studies of AGN variability (Cid Fernandes et al. 1996, Berk et al. 2004, MacLeod et al. 2010, Zuo et al. 2012). Variability in AGN selected in the  $K$ -band however show the opposite trend, correlating variability amplitude and wavelength. To determine if these opposing results are intrinsic properties of the AGN, we investigate the nature of the variability amplitude in dual-band detected objects as well as X-ray AGN. Both of these groups of AGN are found to anti-correlate variability with wavelength, confirming that the differences observed in the  $J$  and  $K$ -band detected AGN are not due to selection biases in the samples.

We next investigate the AGN variability spectrum by comparing amplitude measurements split by detection band to the model spectrum presented in Meusinger et al. 2011. This model predicts that an unobscured AGN should be more variable in bluer bands, with the  $\sigma_K$  to  $\sigma_J$  amplitude ratio being  $\approx 10/3$ . We find that AGN detected from  $J$ -band variability largely match this prediction, with the observed ratio in other AGN decreasing with increasing dominance of the  $K$ -band detection.

Investigating the rest-frame origin of measured variability finds evidence that variability

in different wavebands are generated in different ways.  $J$ -band detections best fit the accretion disk fluctuation model presented in Meusinger et al. 2011, having no preference for the rest-frame emission of the  $J$ -band flux as well as showing no evolution with redshift. Dual band detected AGN have similar properties, but are noticeably offset from the model-predicted  $\sigma_K/\sigma_J$  value, likely due to impact of  $K$ -band emission on the measurements.  $K$ -band detected AGN however, show significantly different features, with a majority of the galaxies originating at RF-IR redshifts and  $\sigma_K/\sigma_J$  decreasing over cosmic time. These properties could be explained by dust obscuration as well as an increased prominence in the host galaxy emission at low redshift. Dusty higher redshift objects would have their intrinsic emission reddened beyond the  $K$ -band as well as preferentially observing more luminous AGN, reducing the relative host galaxy emission. In addition to this, the minority of  $K$ -band detected AGN at RF-optical redshifts are found to have  $\sigma_K/\sigma_J$  similar to the model-predicted value, which would occur if such objects were truly unobscured, AGN dominated systems. We inspect the spectral energy distribution of the galaxies for signs that IR emission is due to thermal reprocessing of bluer light in the  $K$ -band detected galaxies. Here, we take the sub-samples of active galaxies detected as variable in the  $J$  and  $K$ -band only, and mass-match them within 1 per cent of each other based on the measured stellar mass. In addition to this, we introduce a further, mass-matched, comparative sample of X-ray detected active galaxies, split by hardness ratio as a proxy for dust obscuration.

Comparisons of the SEDs of these galaxies finds different levels of UV emission, with  $K$ -band detected active galaxies appearing redder in the  $U - B$  colour compared to  $J$ -band detections. Analogous results are found in the X-ray galaxies, with X-ray hard active galaxies having a redder  $U - B$  distribution compared to the X-ray soft galaxies. UVJ measurements also confirm these differences are not due to the age of the stellar population in the galaxies.

Finally, we investigate the variability timescale to see if dust obscuration is a likely explanation for the differing properties of the samples. To do this, we compare the year-scale variability amplitude to a modified month-scale variability amplitude, where semester/year effects have been removed. In doing this, we find the most variable  $J$ -band detections show variability on both short and long timescales, an effect that is expected if variability in these objects arises from accretion disk fluctuations that propagate out through the system.  $K$ -band variability, however, only occurs on semester timescales in line with a dust-reprocessing scenario of variability where shorter fluctuations would

be impossible. Consistent results are observed in the corresponding measurements for dual-band detected AGN, which supports the dust-driven variability scenario for  $K$ -band detections.

Connecting the variability timescales to observed properties of the SEDs, an anti-correlation in amplitude and  $U - B$  colour is found in the  $K$ -band sample, but no correlation between UV colour and amplitude is observed in the  $J$ -detections, with equivalent measurements from dual-band variable AGN following the same trends. Likewise, these results are in agreement with dust-reprocessing scenarios, where higher levels of dust contamination absorbs more UV light, diluting variability amplitudes in the process.

Overall, we conclude that splitting active galaxies found using long-term, near-infrared variability, by the detection band finds active galaxies with systematically different properties. We confirm that the correlation of variability amplitude and wavelength is opposite for  $J$ -band detected and  $K$ -band detected AGN and we find  $K$ -band variable active galaxies to be consistently UV faint compared to galaxies variable in the  $J$ -band.

The observed properties of  $K$ -band detected active galaxies suggest the IR spectrum is dominated by thermal emission from hot dust over non-thermal radiation processes. These results are consistent with [Clavel et al. 1989](#), and therefore if the NIR spectrum of AGN can be attributed to a combination of thermal and non-thermal emission processes, thermal emission begins to dominate over non-thermal emission between the rest-frame  $J$  and rest-frame  $K$ -band.

# **Chapter 6**

## **Science Chapter 3**

### **6.1 Introduction**

In this chapter, we examine if and how AGN emission impacts host galaxy parameters and vice versa. To do this, we compare the parameters of the AGN selected in this study to a set of inactive galaxies matched in stellar mass, redshift, and effective radius as a control sample.

### **6.2 Data and sample selection**

In this research, we use both ground based and space based imaging of the Ultra Deep Field. In addition to the ground based data the UDS provides (see Chapter 2 for full details) we introduce the Cosmic Assembly Near-Infrared Deep Extragalactic Legacy Survey (CANDELS) survey. This survey was taken on the Hubble Space Telescope and covers a smaller section of the wider, ground based UDS field with higher resolution imaging.

### 6.2.1 Ground based UDS field

For ground based, UDS imaging, the active galaxies consist of the 601 variability detected AGN and 710 X-ray bright AGN found in Section 3.1. To look for clues that link AGN activity to the host galaxy, we select a set of inactive galaxies matched to the features of active galaxies to function as a control sample. The ground based UDS catalogue covers a wider field compared to the space based surveys discussed in the following sections, and as such we are able to impose the following criteria for an inactive or ‘regular’ galaxy to be selected as a control galaxy whilst also retaining a large sample for reasonable conclusions to be drawn. Inactive galaxies must have:

- $M_{control} \pm 5\% M_{active}$
- $R_e^{control} \pm 10\% R_e^{active}$
- $z_{control} \pm 5\%(1+z_{active})$

where  $M$  is the stellar mass,  $R_e$  is the effective radius and  $z$  is the galaxy’s redshift. An inactive galaxy must fall within all three of the mass, radius and redshift limits to be a valid control galaxy. Applying this finds 4,336 control galaxies for the variability detected active galaxies and 4,614 control galaxies for the X-ray selected active galaxies.

### 6.2.2 Space based CANDELS field

In addition to the ground based UDS imaging, we have access to HST space-based imaging of a section of the Ultra Deep Field. The Cosmic Assembly Near-Infrared Deep Extragalactic Legacy Survey (CANDELS) survey consists of five fields:

- The Great Observatories Origins Deep Survey (GOODS)-North field
- The Great Observatories Origins Deep Survey (GOODS)-South field
- Cosmological Evolution Survey (COSMOS)
- Extended Groth Strip (EGS)

- The Ultra Deep Survey (UDS),

with a point source limiting magnitude of  $H = 27.7$ mag. Here we make use of the CANDELS UDS field, which covers a small area of the wider UKIDSS UDS field via the Hubble Space Telescope’s Wide Field Camera 3 infrared channel (WFC3/IR) and WFC3 ultraviolet/optical channel, as well as The Advanced Camera for Surveys (ACS) (Grogin et al. 2011; Koekemoer et al. 2011). The CANDELS catalogue consists of 35,932 extended sources, which is matched to the ‘*best galaxies*’ subset of the UDS DR11 (Section 2.1) where we recover 18,014 sources for use in this study.

When using this imaging, samples of AGN drop from 601 to 48 variability detected AGN and 710 to 203 X-ray detected AGN. Again, controls for this sample were determined by matching inactive galaxies to active galaxies on stellar mass, radius and redshift; however we relax the selection criteria to:

- $M_{control} \pm 10\% M_{active}$
- $R_e^{control} \pm 20\% R_e^{active}$
- $z_{control} \pm 20\%(1+z_{active})$

to ensure a reasonable sample of control galaxies for comparison given the smaller catalogue. This results in 488 control galaxies matched to the 48 variability detected active galaxies and the control sample for the 203 X-ray detected active galaxies contains 1,655 inactive galaxies.

### 6.3 Determining host galaxy parameters

Magnitude measurements and structural parameters for ground-based imaging were measured in Almaini et al. 2017 using the GALAPAGOS (Barden et al., 2012) software. Details of the same data being measured on HST imaging can be found in Maltby et al. 2018 and van der Wel et al. 2012, both of which used GALFIT. All studies fit Sérsic profiles to data, with Almaini et al. 2017 using ground based IR imaging taken in the  $K$ -band. Maltby et al. 2018 uses the optical, space-based imaging ( $I$  and  $V$ -band) and

[van der Wel et al. 2012](#) again uses space based imaging, but in the  $J$  and  $K$  infrared bands.

To measure galaxy parameters we use GALFITM ([Häubler et al., 2013](#)), which is a variant of the 2D fitting algorithm GALFIT ([Peng et al. 2002; Peng et al. 2010](#)) developed as part of the Measuring Galaxy Morphology (MEGAMORPH) project. GALFIT calculates a best-fit model to the surface brightness of a given galaxy by minimising the  $\chi^2$  of the fit, and GALFITM extends this functionality, allowing for the fitting of multiple science images in different wavebands simultaneously.

Here we fit a Sérsic ([Sersic, 1968](#)) + PSF models to HST ACS and WFC3 images in the  $V$ ,  $I$ ,  $J$  and  $H$ -bands. A full explanation of how the PSFs used in this study were constructed can be found in [Maltby et al. \(2018\)](#), but to summarise,  $\sim 150$  stars in the CANDELS-UDS region were isolated and  $4\times 4 \text{ arcsec}^2$  postage stamps of these stars were taken. These images were normalised in flux and then stacked according to the median value. This process is repeated for all four of the WFC3 and ACS bands, with a final PSF being constructed for each corresponding filter.

Sérsic models are convolved with a point spread function (PSF) and compared to the original surface brightness distribution of the science image. Parameters from the Sérsic profile include:

- Effective radius in image pixels along the semi-major axis ( $R_e$ )
- Sérsic index ( $n$ )
- Axis ratio (semi-minor axis/semi-major axis;  $b/a$ )
- Position angle
- Apparent Magnitude

with the PSF model returning a magnitude. Both a combined Sérsic + PSF and singular Sérsic model are fit to all galaxies within this study and we explore how this effects the measured results in active and inactive galaxies in the following sections.

## 6.4 Calculating environmental density

Aperture number densities for galaxies within the UDS are calculated using the technique described in Lani et al. 2013. For each galaxy, a cylindrical volume was constructed based on a 250kpc radius and a  $\pm 0.5\text{Gyr}$  "depth", which is characteristic of the typical errors in the photometric redshift. Within this volume the number of neighbouring galaxies with apparent K-band magnitudes below  $K = 25$  (AB) were counted; this value was then normalised according to the expectation assuming a uniform distribution of galaxies, taking into account masking and the edges of the field, to give the value of relative density. This density,  $\rho_{250}$ , is the environmental density measure we make use of in this analysis with values greater than one indicating an over-dense region and values less than one indicating an under-dense region (Taylor et al., 2023).

## 6.5 Results

### 6.5.1 Environment

To investigate if and how active galaxies differ from inactive galaxies, we first examine large scale properties of the active galaxies. Specifically, we study the environment that active galaxies reside in. In Figure 6.1 we plot the aperture number density vs lookback time for the X-ray bright and variability detected active galaxies and corresponding matched control galaxies determined in Section 6.2.1. Inspecting this, we find both variable and X-ray bright AGN have different environments when comparing them to their control galaxies, with these differences changing over cosmic time. The environments of the X-ray bright active galaxies and control galaxies follow similar shapes over cosmic times, with densities peaking around  $\sim 6\text{Gyrs}$  ago and decreasing either side of this, however the active galaxies in this sample are consistently found to be in denser environments compared to their matched control galaxies. The environments of the variability detected sample are different to this however, seen most significantly in the lowest lookback bins. Overall the environmental density of the variable galaxies decreases near linearly with increasing lookback times whereas the control galaxies follow similar distributions as the X-ray samples, with environments being most galaxy dense at  $\sim 6\text{Gyrs}$  and steadily decreasing either side of this. These results suggest that for

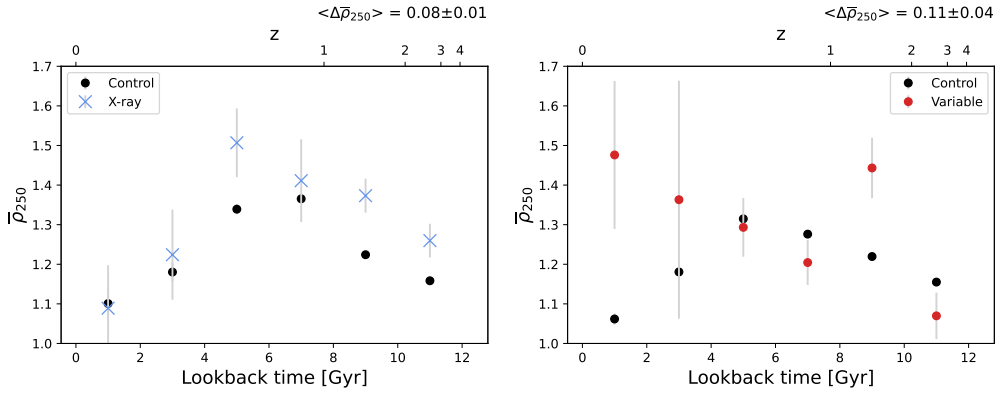


Figure 6.1: Average aperture number density ( $\bar{\rho}_{250}$ ) vs lookback time for X-ray detected active galaxies (left) and variability detected active galaxies (right). X-ray bright active galaxies are denoted by blue crosses, variability detected active galaxies are shown as red points and corresponding matched control galaxies are shown as black points. Galaxies are averaged in bins of 2Gyrs, with lookback times calculated based on redshift and the cosmology quoted in the introduction (Chapter 1). Corresponding redshifts are show on the top x-axis of the plot and the errorbars in grey are the standard error on the mean.  $\langle \Delta \bar{\rho}_{250} \rangle$  denotes the difference in the overall mean  $\rho_{250}$  for all epochs between the active galaxies and their corresponding control galaxies.

a given epoch one would be more likely to observe X-ray bright active galaxies in dense environments. Consistent conclusions cannot be drawn from variable active galaxies however, as at high redshift they appear to be in slightly under-dense regions of space with this diverging at lower redshifts where they seem to be in a range of environments that are generally denser than matched inactive galaxies.

### 6.5.2 Infrared and optical colour comparisons

Having studied the wider environments of the active galaxies, we next inspect the features of the galaxies themselves. One interesting property to study is how the colours of the active galaxies change between groups as well as compared to their control galaxies. Again, investigating characteristics as a function of cosmic time, we look at how the optical and infrared colour changes with increasing lookback time in Figure 6.2. Focusing first on the X-ray detected sample, we find no differences in either the optical or infrared colours of the galaxies compared to the control galaxies over cosmic time. In both cases the active sample have similar values and show a similar distribution to the controls for all epochs studied. In the case of the variability detected galaxies, this same

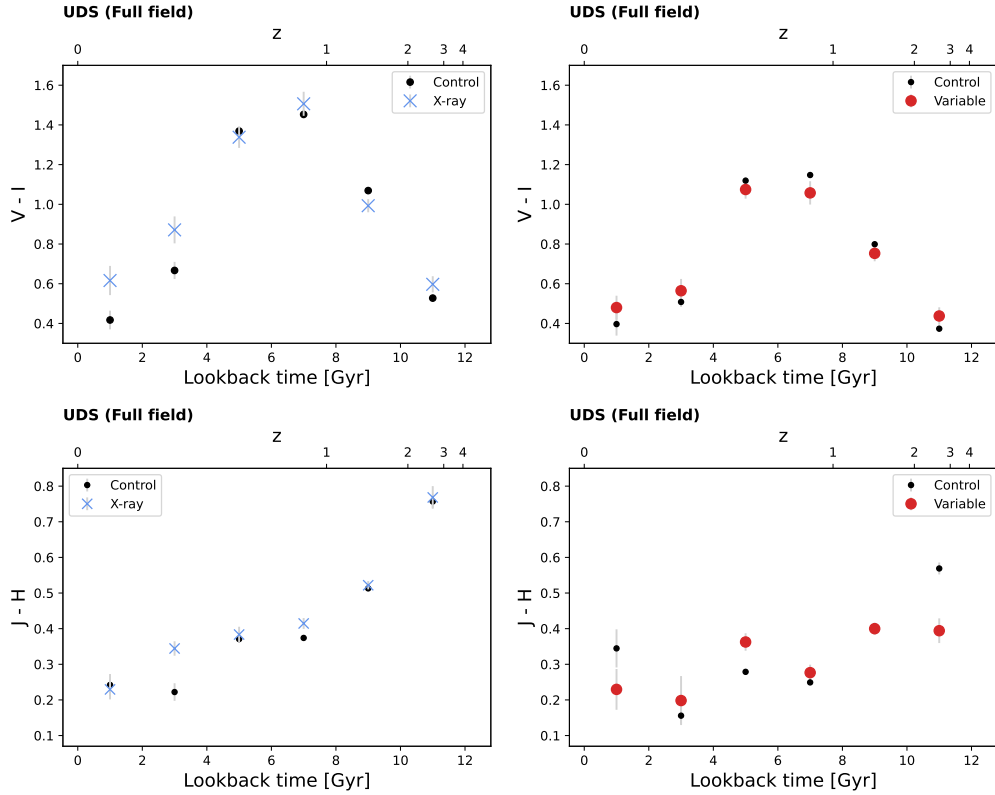


Figure 6.2: Optical  $V - I$  (top) and infrared  $J - H$  (bottom) colour vs lookback time for active galaxies and their matched control galaxies. The left column shows X-ray detected AGN as blue crosses and the right column has variability detected active galaxies as red points. In both groups corresponding control galaxies are black points. Galaxies in these samples are drawn from the full, ground-based UDS field and measured magnitudes are apparent magnitudes. Galaxy colours are averaged in bins of 2Gyrs with error bars being the standard error on the mean. Lookback times are calculated based on the redshift, and corresponding redshifts are shown on the top x-axis of the plots.

similar-colour, similar-distribution result holds for the infrared colours of the galaxy, but not for the optical colours. In the case of optical colour measurements, correlations are not as clear, with optical colours of the variable active galaxies appearing largely flat over cosmic time.

Looking to the largest scales we find the active galaxies are found in different environments compared to similar, inactive galaxies, but looking at the colour evolution of the sample groups only finds small differences in the variability detected sample across cosmic time. To further compare like with like we investigate how the morphology of the galaxies impacts the observed colour and if this changes from active to control groups.

In Figure 6.3, we plot the optical  $V - I$  and infrared  $J - H$  colour vs the Sérsic index  $n$  for the active and control galaxies. Examining first the optical colours, we find that the active X-ray sample are consistently bluer compared to their matched control sample for all morphologies. In addition to this, they show no significant change in colour from disk to bulge dominated systems, whereas the control sample become slightly redder as the bulge component becomes more significant in the galaxy morphology. The optical colour of the active variable sample are also differ significantly from their controls. In disk dominated systems, the average optical colour of variability detected active galaxies is indistinguishable from that of the matched controls, however as bulge dominated systems are probed, the colours diverge. In this case the active galaxies get bluer as the Sérsic index increases whereas the colour of the control sample remains largely the same. Measurements of infrared colours and morphology show a lot of scatter in both X-ray and variability detected active galaxies however. For both cases, the control samples tend to have the same average colour regardless of the morphology of the galaxy, with the active galaxies showing no obvious consistency or trend when comparing the same  $J - H$  colour in the same Sérsic index bin. One key difference however is that the variability detected active galaxies and their controls are much bluer overall compared to the X-ray group and this is seen when comparing both the optical colours and the infrared colours.

Optically, we find that both the AGN have different colours from their controls for similar morphologies. Obvious observational differences are harder to find when inspecting the infrared colours of the active galaxies, however we do note that overall variability detected active galaxies tend to be bluer compared to the X-ray bright active galaxies in this sample. We next note that Chapter 5 found that the properties of the variability detected sample changed when splitting the galaxies by the band or bands they were found to be significantly variable in. To see if this effects extends to the colours, structural parameters and their potential evolution over cosmic time, we repeat this analysis in this research.

In Figure 6.4, we recreate the optical and infrared colours vs lookback time for the variable galaxies seen in Figure 6.2, however we split the variability detected active galaxies into groups based on the photometric band they are found to be significantly variable in. Inspecting the optical colours, we find that the colour of the active galaxies evolves similarly with cosmic time compared to the controls, with the reddest galaxies being found  $\sim$ 6Gyrs ago and the colours being bluer at times either side of this. Beyond

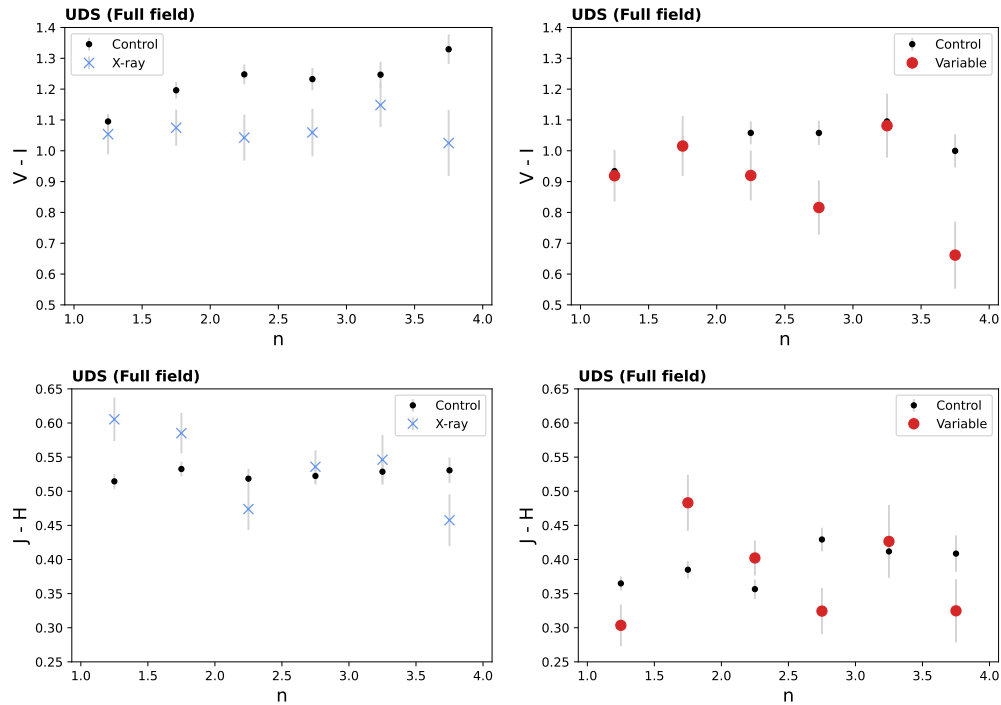


Figure 6.3: Optical  $V - I$  (top) and infrared  $J - H$  (bottom) colour vs Sérsic index for active galaxies and matched control galaxies. The left column shows X-ray detected AGN as blue crosses and the right column has variability detected active galaxies as red points. In both groups corresponding control galaxies are black points. Galaxies in this sample are drawn from the full, ground-based UDS field and measured magnitudes are apparent magnitudes. Galaxy colours are averaged in bins of 2Gyrs with error bars being the standard error on the mean.

this, interestingly differences arise when comparing the active galaxy colours based on bands. The optical colour of the AGN variable in the  $J$ -band only as well as the dual-band detected active galaxies are bluer than the control galaxies for all epochs studied. When inspecting the colours of the  $K$ -band detected sample however, we find that they appear redder than the matched control galaxies. Differences in the groups also appears when inspecting the infrared colours. We find the same result that the  $K$ -band variable active galaxies appear redder than the matched controls whereas the  $J$ -band objects are bluer in colour, however we find the dual-band detected sample changes compared to the optical measurements, with their infrared colour largely being redder than the controls for most cosmic epochs. The trend over cosmic time also changes.  $K$ -band variable galaxies behave like the control galaxies, with the  $J-H$  colour getting redder with increasing lookback time. This effect diminishes however in the dual-band detected group, with the reddening of the IR colour being less than that of the  $K$ -band and the  $J$ -band variable galaxies show almost no colour evolution with cosmic time.

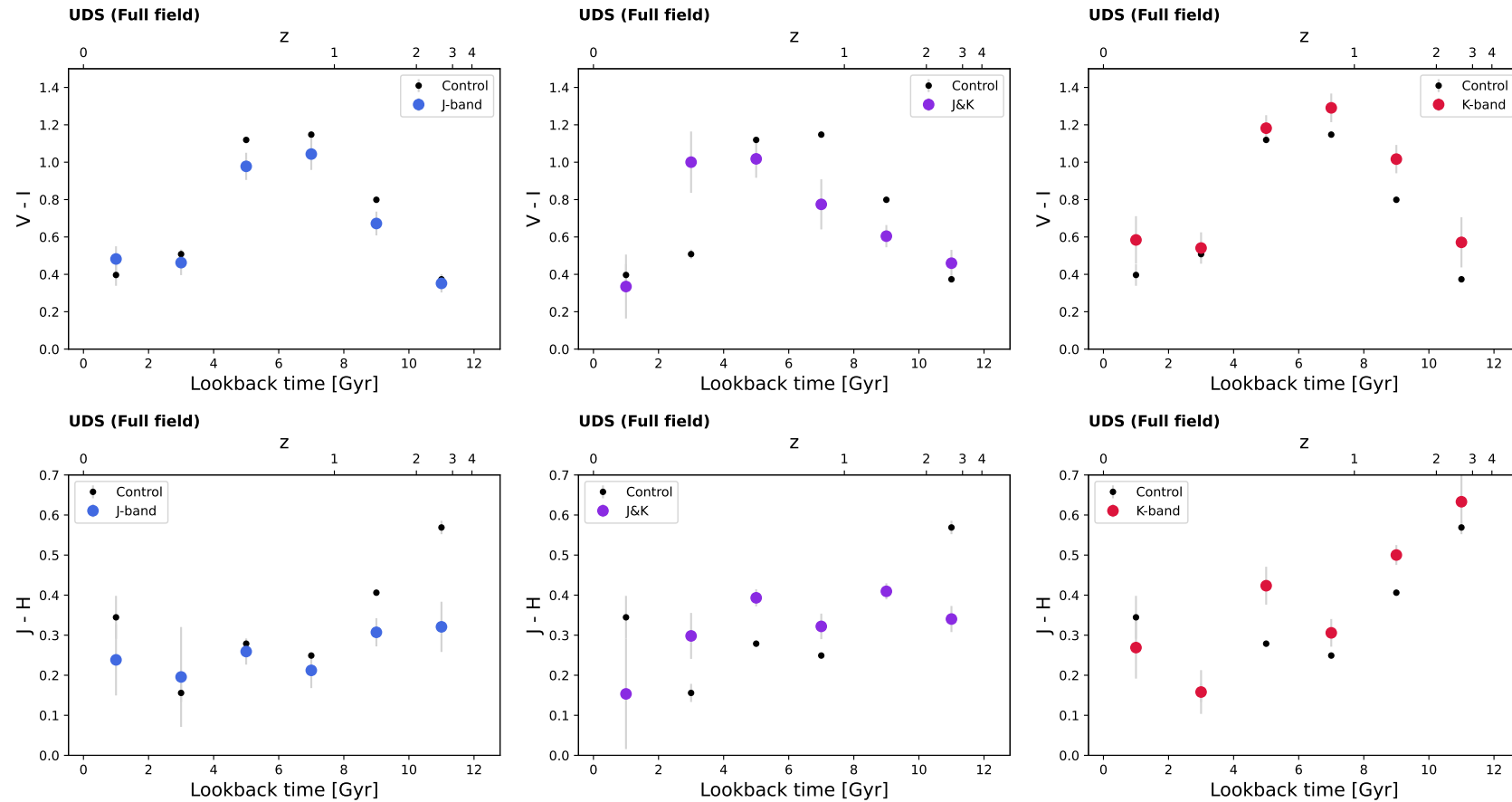


Figure 6.4: Optical  $V - I$  (top) and infrared  $J - H$  (bottom) colour vs lookback time for variability detected active galaxies, split by detection band. AGN variable in the  $J$ -band only are shown as blue point, AGN variable in the  $K$ -band only are shown as red points and dual-band detected AGN are shown as purple points. Matched control galaxies are the same in each plot and are shown as black points. Galaxies in this sample are drawn from the full, ground-based UDS field and measured magnitudes are apparent magnitudes. Galaxy colours are averaged in bins of 2Gyrs with error bars being the standard error on the mean. Lookback times are calculated based on the redshift, and corresponding redshifts are shown on the top x-axis of the plots.

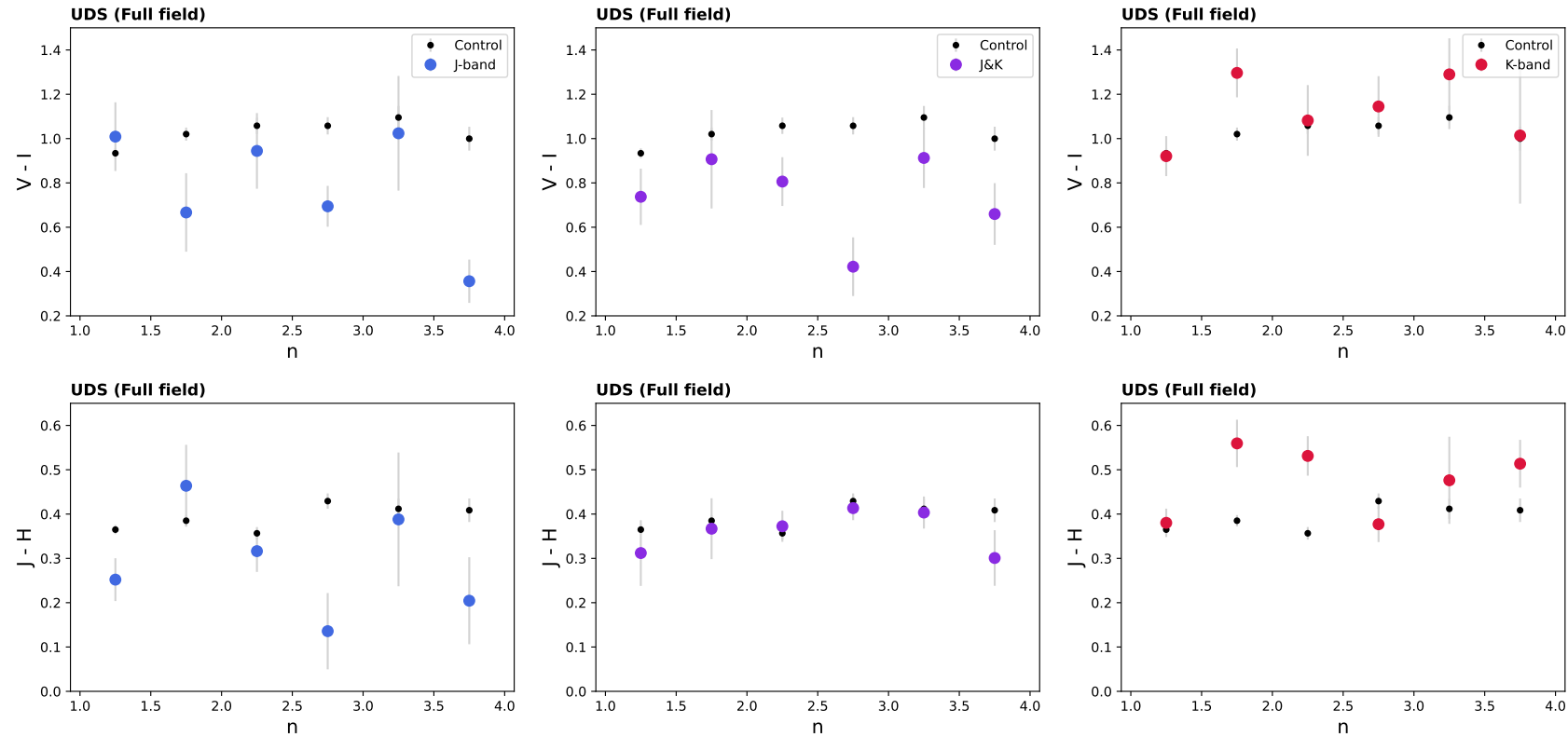


Figure 6.5: Optical  $V - I$  (top) and infrared  $J - H$  (bottom) colour vs Sérsic index for variability detected active galaxies, split by detection band. AGN variable in the  $J$ -band only are shown as blue point, AGN variable in the  $K$ -band only are shown as red points and dual-band detected AGN are shown as purple points. Matched control galaxies are the same in each plot and are shown as black points. Galaxies in this sample are drawn from the full, ground-based UDS field and measured magnitudes are apparent magnitudes. Galaxy colours are averaged in bins of 2Gyrs with error bars being the standard error on the mean. Lookback times are calculated based on the redshift, and corresponding redshifts are shown on the top x-axis of the plots.

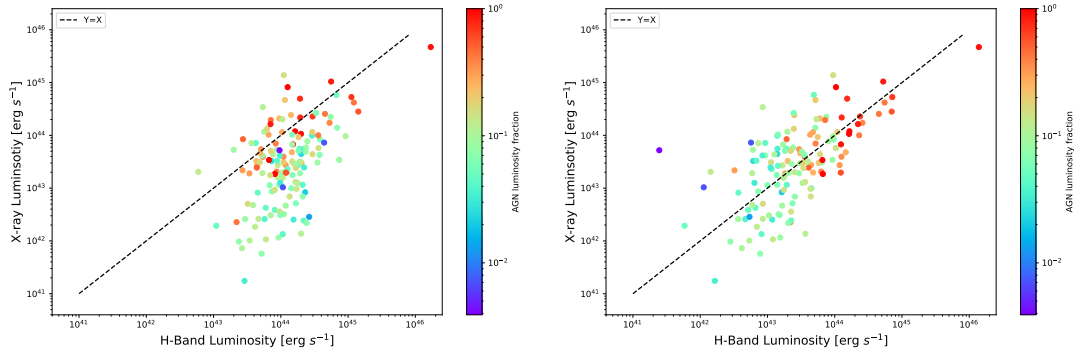


Figure 6.6: Full band (0.5-10keV) X-ray luminosity vs  $H$ -band, infrared luminosity for the X-ray detected active galaxies found within the CANDELS-UDS imaging region. In the left plot the infrared luminosity is based on a single Sérsic fit to the galaxy image, in the right plot the infrared luminosity plot is calculated from the magnitude returned from the PSF component in a combined Sérsic + PSF fit to the active galaxies. In both plots the X-ray luminosity is drawn from the Chandra X-ray catalogue (see Chapter 2). Points are colour coded according to the fraction of observed light attributed to the PSF component in the two component Sérsic + PSF fit and the black dashed line traces unity.

In Figure 6.5 we move on to comparing the optical and infrared colours of the variable galaxies, split by the detection  $K$ -band sample appear redder compared to the  $J$ -band sample, with dual-band detected AGN lying somewhat in the middle of both groups. Combining this comparison with the trends reported in Figure 6.4 finds evidence in agreement with the conclusions found in Chapter 5, with the  $K$ -band detected active galaxies appearing largely redder in colour in all scenarios which could be explained by the existence of dust in the system.

### 6.5.3 Host galaxy comparison

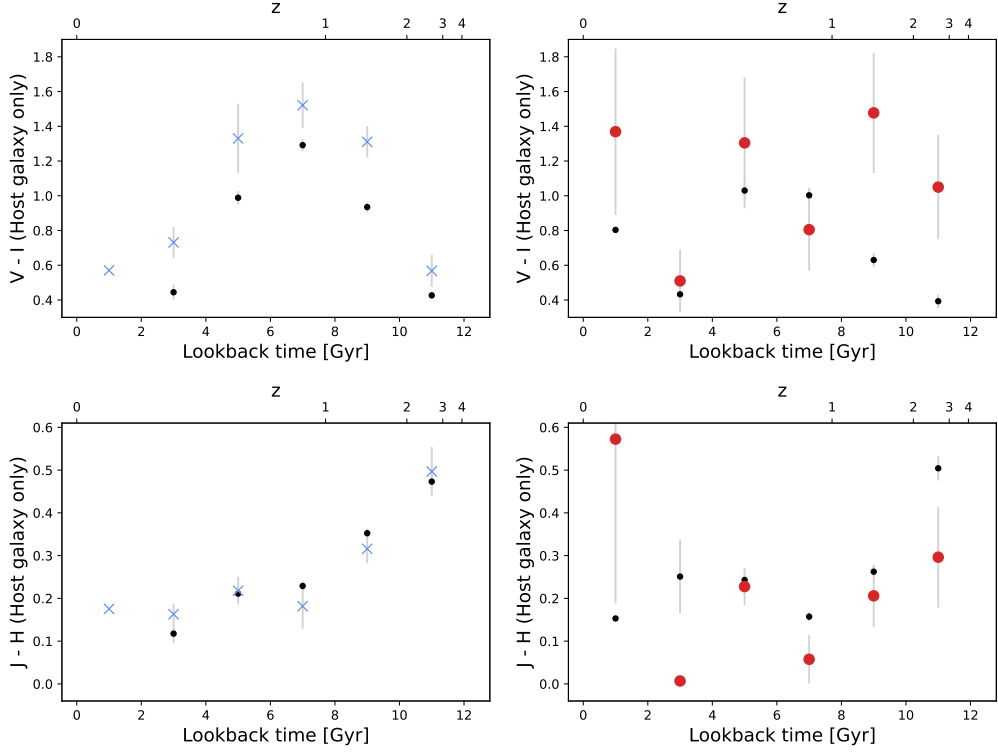


Figure 6.7: Optical  $V - I$  (top) and infrared  $J - H$  (bottom) colour vs lookback time for the active galaxies and matched control galaxies in the CANDELS-UDS imaging region. X-ray bright active galaxies are denoted by blue crosses, variability detected active galaxies are shown as red points and corresponding matched control galaxies are shown as black points. Galaxies are averaged in bins of 2Gyrs with error bars being the standard error on the mean. Lookback times are calculated based on the redshift, and corresponding redshifts are shown on the top x-axis of the plots. Magnitudes are apparent magnitudes and are drawn from the Sérsic component in a combined two component Sérsic + PSF fit to the active galaxies.

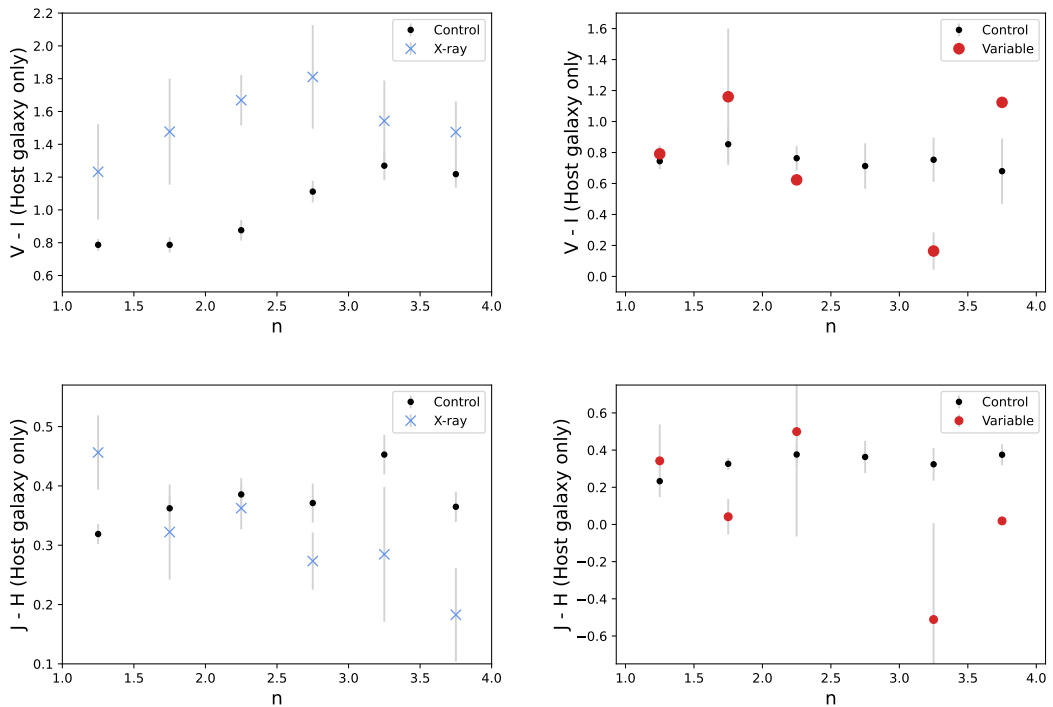


Figure 6.8: Optical  $V - I$  (top) and infrared  $J - H$  (bottom) colour vs Sérsic index for the active galaxies and matched control galaxies in the CANDELS-UDS imaging region. X-ray bright active galaxies are denoted by blue crosses, variability detected active galaxies are shown as red points and corresponding matched control galaxies are shown as black points. Galaxies are averaged in bins of 2Gyrs with error bars being the standard error on the mean. Magnitudes are apparent magnitudes and both magnitudes and Sérsic index are drawn from the Sérsic component in a combined two component Sérsic + PSF fit to the active galaxy images.

# **Chapter 7**

## **Conclusions and Future Work**

### **7.1 Conclusions**

### **7.2 Future work**

- Investigate the host galaxies of AGN in more detail, specifically possible explanations for the why the hosts of X-ray AGN get bluer with colour
- Look at the host properties of the variable AGN in general, hopefully should be doable with high resolution imaging like JWST provides.
- Especially look at in/how the host of variable AGN change depending on the band the AGN was found to be variable in. If  $K$ -band variables are dusty for example, you may expect them to be red in colour.

# Bibliography

- Alloin, D. M. D. M., Johnson, R., & Lira, P., eds. 2006, Physics of active galactic nuclei at all scales No. 693 (Berlin: Springer)
- Almaini, O., Lawrence, A., Shanks, T., et al. 2000, Monthly Notices of the Royal Astronomical Society, 315, 325, doi: [10.1046/j.1365-8711.2000.03385.x](https://doi.org/10.1046/j.1365-8711.2000.03385.x)
- Almaini, O., Wild, V., Maltby, D. T., et al. 2017, Monthly Notices of the Royal Astronomical Society, 472, 1401, doi: [10.1093/mnras/stx1957](https://doi.org/10.1093/mnras/stx1957)
- Antonucci, R. 1993, Annual Review of Astronomy and Astrophysics, 31, 473, doi: [10.1146/annurev.aa.31.090193.002353](https://doi.org/10.1146/annurev.aa.31.090193.002353)
- Avni, Y., & Tananbaum, H. 1986, The Astrophysical Journal, 305, 83, doi: [10.1086/164230](https://doi.org/10.1086/164230)
- Baade, W., & Minkowski, R. 1954, The Astrophysical Journal, 119, 215, doi: [10.1086/145813](https://doi.org/10.1086/145813)
- Barden, M., Häußler, B., Peng, C. Y., McIntosh, D. H., & Guo, Y. 2012, Monthly Notices of the Royal Astronomical Society, 422, 449, doi: [10.1111/j.1365-2966.2012.20619.x](https://doi.org/10.1111/j.1365-2966.2012.20619.x)
- Barvainis, R. 1987, The Astrophysical Journal, 320, 537, doi: [10.1086/165571](https://doi.org/10.1086/165571)
- Beckmann, V., & Shrader, C. 2013, in Proceedings of An INTEGRAL view of the high-energy sky (the first 10 years) - 9th INTEGRAL Workshop and celebration of the 10th anniversary of the launch — PoS(INTEGRAL 2012), Vol. 176 (SISSA Medialab), 069, doi: [10.22323/1.176.0069](https://doi.org/10.22323/1.176.0069)
- Berk, D. E. V., Wilhite, B. C., Kron, R. G., et al. 2004, The Astrophysical Journal, 601, 692, doi: [10.1086/380563](https://doi.org/10.1086/380563)
- Best, P. N., von der Linden, A., Kauffmann, G., Heckman, T. M., & Kaiser, C. R. 2007, Monthly Notices of the Royal Astronomical Society, 379, 894, doi: [10.1111/j.1365-2966.2007.11937.x](https://doi.org/10.1111/j.1365-2966.2007.11937.x)
- Bianchi, S., Mainieri, V., & Padovani, P. 2022, in Handbook of X-ray and Gamma-ray

- Astrophysics, ed. C. Bambi & A. Santangelo (Singapore: Springer Nature), 1–32, doi: [10.1007/978-981-16-4544-0\\_113-1](https://doi.org/10.1007/978-981-16-4544-0_113-1)
- Bradshaw, E. J., Almaini, O., Hartley, W. G., et al. 2013, Monthly Notices of the Royal Astronomical Society, 433, 194, doi: [10.1093/mnras/stt715](https://doi.org/10.1093/mnras/stt715)
- Brammer, G. B., Dokkum, P. G. v., & Coppi, P. 2008, The Astrophysical Journal, 686, 1503, doi: [10.1086/591786](https://doi.org/10.1086/591786)
- Bruzual, G., & Charlot, S. 2003, Monthly Notices of the Royal Astronomical Society, 344, 1000, doi: [10.1046/j.1365-8711.2003.06897.x](https://doi.org/10.1046/j.1365-8711.2003.06897.x)
- Cackett, E. M., Bentz, M. C., & Kara, E. 2021, iScience, 24, 102557, doi: [10.1016/j.isci.2021.102557](https://doi.org/10.1016/j.isci.2021.102557)
- Casali, M., Adamson, A., Oliveira, C. A. d., et al. 2007, Astronomy & Astrophysics, 467, 777, doi: [10.1051/0004-6361:20066514](https://doi.org/10.1051/0004-6361:20066514)
- Chabrier, G. 2003, Publications of the Astronomical Society of the Pacific, 115, 763, doi: [10.1086/376392](https://doi.org/10.1086/376392)
- Cid Fernandes, R., Aretxaga, I., & Terlevich, R. 1996, Monthly Notices of the Royal Astronomical Society, 282, 1191, doi: [10.1093/mnras/282.4.1191](https://doi.org/10.1093/mnras/282.4.1191)
- Civano, F., Elvis, M., Brusa, M., et al. 2012, The Astrophysical Journal Supplement Series, 201, 30, doi: [10.1088/0067-0049/201/2/30](https://doi.org/10.1088/0067-0049/201/2/30)
- Clavel, J., Wamsteker, W., & Glass, I. S. 1989, The Astrophysical Journal, 337, 236, doi: [10.1086/167100](https://doi.org/10.1086/167100)
- Cleary, K., Lawrence, C. R., Marshall, J. A., Hao, L., & Meier, D. 2007, The Astrophysical Journal, 660, 117, doi: [10.1086/511969](https://doi.org/10.1086/511969)
- Collaboration, E. H. T., Akiyama, K., Alberdi, A., et al. 2022, The Astrophysical Journal Letters, 930, L12, doi: [10.3847/2041-8213/ac6674](https://doi.org/10.3847/2041-8213/ac6674)
- Collaboration, T. E. H. T., Akiyama, K., Alberdi, A., et al. 2019, The Astrophysical Journal Letters, 875, L1, doi: [10.3847/2041-8213/ab0ec7](https://doi.org/10.3847/2041-8213/ab0ec7)
- Collier, S., & Peterson, B. M. 2001, The Astrophysical Journal, 555, 775, doi: [10.1086/321517](https://doi.org/10.1086/321517)
- Curtis, H. D. 1988, Publications of the Astronomical Society of the Pacific, 100, 6, doi: [10.1086/132128](https://doi.org/10.1086/132128)
- Cutri, R. M., Wisniewski, W. Z., Rieke, G. H., & Lebofsky, M. J. 1985, The Astrophysical Journal, 296, 423, doi: [10.1086/163461](https://doi.org/10.1086/163461)
- Dayal, P., Volonteri, M., Choudhury, T. R., et al. 2020, Monthly Notices of the Royal Astronomical Society, 495, 3065, doi: [10.1093/mnras/staa1138](https://doi.org/10.1093/mnras/staa1138)

- Dermer, C. D., & Giebels, B. 2016, Comptes Rendus. Physique, 17, 594, doi: [10.1016/j.crhy.2016.04.004](https://doi.org/10.1016/j.crhy.2016.04.004)
- Dicken, D., Tadhunter, C., Axon, D., et al. 2009, The Astrophysical Journal, 694, 268, doi: [10.1088/0004-637X/694/1/268](https://doi.org/10.1088/0004-637X/694/1/268)
- Edelson, R. A., & Malkan, M. A. 1987, The Astrophysical Journal, 323, 516, doi: [10.1086/165848](https://doi.org/10.1086/165848)
- Eide, M. B., Ciardi, B., Graziani, L., et al. 2020, Monthly Notices of the Royal Astronomical Society, 498, 6083, doi: [10.1093/mnras/staa2774](https://doi.org/10.1093/mnras/staa2774)
- Einstein, A. 1916, Annalen der Physik, 354, 769, doi: [10.1002/andp.19163540702](https://doi.org/10.1002/andp.19163540702)
- Einstein, A., Minkowski, H. H., Saha, M., & Bose, S. 1920, The principle of relativity; original papers ([Calcutta] The University of Calcutta). <http://archive.org/details/principleofrelat00eins>
- Elmer, E., Almaini, O., Merrifield, M., et al. 2020, Monthly Notices of the Royal Astronomical Society, 493, 3026, doi: [10.1093/mnras/staa381](https://doi.org/10.1093/mnras/staa381)
- Elmer, E., Merrifield, M., Almaini, O., Hartley, W. G., & Maltby, D. T. 2021, Monthly Notices of the Royal Astronomical Society: Letters, 503, L47, doi: [10.1093/mnrasl/slab023](https://doi.org/10.1093/mnrasl/slab023)
- Elvis, M., Green, R. F., Bechtold, J., et al. 1986, The Astrophysical Journal, 310, 291, doi: [10.1086/164683](https://doi.org/10.1086/164683)
- Fan, L., Fang, G., Chen, Y., et al. 2014, The Astrophysical Journal Letters, 784, L9, doi: [10.1088/2041-8205/784/1/L9](https://doi.org/10.1088/2041-8205/784/1/L9)
- Fath, E. A. 1909, Lick Observatory Bulletin, 149, 71, doi: [10.5479/ADS/bib/1909LicOB.5.71F](https://doi.org/10.5479/ADS/bib/1909LicOB.5.71F)
- Finkelstein, D. 1958, Physical Review, 110, 965, doi: [10.1103/PhysRev.110.965](https://doi.org/10.1103/PhysRev.110.965)
- Fitch, W. S., Pacholczyk, A. G., & Weymann, R. J. 1967, The Astrophysical Journal, 150, L67, doi: [10.1086/180095](https://doi.org/10.1086/180095)
- Furusawa, H., Kosugi, G., Akiyama, M., et al. 2008, The Astrophysical Journal Supplement Series, 176, 1, doi: [10.1086/527321](https://doi.org/10.1086/527321)
- Gabor, J. M., Impey, C. D., Jahnke, K., et al. 2009, The Astrophysical Journal, 691, 705, doi: [10.1088/0004-637X/691/1/705](https://doi.org/10.1088/0004-637X/691/1/705)
- Genzel, R., Eisenhauer, F., & Gillessen, S. 2010, Reviews of Modern Physics, 82, 3121, doi: [10.1103/RevModPhys.82.3121](https://doi.org/10.1103/RevModPhys.82.3121)
- Ghez, A. M., Klein, B. L., Morris, M., & Becklin, E. E. 1998, The Astrophysical Journal, 509, 678, doi: [10.1086/306528](https://doi.org/10.1086/306528)

- Green, A. R., McHardy, I. M., & Lehto, H. J. 1993, Monthly Notices of the Royal Astronomical Society, 265, 664, doi: [10.1093/mnras/265.3.664](https://doi.org/10.1093/mnras/265.3.664)
- Grogin, N. A., Conselice, C. J., Chatzichristou, E., et al. 2005, The Astrophysical Journal, 627, L97, doi: [10.1086/432256](https://doi.org/10.1086/432256)
- Grogin, N. A., Kocevski, D. D., Faber, S. M., et al. 2011, The Astrophysical Journal Supplement Series, 197, 35, doi: [10.1088/0067-0049/197/2/35](https://doi.org/10.1088/0067-0049/197/2/35)
- Hafez, I. 2010, phd, James Cook University, doi: [10.25903/6xsf-aa64](https://doi.org/10.25903/6xsf-aa64)
- Harrison, C. 2014, Doctoral, Durham University. <http://etheses.dur.ac.uk/10744/>
- Herrero, A., Kudritzki, R. P., Gabler, R., Vilchez, J. M., & Gabler, A. 1995, Astronomy and Astrophysics, 297, 556. <https://ui.adsabs.harvard.edu/abs/1995A&A...297..556H>
- Hickox, R. C., & Alexander, D. M. 2018, Annual Review of Astronomy and Astrophysics, 56, 625, doi: [10.1146/annurev-astro-081817-051803](https://doi.org/10.1146/annurev-astro-081817-051803)
- Hubble, E. 1929, Proceedings of the National Academy of Sciences, 15, 168, doi: [10.1073/pnas.15.3.168](https://doi.org/10.1073/pnas.15.3.168)
- Hubble, E. P. 1925, The Astrophysical Journal, 62, 409, doi: [10.1086/142943](https://doi.org/10.1086/142943)
- . 1926, The Astrophysical Journal, 64, 321, doi: [10.1086/143018](https://doi.org/10.1086/143018)
- Humason, M. L. 1932, Publications of the Astronomical Society of the Pacific, 44, 267, doi: [10.1086/124242](https://doi.org/10.1086/124242)
- Hunt, L. K., Zhekov, S., Salvati, M., Mannucci, F., & Stanga, R. M. 1994, Astronomy and Astrophysics, 292, 67. <https://ui.adsabs.harvard.edu/abs/1994A&A...292...67H>
- Häußler, B., Bamford, S. P., Vika, M., et al. 2013, Monthly Notices of the Royal Astronomical Society, 430, 330, doi: [10.1093/mnras/sts633](https://doi.org/10.1093/mnras/sts633)
- information@eso.org. 1999, The Hubble tuning fork - classification of galaxies. <https://www.spacetelescope.org/images/heic9902o/>
- Jarvis, M. J., Bonfield, D. G., Bruce, V. A., et al. 2013, Monthly Notices of the Royal Astronomical Society, 428, 1281, doi: [10.1093/mnras/sts118](https://doi.org/10.1093/mnras/sts118)
- Kocevski, D. D., Hasinger, G., Brightman, M., et al. 2018, The Astrophysical Journal Supplement Series, 236, 48, doi: [10.3847/1538-4365/aab9b4](https://doi.org/10.3847/1538-4365/aab9b4)
- Koekemoer, A. M., Faber, S. M., Ferguson, H. C., et al. 2011, The Astrophysical Journal Supplement Series, 197, 36, doi: [10.1088/0067-0049/197/2/36](https://doi.org/10.1088/0067-0049/197/2/36)
- Kormendy, J., & Richstone, D. 1995, Annual Review of Astronomy and Astrophysics, 33, 581, doi: [10.1146/annurev.aa.33.090195.003053](https://doi.org/10.1146/annurev.aa.33.090195.003053)

- Kouzuma, S., & Yamaoka, H. 2012, The Astrophysical Journal, 747, 14, doi: [10.1088/0004-637X/747/1/14](https://doi.org/10.1088/0004-637X/747/1/14)
- Lani, C., Almaini, O., Hartley, W. G., et al. 2013, Monthly Notices of the Royal Astronomical Society, 435, 207, doi: [10.1093/mnras/stt1275](https://doi.org/10.1093/mnras/stt1275)
- Lawrence, A., Watson, M. G., Pounds, K. A., & Elvis, M. 1987, Nature, 325, 694, doi: [10.1038/325694a0](https://doi.org/10.1038/325694a0)
- Lawrence, A., Warren, S. J., Almaini, O., et al. 2007, Monthly Notices of the Royal Astronomical Society, 379, 1599, doi: [10.1111/j.1365-2966.2007.12040.x](https://doi.org/10.1111/j.1365-2966.2007.12040.x)
- LIGO Scientific Collaboration and Virgo Collaboration, Abbott, B., Abbott, R., et al. 2016, Physical Review Letters, 116, 061102, doi: [10.1103/PhysRevLett.116.061102](https://doi.org/10.1103/PhysRevLett.116.061102)
- Lira, P., Arévalo, P., Uttley, P., McHardy, I., & Breedt, E. 2011, Monthly Notices of the Royal Astronomical Society, 415, 1290, doi: [10.1111/j.1365-2966.2011.18774.x](https://doi.org/10.1111/j.1365-2966.2011.18774.x)
- Lira, P., Arévalo, P., Uttley, P., McHardy, I. M. M., & Videla, L. 2015, Monthly Notices of the Royal Astronomical Society, 454, 368, doi: [10.1093/mnras/stv1945](https://doi.org/10.1093/mnras/stv1945)
- Low, J., & Kleinmann, D. E. 1968, The Astronomical Journal, 73, 868, doi: [10.1086/110722](https://doi.org/10.1086/110722)
- Lyu, J., Alberts, S., Rieke, G. H., & Rujopakarn, W. 2022, The Astrophysical Journal, 941, 191, doi: [10.3847/1538-4357/ac9e5d](https://doi.org/10.3847/1538-4357/ac9e5d)
- MacLeod, C. L., Ivezić, , Kochanek, C. S., et al. 2010, The Astrophysical Journal, 721, 1014, doi: [10.1088/0004-637X/721/2/1014](https://doi.org/10.1088/0004-637X/721/2/1014)
- Madejski, G. G., & Sikora, M. 2016, Annual Review of Astronomy and Astrophysics, 54, 725, doi: [10.1146/annurev-astro-081913-040044](https://doi.org/10.1146/annurev-astro-081913-040044)
- Maltby, D. T., Almaini, O., Wild, V., et al. 2018, Monthly Notices of the Royal Astronomical Society, 480, 381, doi: [10.1093/mnras/sty1794](https://doi.org/10.1093/mnras/sty1794)
- . 2016, Monthly Notices of the Royal Astronomical Society: Letters, 459, L114, doi: [10.1093/mnrasl/slw057](https://doi.org/10.1093/mnrasl/slw057)
- McLure, R. J., Pearce, H. J., Dunlop, J. S., et al. 2013, Monthly Notices of the Royal Astronomical Society, 428, 1088, doi: [10.1093/mnras/sts092](https://doi.org/10.1093/mnras/sts092)
- McLure, R. J., Pentericci, L., Cimatti, A., et al. 2018, Monthly Notices of the Royal Astronomical Society, 479, 25, doi: [10.1093/mnras/sty1213](https://doi.org/10.1093/mnras/sty1213)
- Meusinger, H., Hinze, A., & Hoon, A. d. 2011, Astronomy & Astrophysics, 525, A37, doi: [10.1051/0004-6361/201015520](https://doi.org/10.1051/0004-6361/201015520)

- Michell, J. 1784, Philosophical Transactions of the Royal Society of London, 74, 35, doi: [10.1098/rstl.1784.0008](https://doi.org/10.1098/rstl.1784.0008)
- Netzer, H. 2013, The Physics and Evolution of Active Galactic Nuclei (New York, UNITED STATES: Cambridge University Press). <http://ebookcentral.proquest.com/lib/nottingham/detail.action?docID=1113069>
- Neugebauer, G., Soifer, B. T., Matthews, K., & Elias, J. H. 1989, The Astronomical Journal, 97, 957, doi: [10.1086/115040](https://doi.org/10.1086/115040)
- Pacholczyk, A. G., & Wisniewski, W. Z. 1967, The Astrophysical Journal, 147, 394, doi: [10.1086/149020](https://doi.org/10.1086/149020)
- Padovani, P., Alexander, D. M., Assef, R. J., et al. 2017, The Astronomy and Astrophysics Review, 25, 2, doi: [10.1007/s00159-017-0102-9](https://doi.org/10.1007/s00159-017-0102-9)
- Paltani, S., & Courvoisier, T. J. L. 1994, Astronomy and Astrophysics, 291, 74. <https://ui.adsabs.harvard.edu/abs/1994A&A...291...74P>
- Panagiotou, C., Papadakis, I., Kara, E., Kammoun, E., & Dovčiak, M. 2022, A physical model for the UV/optical power spectra of AGN, arXiv, doi: [10.48550/arXiv.2207.04917](https://doi.org/10.48550/arXiv.2207.04917)
- Peng, C. Y., Ho, L. C., Impey, C. D., & Rix, H.-W. 2002, The Astronomical Journal, 124, 266, doi: [10.1086/340952](https://doi.org/10.1086/340952)
- . 2010, The Astronomical Journal, 139, 2097, doi: [10.1088/0004-6256/139/6/2097](https://doi.org/10.1088/0004-6256/139/6/2097)
- Pentericci, L., McLure, R. J., Garilli, B., et al. 2018, Astronomy & Astrophysics, 616, A174, doi: [10.1051/0004-6361/201833047](https://doi.org/10.1051/0004-6361/201833047)
- Pierce, C. M., Lotz, J. M., Primack, J. R., et al. 2010, Monthly Notices of the Royal Astronomical Society, 405, 718, doi: [10.1111/j.1365-2966.2010.16502.x](https://doi.org/10.1111/j.1365-2966.2010.16502.x)
- Pouliasis, E., Georgantopoulos, I., Bonanos, A. Z., et al. 2019, Monthly Notices of the Royal Astronomical Society, 487, 4285, doi: [10.1093/mnras/stz1483](https://doi.org/10.1093/mnras/stz1483)
- Pozzetti, L., Bolzonella, M., Zucca, E., et al. 2010, Astronomy & Astrophysics, 523, A13, doi: [10.1051/0004-6361/200913020](https://doi.org/10.1051/0004-6361/200913020)
- Rees, M. J. 1984, Annual Review of Astronomy and Astrophysics, 22, 471, doi: [10.1146/annurev.aa.22.090184.002351](https://doi.org/10.1146/annurev.aa.22.090184.002351)
- Rees, M. J., Silk, J. I., Werner, M. W., & Wickramasinghe, N. C. 1969, Nature, 223, 788, doi: [10.1038/223788a0](https://doi.org/10.1038/223788a0)
- Rieke, G. H. 1978, The Astrophysical Journal, 226, 550, doi: [10.1086/156639](https://doi.org/10.1086/156639)
- Rieke, G. H., & Lebofsky, M. J. 1981, The Astrophysical Journal, 250, 87, doi: [10.1086/159350](https://doi.org/10.1086/159350)

- Rindler, W. 1956, Monthly Notices of the Royal Astronomical Society, 116, 662, doi: [10.1093/mnras/116.6.662](https://doi.org/10.1093/mnras/116.6.662)
- Salpeter, E. E. 1964, The Astrophysical Journal, 140, 796, doi: [10.1086/147973](https://doi.org/10.1086/147973)
- Sandage, A. 1961, The Hubble Atlas of Galaxies. <https://ui.adsabs.harvard.edu/abs/1961hag..book.....S>
- Sanders, D. B., Phinney, E. S., Neugebauer, G., Soifer, B. T., & Matthews, K. 1989, The Astrophysical Journal, 347, 29, doi: [10.1086/168094](https://doi.org/10.1086/168094)
- Schmidt, M. 1963, Nature, 197, 1040, doi: [10.1038/1971040a0](https://doi.org/10.1038/1971040a0)
- Schreiber, C., Pannella, M., Elbaz, D., et al. 2015, Astronomy & Astrophysics, 575, A74, doi: [10.1051/0004-6361/201425017](https://doi.org/10.1051/0004-6361/201425017)
- Schwarzschild, K. 1916, Abh. Konigl. Preuss. Akad. Wissenschaften Jahre 1906, 92, Berlin, 1907, 1916, 189. <https://ui.adsabs.harvard.edu/abs/1916AbhKP1916..189S>
- . 1999, On the gravitational field of a mass point according to Einstein's theory, arXiv, doi: [10.48550/arXiv.physics/9905030](https://arxiv.org/abs/physics/9905030)
- Sersic, J. L. 1968, Atlas de Galaxias Australes. <https://ui.adsabs.harvard.edu/abs/1968adga.book.....S>
- Seyfert, C. K. 1943, The Astrophysical Journal, 97, 28, doi: [10.1086/144488](https://doi.org/10.1086/144488)
- Shi, Y., Rieke, G. H., Hines, D. C., et al. 2005, The Astrophysical Journal, 629, 88, doi: [10.1086/431344](https://doi.org/10.1086/431344)
- Simpson, C., Westoby, P., Arumugam, V., et al. 2013, Monthly Notices of the Royal Astronomical Society, 433, 2647, doi: [10.1093/mnras/stt940](https://doi.org/10.1093/mnras/stt940)
- Slipher, V. M. 1913, Lowell Observatory Bulletin, 2, 56. <https://ui.adsabs.harvard.edu/abs/1913LowOB...2...56S>
- Smith, H. J., & Hoffleit, D. 1963, Nature, 198, 650, doi: [10.1038/198650a0](https://doi.org/10.1038/198650a0)
- Son, S., Kim, M., & Ho, L. C. 2022, The Astrophysical Journal, 927, 107, doi: [10.3847/1538-4357/ac4dfc](https://doi.org/10.3847/1538-4357/ac4dfc)
- Steffen, A. T., Strateva, I., Brandt, W. N., et al. 2006, The Astronomical Journal, 131, 2826, doi: [10.1086/503627](https://doi.org/10.1086/503627)
- Suh, H., Civano, F., Hasinger, G., et al. 2019, The Astrophysical Journal, 872, 168, doi: [10.3847/1538-4357/ab01fb](https://doi.org/10.3847/1538-4357/ab01fb)
- Sutherland, W., & Saunders, W. 1992, Monthly Notices of the Royal Astronomical Society, 259, 413, doi: [10.1093/mnras/259.3.413](https://doi.org/10.1093/mnras/259.3.413)
- Sánchez, P., Lira, P., Cartier, R., et al. 2017, The Astrophysical Journal, 849, 110, doi: [10.3847/1538-4357/aa9188](https://doi.org/10.3847/1538-4357/aa9188)

- Tananbaum, H., Avni, Y., Branduardi, G., et al. 1979, *The Astrophysical Journal*, 234, L9, doi: [10.1086/183100](https://doi.org/10.1086/183100)
- Taylor, E., Almaini, O., Merrifield, M., et al. 2023, *Monthly Notices of the Royal Astronomical Society*, 522, 2297, doi: [10.1093/mnras/stad1098](https://doi.org/10.1093/mnras/stad1098)
- Trevese, D., Boutsia, K., Vagnetti, F., Cappellaro, E., & Puccetti, S. 2008, *Astronomy & Astrophysics*, 488, 73, doi: [10.1051/0004-6361:200809884](https://doi.org/10.1051/0004-6361:200809884)
- Uttley, P., Cackett, E. M., Fabian, A. C., Kara, E., & Wilkins, D. R. 2014, *The Astronomy and Astrophysics Review*, 22, 72, doi: [10.1007/s00159-014-0072-0](https://doi.org/10.1007/s00159-014-0072-0)
- van der Wel, A., Bell, E. F., Häussler, B., et al. 2012, *The Astrophysical Journal Supplement Series*, 203, 24, doi: [10.1088/0067-0049/203/2/24](https://doi.org/10.1088/0067-0049/203/2/24)
- Volonteri, M., & Gnedin, N. Y. 2009, *The Astrophysical Journal*, 703, 2113, doi: [10.1088/0004-637X/703/2/2113](https://doi.org/10.1088/0004-637X/703/2/2113)
- Webster, B. L., & Murdin, P. 1972, *Nature*, 235, 37, doi: [10.1038/235037a0](https://doi.org/10.1038/235037a0)
- Williams, R. J., Quadri, R. F., Franx, M., Dokkum, P. v., & Labb  , I. 2009, *The Astrophysical Journal*, 691, 1879, doi: [10.1088/0004-637X/691/2/1879](https://doi.org/10.1088/0004-637X/691/2/1879)
- Wuyts, S., Labb  , I., Franx, M., et al. 2007, *The Astrophysical Journal*, 655, 51, doi: [10.1086/509708](https://doi.org/10.1086/509708)
- Zuo, W., Wu, X.-B., Liu, Y.-Q., & Jiao, C.-L. 2012, *The Astrophysical Journal*, 758, 104, doi: [10.1088/0004-637X/758/2/104](https://doi.org/10.1088/0004-637X/758/2/104)